

Some pages of this thesis may have been removed for copyright restrictions.

If you have discovered material in AURA which is unlawful e.g. breaches copyright, (either yours or that of a third party) or any other law, including but not limited to those relating to patent, trademark, confidentiality, data protection, obscenity, defamation, libel, then please read our Takedown Policy and contact the service immediately

Transducer
Development

TRANSDUCER DIFFRACTION THEORY AND
DEVELOPMENT OF AN ULTRASONIC TOMOGRAM

by

DAVID GEE

A thesis submitted to the University of
Aston in Birmingham for the degree of
Doctor of Philosophy

David Gee

Department of Physics
June 1981

Transducer Diffraction Theory and
Development of an Ultrasonic Tomogram

SUMMARY

The work described in this thesis is the development of an ultrasonic tomogram to provide outlines of cross-sections of the ulna in vivo. This instrument, used in conjunction with X-ray densitometry previously developed in this department, would provide actual bone mineral density to a high resolution.

It was hoped that the accuracy of the plot obtained from the tomogram would exceed that of existing ultrasonic techniques by about five times. Repeat measurements with these instruments to follow bone mineral changes would involve very low X-ray doses.

A theoretical study has been made of acoustic diffraction, using a geometrical transform applicable to the integration of three different Green's functions, for axisymmetric systems. This has involved the derivation of one of these in a form amenable to computation. It is considered that this function fits the boundary conditions occurring in medical ultrasonography more closely than those used previously. A three dimensional plot of the pressure field using this function has been made for a ring transducer, in addition to that for disc transducers using all three functions.

It has been shown how the theory may be extended to investigate the nature and magnitude of the particle velocity, at any point in the field, for the three functions mentioned. From this study, a concept of diffraction fronts has been developed, which has made it possible to determine energy flow also in a diffracting system. Intensity has been displayed in a manner similar to that used for pressure. Plots have been made of diffraction fronts and energy flow direction lines.

David Gee, Ph.D., 1981

Key Words:

Acoustic
Tomogram
Green's Functions
Velocity Computation
Diffraction Energy

ACKNOWLEDGMENTS
For Emilie, wherever I may find her.

... my supervisor, Dr. J. A. ...
... and assistance ...
... also ...
... valuable advice ...
... Howard ...

ACKNOWLEDGEMENTS

... whose department ...
... wife, Cathy, ...

I would like to express my thanks to my Supervisor, Dr J A Archer-Hall, whose active guidance, encouragement and assistance has made the work contained in this thesis possible. I am also grateful to my advisor, Dr P E Francois, for his valuable advice and encouragement.

I would also like to acknowledge the following:

The staff of the Physics Workshops, especially Howard Arrowsmith, for their practical assistance.

The Science Research Council, for their financial support.

Professor S E Hunt, in whose department the work was carried out.

Last, but not least, I thank my wife, Cathy, to whom this work is dedicated.

CONTENTS

ULTRASONIC TOMOGRAPHY

1. Introduction of Present Ultrasonic Tomogram 1

2. Ultrasonic Tomogram 2

3. Tomographic Reconstruction 3

4. Radial Movement 7

5. 15° Scans 8

6. Long 9

7. System 10

8. Electronic Development 11

1
2
2
4
7
8
10
11

	<u>Page No.</u>
SUMMARY	i
ACKNOWLEDGEMENTS	iii
LIST OF TABLES, FIGURES, PHOTOGRAPHS	x
<u>PREFACE</u>	1
P.1 Introduction	2
P.2 Bone Densitometry	2
P.2.1 The X-Ray Densitometer	4
P.2.2 Bone Tomography	6
P.2.2.1 Stages in the Evolution of Tomogram Design Concepts	7
P.2.2.2 Elaboration of Concept 2	8
P.2.2.3 Aims of Present Research	10
P.3 Transducer Diffraction Theory	11
<u>CHAPTER 1: INTRODUCTION TO ULTRASONIC TOMOGRAM</u>	16
1.1 General Introduction	17
1.2 General Description of Present Ultrasonic Tomogram	19
1.3 Basic Concepts of the Ultrasonic Tomogram	22
1.3.1 Choice of Transducer Configuration	22
1.3.2 Timing System	23
1.3.3 The Scanning System	25
1.3.4 Information to Control the Radial Movement	26
1.3.5 Display System	28
1.3.6 The Use of Two Separate 275° Scans	29
1.4 Comparisons with Alternative Systems	31
<u>CHAPTER 2: TOMOGRAM ELECTRONICS</u>	35
2.1 Introduction	36
2.1.1 Description of Original System	36
2.1.2 Objectives in Electronic Development	40

CHAPTER 2 (cont'd)	<u>Page No.</u>
2.2 General Description of Present Tomogram Electronics	42
2.2.1 Method of Operation	43
2.3 Descriptions of Circuits	44
2.3.1 Pulse Generator	44
2.3.2 Pulse P9 Modifier	49
2.3.3 Pulse P5A Modifier and Oscillator	51
2.3.4 Bone Side Driver Amplifier	53
2.3.5 Reference Driver Amplifier	55
2.3.6 Isolator Preamplifiers	57
2.3.7 Bone Side A.G.C. Amplifier	59
2.3.8 Reference Amplifier	62
2.3.9 Final Amplifiers	64
2.3.10 Bias Control System	64
2.3.11 Discriminator	69
2.3.12 Motor Switch Circuit	72
2.3.13 The Motor	74
2.3.14 Transducer Housings	75
2.4 Conclusions	75
<u>CHAPTER 3: BIAS THEORY</u>	80
3.1 Consideration of Time Constants	81
3.1.1 Bias Acquisition Time	81
3.1.2 Filtration Time Constant	82
3.1.3 Sample and Hold	82
3.1.4 Actuation Time	83
3.1.5 Amplifier Response Times and Phase Shifts	83
3.2 Bias Theory	84
3.3 Conclusions	90

	<u>Page No.</u>
<u>CHAPTER 4: INTRODUCTION TO DIFFRACTION THEORY</u>	92
4.1 Introduction	93
4.2 Green's Functions	95
<u>CHAPTER 5: RADIATING DIPOLE</u>	99
5.1 Derivation of Radiating Dipole Green's Function	100
5.2 Theoretical Results	106
5.3 Experimental Results	119
5.4 Conclusions	123
<u>CHAPTER 6: PARTICLE VELOCITY</u>	126
6.1 Derivation of the Particle Velocity	127
6.2 Consideration of Resultant Particle Velocity	131
6.3 Conclusions	137
<u>CHAPTER 7: DIFFRACTION FRONTS</u>	140
7.1 Diffraction Fronts	141
7.1.1 Derivation	141
7.1.2 Results	144
7.2 Energy Intensity	148
7.2.1 Derivation	148
7.2.2 Results	149
7.3 Corollary of Diffraction Front and Intensity Theory	153
7.4 Conclusions	155
7.5 General Conclusions of Diffraction Theory	157
<u>APPENDICES</u>	159
Appendix 1: Transmission Line Model for Attenuation in a Fluid	160
A.1.1 Introduction	160
A.1.2 Theory	161

	<u>Page No.</u>
APPENDICES (cont'd)	
A.1.3 Results	164
Appendix 2: Initial Bias System	166
A.2.1 Description	166
A.2.2 Initial Bias System Theory	166
Appendix 3: Frequency Response of Transducer Coupling	171
A.3.1 Coupling between Driver Amplifier and Transducer	171
A.3.2 Coupling between Transducer and Preamplifier	172
Appendix 4: Investigation of Computing Costs	176
A.4.1 Estimation of Computing Costs for Zemanek Algorithm	176
A.4.2 Estimation of Computing Costs for New Algorithm Using Huygen Green's Function	178
A.4.3 Estimation of Computing Costs for Lockwood and Willette Algorithm	180
Appendix 5: Publication	181
REFERENCES	189

LIST OF TABLES, FIGURES, PHOTOGRAPHS

	<u>Page No.</u>
Plate 1.1 The Ultrasonic Tomogram	20
Fig. 1.1 Tomogram Scan Angles	30
Table 1.1 Comparison with Bodyscanners	32
Plate 2.1 Transmitted Wave Train	39
Fig. 2.1 Block Diagram of Electronics	37
Fig. 2.2 Pulse Generator	45
Fig. 2.3 Pulse Shapes	48
Fig. 2.4 Pulse P9 Modifier	50
Fig. 2.5 Pulse P5A Modifier	52
Fig. 2.6 Oscillator	52
Fig. 2.7 Bone Side Driver Amplifier	54
Fig. 2.8 Reference Driver Amplifier	56
Fig. 2.9 Bone Side Isolator Preamplifier	58
Fig. 2.10 Reference Isolator Preamplifier	58
Fig. 2.11 A.G.C. Amplifier	60
Fig. 2.12 Graph of V_s vs log GAIN for A.G.C. Amplifier	61
Fig. 2.13 Reference Amplifier	63
Fig. 2.14 Final Amplifiers	63
Fig. 2.15 Bias Control System	65
Fig. 2.16 The Discriminator	70
Fig. 2.17 Motor Switch Circuit	73
Plate 2.2 Transducer Housing	76
Fig. 2.18 Transducer Housing	77
Fig. 3.1 Bias System	84
Fig. 4.1 Geometry of General Surface Integral	93
Fig. 4.2 Green's Functions	96
Fig. 4.3 Boundary Condition of Radiating Dipole	98

	<u>Page No.</u>
Fig. 5.1 Single Dipole	101
Fig. 5.2 Transform Geometry	103
Fig. 5.3 Huygen Three Dimensional Diffraction Field	107
Fig. 5.4 Kirchhoff Three Dimensional Diffraction Field	108
Fig. 5.5 Radiating Dipole Three Dimensional Diffraction Field	109
Fig. 5.6 Alternative Views of Radiating Dipole Field	110
Fig. 5.7 Alternative Views of Radiating Dipole Field	111
Fig. 5.8 Axis Plots	113
Fig. 5.9 Cross Plots	114
Fig. 5.10 Ring Transducer Cross Plot	116
Fig. 5.11 Ring Transducer Axis Plot	117
Fig. 5.12 Three Dimensional Ring Transducer Diffraction Field	118
Plate 5.1 Experimental Investigation of Huygen Function	120
Fig. 5.13 Experimental Huygen Axis Plot	122
Fig. 5.14 Computed Huygen Axis Plot	122
Fig. 6.1 Cross Plot of Radiating Dipole Particle Velocity	130
Fig. 6.2 Elliptic Nature of Resultant Particle Velocity	133
Fig. 7.1 Particle Velocity Vectors	142
Fig. 7.2 Radiating Dipole Diffraction Fronts	145
Fig. 7.3 Nearfield Diffraction Fronts	146
Fig. 7.4 Comparison of Diffraction Fronts	147
Fig. 7.5 Huygen Diffraction Energy Field	150
Fig. 7.6 Kirchhoff Diffraction Energy Field	151
Fig. 7.7 Radiating Dipole Diffraction Energy Field	152

	<u>Page No.</u>
Fig. 7.8 Alternative View of Radiating Dipole Energy Field	154
Fig. A.1.1 Transmission Line Model	161
Fig. A.1.2 Graph of α vs f for Transmission Line Model	165
Fig. A.1.3 Graph of C^r/c_0 vs f for Transmission Line Model	165
Fig. A.2.1 Initial Bias System	167
Fig. A.2.2 Equivalent Circuit for Initial Bias System	169
Fig. A.3.1 Equivalent Circuit with Transducer Transmitting	171
Fig. A.3.2 Equivalent Circuit with Transducer Receiving	172
Fig. A.3.3 Frequency Response of Transducer Coupling	174

P.1 Introduction

This thesis is a study of some applications of ultrasonics to Medical Physics. The two major applications dealt with are: the development of an ultrasonic tomogram to be used in conjunction with an x-ray densitometer to investigate bone mineral content in vivo, and the formulation of a new transducer diffraction theory more closely allied to those conditions found in medical ultrasonography.

P.2 Bone Densitometry

A method to assess bone mineral content in vivo which causes minimal biological damage is of great clinical importance in the study of bone diseases such as osteomalacia, osteoporosis, hyperparathyroidism, rickets, and disturbances of the renal system, where the calcium or phosphorus content of the bone has been altered. Of these, osteoporosis is the most common bone disease in the U.K. (Fourman, 1960), whilst osteomalacia is much less common in those countries where an adequate diet is eaten. In osteomalacia, there is a lower calcium absorption from the intestine which is usually due to a vitamin D deficiency. This causes incomplete calcification of the bone matrix giving a reduction in the mineral content per unit volume of bone.

If there is too little bone matrix, but the matrix is impregnated with the normal calcium salt content, the condition is called osteoporosis, and is often a manifestation of ageing (senile osteoporosis). Nordin (1964) has suggested that the primary cause is a long term calcium imbalance. The other diseases mentioned all result in a low calcium content of the bone, and are discussed in detail by Fourman (1960).

The effects and causes of all these diseases may be studied by in vivo bone densitometry, and the effect of chemotherapy may also be studied if the method of densitometry may be used serially. In the past, some purely ultrasonic methods to study bone mass have been tried, notably Rich et al (1965), Cameron et al (1969) and Jurist (1970), but with varying success, and a great deal of inaccuracy. All of these have been superseded by easier and more accurate methods employing computed x-ray tomography (Hounsfield, 1973, Ambrose, 1973, Perry and Bridges, 1973, Elsasser and Reeve, 1980). These methods have been investigated at great length, and a section is presented in the next chapter in which the accuracy of such machines as the Emiscanner is compared with the method developed at Aston.

Work has been carried out over the last ten years in the Physics Department at Aston University, and at Dudley Road Hospital, Birmingham, with the purpose of improving techniques for the study of decalcification in vivo. It is intended that instrumentation be developed in order to determine the actual mineral density at each point of a selected bone, the ulna being chosen in the present case.

The ulna was chosen as it has the advantage of being a peripheral part of the body which can be moved without too much difficulty. This is important in the case of elderly people who may be arthritic. The site was chosen to be about 30 mm from the ulnar styloid, where the bone would have an approximately annular cross-section, and the amount of subcutaneous fat and muscle around the bone is minimal, which is an advantage when small calcium differences between successive scans are sought. Although the lumbar vertebrae may give a more sensitive reflection of total skeletal calcium than the ulna, both the radius and the ulna have been found to reflect the degree of mineralisation of the

remaining skeleton (Virtama et al, 1965, Helela et al, 1969, 1970, Rusch and Virtama, 1972).

The technique devised at Aston requires two necessary steps so that values of bone mineral density may be quoted to a high degree of accuracy:

- 1) The first step is to determine the total amount and site of bone minerals at each point across the ulna. This has been achieved by using an x-ray absorption scan.
- 2) The second step is to determine the path length through the bone at each point of the x-ray scan. This could be obtained from an accurate outline of the ulna cross-section at the level at which the absorption scan has been performed, and is to be obtained by ultrasonic tomography.

The first part of the bone densitometry method, i.e. the total bone mineral estimation using x-ray scanning techniques, will now be dealt with briefly.

P.2.1 The X-Ray Densitometer

An apparatus for bone mineral estimation in vivo has been developed by Edwards (1973) and Archer-Hall et al (1973, 1978). Further modifications have been carried out by Al-Jarallah (1976, 1978). This apparatus has been designed so that the beam from a conventional diagnostic x-ray set falls on a lead plate with two slots. Beneath one of them is a monitor detector to sample the radiation. The other beam passes down into a water bath designed to accommodate the patient's arm firmly in such a manner that the ulna is scanned. The bath and arm are moved through the beam in a smooth motion by a worm drive at the rate of 1 cm/sec. The transmitted beam passes through a defining slit to a second detector. The detectors are small pieces of Cs I (Tl) viewed by

photo-cells. The light output of the crystals is sufficiently great that a d.c. current, rather than a series of pulses, is obtained.

This apparatus performs an x-ray absorption scan with a spatial resolution of 0.25 mm and negligible positional error, without discomfort to the patient. It also has a number of advantages:

- 1) It can provide an extremely accurate analysis of the extent and site of bone minerals in the skeleton of the living patient, especially in the ulna.
- 2) The x-ray dosage to the patient is very low, approximately 150 mRads per scan, which is about one tenth of that used in taking a radiograph of a whole limb. Hence repeated scans may be performed at, for example, monthly intervals to determine response to therapy.
- 3) The short scan time of a few seconds means that distortions of the observed profile due to patient movement are minimised.
- 4) The apparatus is made to fit to an unmodified clinical x-ray set, but avoids the difficulties associated with photographic procedures which have been used before (Johns, 1961).
- 5) It provides a compensation for the variations in x-ray intensity and spectral distribution due to fluctuations in the mains supply voltage. This is achieved by the use of a monitor detector and electronic switching techniques, so as to result in an overall error not exceeding 1.5%.

The principle of operation of this apparatus and its compensation for variations in x-ray intensity are summarised as follows:

The photocurrents from the monitor and lower detectors are simultaneously integrated with respect to time from the start of each half cycle of the mains supply. The integration is performed for a period of time "t" until the result obtained from the current of the

monitor detector reaches a preset value. This value is selected so that the time of integration "t" will be about $1/200^{\text{th}}$ of a second. If the mains supply voltage, and hence the x-ray output, is high, then the time of integration required to reach the preset value will be shorter, and vice versa. When this preset value is reached, electronic switching causes the integration of the second current from the lower detector to stop, and the value of the integral is held and fed out to give a y-deflection on an oscilloscope screen. At the end of each half cycle, both integrators are reset to zero and the procedure is repeated.

The voltage for the x-deflection of the oscilloscope is obtained from a tracking potentiometer whose roller contact moves with the system carrying the limb. The oscilloscope trace of the ulna is thus made to give a graph in which increase in ordinate indicates an increase of the bone minerals, abscissa being a measure of distance across the ulna.

The calibration of the vertical scale was initially provided by a reference step wedge made of ivory, but this has been replaced by one made of an artificial bone-like material developed by Bashter (1976). This material has the advantages that it is homogeneous, does not absorb water, is easily machinable, and has a precisely known elemental composition. The wedge ranges in thicknesses from 3 mm to 13 mm in 1 mm steps, and is placed in the water bath beside the limb so as to be scanned in the same way as the ulna.

P.2.2 Bone Tomography

Once the x-ray densitometer has provided an estimation of the amount and site of bone mineral at each point across the ulna, it is

necessary to determine the corresponding path length through the ulna in order to calculate the actual bone mineral density. The required path lengths can be obtained from an accurate outline of the cross-section of the ulna at the same level as the x-ray scan, by using a tomogram.

It was decided to use an ultrasonic tomogram employing an echo-timing technique as the resolution of x-ray tomographic methods at that time was insufficient, as has been explained extensively by Bashter (1976). Ultrasonic radiation has been utilised by many workers for the purpose of visualisation and localisation of tissue interfaces by using the pulse echo-ranging technique, notably Wild et al (1951), Howry et al (1956, 1957), Donald and Brown (1961), Freedman (1962), Kossoff et al (1963, 1964, 1965, 1966, 1968, 1971), Wells (1963, 1969, 1972, 1977, 1979), Robinson et al (1966), Fry et al (1968), Gore and Leeman (1977) and many others.

The original aims of the project were twofold. The first aim was to develop the ultrasonic tomogram so that it could be used in conjunction with the x-ray densitometer for clinical investigations of bone mineral content. The second aim was to build an instrument whose resolution was much higher than that obtainable with present plotting systems, and to try to develop this to its practical limit.

P.2.2.1 Stages in the Evolution of Tomogram Design Concepts

These were as follows:

- 1) It was realised that the soft tissue to bone interface gives the highest reflectance of any in living tissue, except soft tissue to air.
- 2) The longitudinal resolution of a pulse echo-ranging technique

depends on the accuracy of the electronic timing system used.

- 3) The lateral resolution can be maximised if a large aperture bowl transducer is used for sending and receiving the pulse.
- 4) The high resolution can only be maintained if the bowl focus is kept on the reflecting surface.
- 5) A servomechanism could be made to drive the bowl in and out, keeping its axis in the radial line of a rotating drum system.

The focus could thus be kept on the reflecting surface, while the whole system is rotating around the centre of the bone. The information for control of the bowl servomechanism could be obtained from the pulse echo time.

- 6) It would be better to compare the echo time with that of a fixed reference system rather than to time the reflection against an oscillator clock. The reference system would involve an identical transducer and a rod reflector, whose cylindrical radius was about the average of that of the bone. If the reference and bone systems were in the same water bath, this would automatically remove error due to changes in the velocity of propagation of the pulses as a result of changes in temperature of the water surrounding the limb.

- 7) It was realised that a direct writing system could be used to draw an enlarged picture of the outline of the bone cross-section. This became clear once the concept of moving the transducer around the bone had been established, with a rotation of an angle θ say from a start position, and in a radial direction so that the focus is at a distance r from the centre of rotation.

P.2.2.2 Elaboration of Concept 2

In the original system, it was thought that the cessation of a pulse

7MHz square envelope pulse could be used as an "event", but this was shown not to be the case. It was also thought to be acceptable if the electronics of the time discriminator were capable of responding in $1/14^{\text{th}}$ μs , i.e. one half cycle of the period of the 7 MHz pulse. If this were so, the system would be able to detect a change of echo path, $2d$, of about 0.1 mm. Thus the least detectable distance error would be 0.05 mm.

The frequency of 7 MHz was chosen as a compromise between resolution and attenuation, as a higher frequency would provide better resolution, but the returning signal would be so attenuated that it would be lost in the electronic noise. Originally, it was thought that a bowl resonant at 1 MHz could be driven at its seventh harmonic to provide a suitable signal. However, this proved to be unsatisfactory, and it was eventually decided to use a bowl resonant at 2.2 MHz, and to drive it at its third harmonic, or second overtone, which is a little more than three times the resonant frequency, i.e. it is 6.85 MHz.

In the present system, it has been shown that for a given amplitude, the rise time of a signal obtained by acoustic reflection can be less than one quarter of the resonant period of the transducer used. This is achieved by shock excitation, i.e. the application of a 20 volt pulse with a rise time of about 50 ns.

Support for the accuracy of echo timing methods has been provided by the work of Gore and Leeman (1977) and Leeman (1980). Leeman has shown that where there is a variation of attenuation and velocity with frequency (as for waves in tissue) that a short duration pulse $f(t)$ applied by a transducer can be expressed in terms of two integrals, after the pulse has propagated a finite distance.

The first of these integrals can be shown to be of the same shape

as $f(t)$, but attenuated, and will travel at that velocity for which attenuation would be zero. The second arrives later than the first, and has been described as "rumble".

It is therefore evident that if $f(t)$ can be very sharp, and the receiving system be made to respond to this, then accurate timing can be obtained with no confusion due to the lower frequency components of the pulse. Examination of Leeman's work shows that this is only valid when the dispersion is such that the velocity of propagation increases with increase of frequency.

Attenuation in tissue tends to be proportional to frequency, whereas in pure liquids it is generally lower in magnitude, but proportional to the square of frequency. A model for a fluid has been considered analytically in Appendix 1 having attenuation proportional to the square of frequency, in which it is shown that, as in tissue, it is the high frequency components of the pulse for which the velocity is greatest.

P.2.2.3 Aims of Present Research

The objective of the practical part of the present project on the ultrasonic tomogram was to improve the electronics of the system so that it would be able to follow the outline of an object where the axis of the ultrasonic beam makes a moderate angle (i.e. about 40°) to the normal at the reflecting surface. This improvement would allow the system to accommodate weak signals caused by attenuating tissue or oblique angles of reflection. It was hoped that the tomogram would be working well enough for a subsequent project to be started involving clinical trials of the two machines.

Although the tomogram has worked and traced several objects to the

degree of resolution expected, no reproducible results were obtained as one transducer failed shortly before the project was to have ended.

A detailed description of the x-ray bone densitometer may be found in Edwards (1973) and Al-Jarallah (1976), and will not be further expounded as no other improvements to this apparatus have been required. A full introduction to the ultrasonic tomogram, including basic design concepts and method of operation, is given in the next chapter. The rest of this preface will deal with the other major application of ultrasonics to Medical Physics investigated, namely the formulation of a new transducer diffraction theory.

P.3 Transducer Diffraction Theory

The complete description of the acoustic field produced by an ultrasonic transducer is generally divided into two parts: the nearfield (Fresnel) region characterised by interference phenomena, and the far-field (Fraunhofer) region characterised by an interference-free sound field. The basic applications of ultrasonics to Medical Physics were laid down by Kossof et al (1968), in which they shed practical light on the complexity of the beam patterns within the nearfield, and until recently, most theoretical works have tended to avoid this region for the very same reason. As most ultrasonic imaging techniques in Medical Physics work within the nearfield, there is a great need for a better understanding of the diffraction phenomena in this region, especially the phenomena that relate directly to the sort of transducers used in medical ultrasonography.

The steady-state radiation patterns of ultrasonic transducers in the nearfield may be investigated theoretically by two alternative approaches. Of these, the most widely used to date involves a surface

double integral of a Green's function taken over the transducer face to satisfy the relevant boundary conditions. This technique, initially developed by Lord Rayleigh (1926) for the infinitely baffled disc, can be used to give the acoustic pressure distribution in both the near-field and farfield for various transducer configurations. Rayleigh's integral, which can also be called the Huygen integral (Baker and Copson, 1939), has been analytically evaluated for certain parts of the field and certain values of the frequency and transducer width by McLachlan (1932), Stenzel (1939, 1952), Seki et al (1956), Freedman (1960, 1970, 1971, 1972, 1977) and Frederick (1965). These have usually involved either circular or rectangular pistons. Computation of the sound field was first achieved by Zemanek (1971), and a single integral computer method involving impulse response in which the steady-state field was eventually computed was presented in 1973 by Lockwood and Willette.

Archer-Hall et al (1978) presented a geometry to convert the steady-state Huygen integral and the Kirchhoff integral (which applies to a different set of transducer boundary conditions) into single integrals with fixed limits, which were easily evaluated by computer.

Another representation of the pressure field of the circular piston was developed by Schoch (1941) from the Kirchhoff surface integral, in which he transformed the expression into a line integral. This has subsequently been used by Carter and Williams (1951) to develop a series expansion, and by Dehn (1960) to investigate maxima and minima, but no full computation of results has been presented to date.

During this time, there has been some parallel research into the alternative approach first developed by King (1934) which gives a single integral representation of the field by an integral transform technique. Oberhettinger (1961) showed that King's integral can be derived from Rayleigh's, and hence describes a transducer of Huygen type boundary

conditions. Further analytical work has been carried out by Williams (1964) and Greenspan (1979). Archer-Hall and Hutchins (1980) approached the problem using a concept suggested by King's integral and used a Bessel series in which the constants were initially considered arbitrary, and were determined by a simultaneous equation technique enabling the whole series to be fitted to prescribed boundary conditions. The series found to be most suitable was of the Schlömilch form (Watson, 1966).

Another area investigated more recently has been in the techniques of impulse and transient response from piston radiators, led principally by Stepanishen (1971, 1974, 1976, 1978), Freedman (1970, 1971, 1972, 1977) and Robinson et al (1974). The advantage of these techniques is that the solutions are more amenable to investigation of different transducer configurations, as shown by the work of Penttinen and Luukkala (1976) and Weyns (1980), the disadvantage being that the only boundary conditions being considered are those corresponding to a Huygen type integral.

Nearly all of the work to date has been involved with the investigation of the rigid, infinitely baffled transducer, which usually requires some evaluation of the Huygen surface integral. The boundary conditions of this type of transducer are well known, as is the Green's function in the corresponding surface integral. The other integral occasionally investigated is called Kirchhoff's integral, and the boundary conditions that this applies to are not so clearly understood in the literature. Spence (1949), for example, refers to the Kirchhoff as an approximation of the Huygen integral, whereas they are distinctly separate entities. Archer-Hall et al (1978) compute the pressure field of the Kirchhoff integral, but make little comment of the boundary conditions to which it applies.

There were two original objectives of the theoretical work for this thesis. The first aim was to examine closely the boundary conditions of the two Green's functions mentioned as well as those of the Radiating Dipole function, as it was believed that the latter would describe the boundary conditions found in Medical Physics more closely than either the Huygen or Kirchhoff functions. The second objective was to compute the pressure field of the Radiating Dipole function employing the geometrical transform used by Archer-Hall et al (1978). Although this function is well known in electromagnetism (Grant and Philips, 1975) and analytical acoustics (Morse and Feshbach, 1953; Morse and Ingard, 1968), never before had it been developed into a suitable form amenable to computation. It was found that better understanding of the Kirchhoff boundary conditions followed from a clear definition of the other two, as it was shown that after geometrical transformation the Kirchhoff was in fact a mixture of the Radiating Dipole and Huygen functions.

As work progressed, it was realised that the single integral forms of the acoustic potential for all three Green's functions could be differentiated under the integral sign before computer integration, and would thus yield expressions for the normal and radial components of particle velocity.

Further investigation and computation revealed that the resultant particle velocity must be described as an elliptical vector. This concept has not been realised before anywhere in acoustic diffraction literature.

Once this property was confirmed, the problem of how to present this information graphically had to be overcome. This was achieved by the introduction of the concept of "diffraction fronts", by considering the direction of energy flow at a general point anywhere in the

diffraction field. This allowed the illustration of the changing direction of the resultant particle velocity in the field, and a further theoretical step was made to depict the magnitude of this resultant by plotting energy intensity.

The results of computations of the sound pressure field for the three functions mentioned have been illustrated in three dimensional computer plots similar to those obtained by Zemanek (1971) and Lockwood and Willette (1973), and it has been shown that the computing "costs" and errors of the new algorithm are significantly lower than these previous techniques. A simple acoustic experiment is also presented whose results agree with those of all the surface integral techniques involving the Huygen integral. The normal component of the particle velocity across the face of the disc has been found to confirm the boundary conditions of all three functions.

Although nearly all of the computational and theoretical work in this area is now complete, the three dimensional plots of energy intensity show some interesting features which indicate the need for further investigation.

Thus it may be seen that the original aims and objectives of the thesis were predominantly practical, and that not all of these were completely achieved. However, what originally began as a small theoretical investigation has provided far more information than expected, and has involved the development of new concepts and viewpoints in ultrasonic diffraction theory.

Introduction to Ultrasonic Tomography

Chapter 1

1.1

CHAPTER 1

Introduction to Ultrasonic Tomogram

1.1.1

1.1.2

1.1.3

1.1.4

1.1.5

1.1.6

1.1.7

1.1.8

1.1.9

1.1.10

1.1.11

1.1.12

1.1.13

1.1 General Introduction

In this chapter, the possibility of using ultrasonics to determine the cross-sectional profile of the ulna will be discussed. The basic requirements and concepts for the construction of such a machine will be outlined, and the accuracy of the complete densitometric system compared with other purely radiographic techniques.

The use of ultrasonics in diagnostic imaging is generally divided into two techniques. Doppler techniques (Wells, 1977, 1980, Maginess, 1979, Bow et al, 1980, Hall, 1980, Woodcock, 1980) are usually employed to investigate dynamic phenomena such as blood flow, heartbeat and abdominal dynamics. Pulse echo-ranging methods investigate site, shape and content of stationary lesions or foreign bodies. A variation of the latter technique was chosen in the present case to investigate the ulna.

The principle of pulse echo-ranging is that a train of short duration pulses is transmitted from the transducer in a known direction into the patient. When the pulse meets a boundary separating two media of differing acoustic impedances, part of its energy (depending on this difference) is reflected back. The returning echo is usually received by the same transducer acting as a detector during the period between successive transmitted wave-trains. The information obtained from the echo is the direction of the original beam, and the time that it takes to return. The former indicates the direction of the reflecting interface, and the latter gives a measure of the distance between this interface and the transducer surface.

One of the factors of significance to the use of ultrasonics in medicine is the marked differences of acoustic impedances at a bone-soft tissue interface. This impedance difference is the greatest of any tissue interface in the human body. The mean value of acoustic

impedance (ρc) for human tissue is about $1.63 \times 10^6 \text{ Kg m}^{-2}\text{s}$, and that for bone is about $7 \times 10^6 \text{ Kg m}^{-2}\text{s}$. Hence, an amplitude reflection of about 62% could be obtained at a bone-soft tissue interface.

The principle objective of the ultrasonic tomogram worked on by Bashter (1976), and continued in this thesis, is to ignore all information from minor reflections at tissue-tissue interfaces, and to act only on the large reflection from the single bone surface interface, as this is the only information required in the present case. This method to increase resolution is a major departure from the more usual ultrasonic tomographic techniques (Greenleaf et al, 1974, 1975, Carson et al, 1976, Glover et al, 1977, Mueller et al, 1979). These techniques use planar transducers in an attempt to display the full cross-section of the part of the body being investigated, and to include reflections from all interfaces within that cross-section. As further spatial information from these minor reflections is ignored in the present case, the resolution of this ultrasonic tomogram can be increased beyond that of others, almost to its limit.

The limit of resolution of any ultrasonic echo-ranging technique depends on two factors, the longitudinal and the lateral resolution. The lateral resolution of the system will depend on the diffraction pattern of the transducer used. In the present case, a bowl transducer has been chosen to maximise lateral resolution, as this is far greater for the bowl than for the planar transducer when the bowl is investigating a reflection at its focus. However, to maintain this high lateral resolution, the interface under examination must be kept at the focus of the bowl, and this has required the incorporation of a servomechanism to move the bowl radially to maintain focus and hence lateral resolution. The longitudinal resolution will depend on the accuracy of the electronic

timing system used to maintain the bowl in focus. As the choice of transducer configuration has been made to maximise lateral resolution, it may be seen that the total resolution of the system will depend on the electronic timing to a great degree.

When the author began the present project, the mechanical construction of the tomogram had been completed and was satisfactory, and a suite of electronics had been designed, tested and built. However, the tomogram did not work consistently, nor did it trace objects to any degree of resolution expected. This failing was believed to be principally due to the design of the electronics. The main aim of the practical work on the ultrasonic tomogram in this thesis was thus to improve the electronics to obtain the desired resolution required for accurate bone densitometry. Specific failings of the initial electronic designs will be explained in greater detail in the next chapter.

1.2 General Description of Present Ultrasonic Tomogram

The ultrasonic tomogram (see plate 1.1) involves two matching ceramic bowl transducers (PZT-5A) attached vertically to the bottom of a rotating drum, in which all the electronic circuit elements are mounted. One transducer is to be used as a reference, and the other is to be used as the scanning or "bone" transducer. Both transducers are immersed in a water bath designed to accommodate an arm vertically through a rubber cuff in the base of the bath, without discomfort to the patient. The limb is held normal to the axis of symmetry of the scanning transducer, in such a way as to allow for a smooth rotation of the transducer around the limb. The time for a complete rotation of 360° is about 33 seconds.

An electronic switching technique is used to turn on both transducers as transmitters. The bone transducer transmits a long duration



Plate 1.1. The Ultrasonic Tomogram

pulse (about 110 μ s) of 6.85 MHz ultrasonic waves, with a shock excitation, or impulse, at the end of each pulse, i.e. at 120 μ s. The reference transducer does not transmit the long duration pulse, which is called the pilot wave, for reasons that will be discussed in the following chapter, but does transmit the impulse at 120 μ s, in synchronisation with the bone transducer. Each transducer is then switched electronically to act as a receiver for the corresponding returning echoes. The pulses are transmitted 500 times a second. The difference in the delay times of the two received impulses, which is proportional to the difference in their path lengths, is obtained by amplifying them and feeding them into a discriminator, which determines which of the two impulses returned earliest. The information from the discriminator provides the input for a servomechanism designed to maintain the scanning bowl focus on the bone surface by appropriate radial movement.

The display system involves a direct mechanical coupling of the servomechanism to a pen recorder on top of the machine, which is driven through a 10:1 wormbox, as opposed to the 100:1 wormbox of the bowl transducer servo drive. Thus the pen will draw a ten times full size outline of the ulna, after suitable calibration on a regular surface of known dimension. The electronics and associated servo motor are supplied with power through two large copper slip rings on the top and bottom of the rotating drum. The d.c. supply to the slip rings is only 20 volts, thus there is no risk of electric shock to the patient.

In this technique, the outline of the ulna cross-section will be obtained using two separate scans, each of 275°, one with the arm pronated, the other with the arm in the supinated position. This is

necessary to obtain that part of the ulna profile shadowed from the transducer by the radius when only one scan is performed. The two scans will be combined to give the complete outline of the cross-section of the ulna. The time for each scan will be about 25 seconds.

1.3 Basic Concepts of the Ultrasonic Tomogram

The main overriding objective that will govern all basic design concepts is that the machine is meant to determine the cross-section of the ulna to a high degree of resolution by using ultrasonics. An ultrasonic tomogram will find a cross-section using ultrasonics, but the other design concepts that will affect resolution require further discussion and explanation, and consideration of these will highlight the reasons behind the construction of the ultrasonic tomogram just described.

1.3.1 Choice of Transducer Configuration

Most of the previous techniques used in diagnosis involve a broad beam of large ultrasonic field depth, using plane transducers. Since the resolution of fine detail requires examining a small area of the scanned bone, the system must imply as small a beam width as possible. These conditions may be achieved by using a converging beam of ultrasonics with a sharp focus. Therefore it has been decided to use a spherical concave transducer in a bath of water surrounding the limb, and a technique to maintain its focus on the bone surface. This choice will provide a high degree of lateral resolution, a source of major loss of accuracy in general diagnostic echo-timing techniques.

A theoretical investigation of bowl resolution by Bashter (1976) and Archer-Hall (1980), using a new technique, has revealed that the accuracy of a bowl with its diameter equal to its focal length is

higher than that predicted by the usual Huygen integral. It was also shown in these works that the focus of an ultrasonic bowl transducer was not a point but a small, approximately cylindrical volume centred about the centre of curvature, and that maximum resolution could only be maintained if the surface or interface being scanned was kept within the bounds of this volume. This implied the need for a servomechanism and associated electronics to use the information obtained from the bone reflection, not only to keep the transducer in focus for the following reflection but also to plot the outline of the ulna.

From these previous considerations, the focal length and diameter of the bowl were both chosen to be about 10 cm. The large aperture of the transducer, besides giving a higher resolution, would also enable a greater proportion of the reflected ultrasonic waves to be collected when the transducer operates as a detector. Unsuccessful attempts have been made by Bashter to fabricate a bowl transducer of the required aperture and radius of curvature, and it had been decided to use the largest bowl commercially available. This was of about 5 cm diameter, 10 cm in focal length, and the difference between the two theoretical diffraction patterns in this case was not too marked.

1.3.2 Timing System

In order to obtain a scan of the ulna cross-section, it is necessary for the transducer to move around the arm to examine a series of points on the surface of the bone at the required level of cut. While the transducer is moving in its circular path, the echoes from the reflecting targets on the bone surface are received at delay times proportional to their distances from the centre of the transducer.

There are two systems by which the distances of the targets from

the transducer can be determined:

- (1) a timing mechanism, or
- (2) a reference system.

A timing mechanism, such as a quartz crystal oscillator, needs a calibration from a known velocity of sound in the coupling medium (water). As the velocity of sound is temperature dependent (Kossoff et al, 1964), any variation in the water temperature is equivalent to changing the time of the ultrasonic path. For instance, 10°C change in temperature gives a change in velocity of about 35 ms^{-1} . This is equivalent to about 2.4 mm change in path length over 100 mm.

The error due to variation of sound velocity could be overcome by using a reference system in the same water bath. This system consists of a concave bowl transducer (exactly matching the scanning transducer) with a fixed reflecting rod present at its focus. Both the scanning and reference transducers are pulsed simultaneously to operate as transmitters. The returning echoes from the bone surface and reflecting rod are detected by the corresponding transducers at delay times proportional to their ultrasonic path lengths. As the distance between the reflecting rod and the reference transducer is always constant (equal to the radius of curvature), the echoes from the bone surface may arrive earlier or later than the reference echoes, depending on whether the target distance from the bone transducer is shorter or longer than the radius of curvature.

This system gives a method for the comparison of the delay times of the echoes from the bone surface, and hence removes the errors in range introduced by the change in velocity of ultrasound with water temperature.

Furthermore, with the case of shock excitation, the two echoes from

the bone and reference rod will have a similar shape, since they will have similar frequency spectra, which will make it feasible to compare the reflection times.

If consideration is to be given for precise location of the bone surface in the radial direction, i.e. a maximum axial resolution, it will be seen that this depends on the accuracy of assessment of the time interval between the two echoes detected by the scanning and reference transducers. Therefore the total resolution of the system will depend upon the electronics involved in this time discrimination.

1.3.3 The Scanning System

In order to preserve the required lateral resolution of the scanning transducer, its focus must be always maintained at the bone surface. This means that, during its circular movement, the scanning transducer must execute, in addition, a radial movement towards and away from the limb in order to keep the axial path constant in length. The information to do this can be obtained from the time interval between the two echoes detected by the scanning and reference transducers.

Therefore, provision must be made for movement of the bone transducer in:

- (1) a circular movement around the limb, and
- (2) a radial movement towards and away from the limb, so as to maintain its focus on the bone surface.

If all positional information concerning the profile of the bone is given in terms of radial movement, the circular movement can be kept at any constant speed.

1.3.4 Information to control the Radial Movement

It is intended to determine the path difference by the comparison of reflection times from the reference and scanning transducers and their respective targets for a distinct event. It is necessary for the comparison of the two echo pulses that they are amplified to be of about the same value before applying them to the discriminator. This is necessary for two reasons. The first and most important reason is that if the two impulses return simultaneously, i.e. the bone transducer is in focus, it is required that the two signals cancel to maintain a three state servo system. The second reason is that if the timing is to be judged by an indeterminate part of the rise of each impulse, an error may be involved when the two signals are very unequal as the slopes (i.e. the time taken to rise to a certain voltage) will be different.

Any system to be used in this manner requires the receiving amplifier dealing with the bone signal to have a variable gain to allow for change of the reflected signal. A voltage signal controlling the gain could be derived from a continuous wave-train transmitted before the event.

In the original scheme, it was intended to obtain the event from the abrupt cessation of a continuous wave. For accurate assessment of the time intervals, the wave-trains should be sharply terminated, which requires that the delay times of the transducers must be as short as possible. Considerable work has been carried out with regard to the construction of backing and matching layers (Bashter, 1976), but the cessation of the wave-trains could not be made abrupt enough to provide distinct events.

This difficulty was overcome by using a shock excitation, with a sharp onset, after the end of the transmitted pulses. Further

consideration by the author of the use of these R.F. pulses as pilot waves led to the wave-train on the reference side only transmitting the impulse, as the reference signal received is always of the same size, and hence requires no pilot wave to carry information about signal size.

Recent work on mathematical models of pulse propagation in dispersive media (Dines and Kak, 1976, Gore and Leeman, 1977, Leeman, 1980) have revealed that a received ultrasonic pulse may have an associated time-extended "rumble" of associated lower frequency components which would cause an alteration in the pulse shape. This has been considered by the author in the light of the pulse excitations to be used with the ultrasonic tomogram, but no such rumble has been found by experimental inspection of received pulses. This does not necessarily invalidate the theory, as it predicts that the rumble may not be discernible for short pulses that only travel a short depth into the tissue before reflection occurs, and the ringing of the transducers used may have masked such a small phenomenon. However, this observation does show that, for the tissue depth and frequency of operation of the tomogram, this phenomenon does not cause any loss of accuracy in the echo-timing technique. A new transmission line model for attenuation in pure liquids, as opposed to tissue, is given in Appendix 1.

When the two received signals have been amplified to be of about the same value, they are fed into a discriminator circuit in order to determine which of the two pulses returns sooner. The information from the discriminator provides the input for a servomechanism which operates to maintain the focus of the scanning transducer on the bone surface by radial movement. The detailed operation of the servo-

mechanism and the electronic circuits of the apparatus will be discussed in Chapter 2.

1.3.5 Display System

The movement of the bone transducer as it goes around the limb follows the shape of the reflecting bone surface, at the level at which scanning is performed. The transducer could be made to draw its display as it goes by one of the following systems:

- (1) a remote external plotter of a pen on a chart,
- (2) a cathode ray tube,
- (3) a direct mechanical coupling of the transducer to a pen on a drawing paper, attached to the frame of the apparatus.

The accuracy of the result depends on the type of display used. For example, the remote display system involves r and θ , and the transmission of their values on to paper could give rise to both radial and angular errors in the plotting system. In the second system, the magnification ratio of the cathode-ray tube is limited by the size of the screen, and could also give a distorted picture. For a permanent record, it is necessary to photograph the cathode-ray display, which is a further expensive disadvantage of this system.

It would also be necessary to provide at least two further slip rings to convey the r and θ information to the plotter. Alternatively, this data could be transmitted on a radio wave carrier at some frequency different to those already used on the machine.

The direct mechanical coupling display system is therefore more desirable than the other systems for the following reasons:

- (1) The backlash error in the angular plot is zero.

- (2) The backlash error in the radial coordinate would be less than in a system with remote display.
- (3) Any desired magnification ratio can be achieved, so that the error in taking measurements due to the thickness of the plotting pen will be minimised by increasing this ratio.
- (4) It gives directly a permanent record of the display on drawing paper, without photography and its associated problems.
- (5) The drawing papers are much cheaper than photographic films.
- (6) The display system is cheaper than either of the other alternatives.

Therefore, the transducer is to be made to transfer its movement by a coupled screw drive to a pen writing on a paper attached to the frame of the apparatus. A suitable magnification ratio of the plot can be obtained by using suitable gear boxes.

1.3.6 The Use of Two Separate 275° Scans

In practice, the single complete rotation of a 360° scan of the ulna is impossible to achieve, since the radius bone presents a complete obstacle to the ultrasonic waves in front of some parts of the ulna surface. According to the anatomy of the limb (Gray, 1977), the relative position of the radius with respect to the ulna can be changed by twisting the forearm 90° - 120° while the elbow remains fixed.

Fig. 1.1 is a life-size section of the bones of the left forearm, seen from the hand, when the arm is supinated and pronated. In the

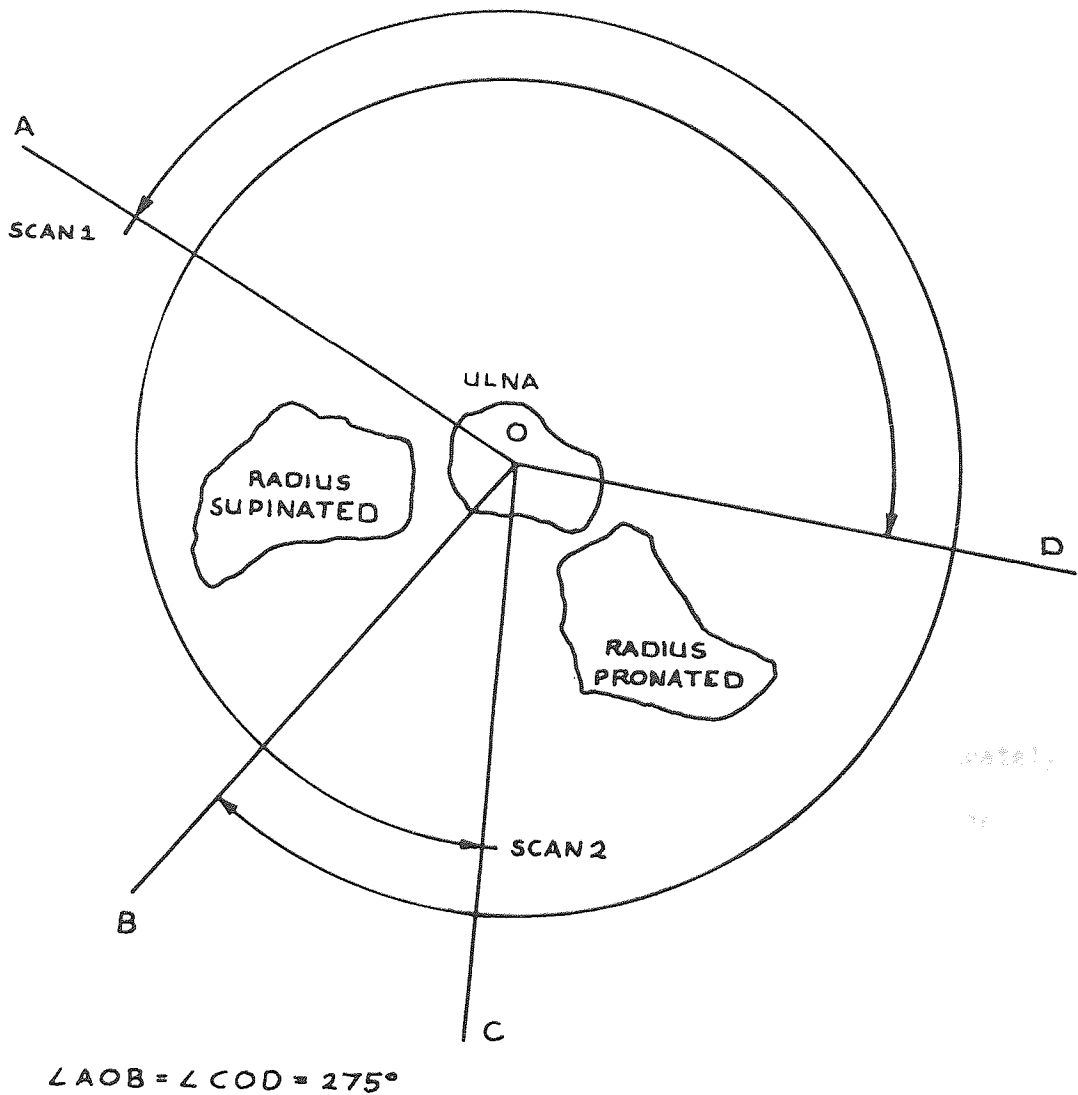


FIG.1.1.1 Tomogram Scan Angles

first position, the surface of the ulna shadowed by the radius is about $50^\circ - 55^\circ$. As can be seen from the figure, this angle is easily covered by the second scan. Thus the two plotted outlines may be superimposed in order to obtain the complete cross-section. In the case of an elderly patient who may only manage about a 90° rotation of the forearm, the technique is still valid, as there is a large overlap of the two scans (angle COB from Fig. 1.1).

1.4 Comparisons with Alternative Systems

It is feasible that the information required for in vivo bone densitometry could be obtained by using present X-ray tomography systems such as the Emiscanner. These could be arranged to give absolute absorption levels across the bone without the need of an outline of the cross-section. The relevant absorption levels for each resolution area would have to be compared with calibration pieces containing accurately known densities of bone mineral. It would then be possible for the computer plot to be given in terms of this bone mineral density.

The failure of early X-ray tomographic techniques to find an accurate enough outline has been extensively dealt with by Bashter (1976), so this will not be discussed. The viability of the bone densitometer and ultrasonic tomogram as one complete system will only be compared here with the latest computed tomography system.

There are four main types of Emiscanner, the brainscanner (such as the CT 1010), the basic bodyscanner (such as the 7020), the high resolution scanner (the 7020HR), and the very latest bodyscanner (the 7070 with nutating sensor geometry). These four were developed in the order in which they are placed.

The brainscanner can be disregarded for bone densitometry as the

main difficulty in fixing the ulna would necessitate the removal of the rubber water headbag, and modifications to use a different type of water bath. This is because the brainscanner takes no account of absorption in the path between scanner and patient, as this is filled with water. The brainscanner also gives the highest dose of all the Emiscanners (about 3 rads), which is another serious disadvantage. A water bath would not be required in all subsequent scanners, as a separate monitor X-ray beam is installed to account for absorption in the air path between scanner and patient. Thus, for the bodyscanner, all that would be necessary is a simple fixing bracket to hold the arm in place.

In the case of any computed tomography system, a compromise between resolution and scan time (and hence dose rate) has to be reached to suit the required conditions of operation. Of all the three bodyscanners mentioned, the high resolution scanner has sacrificed scan time and dose rate for more accurate spatial information, the basic bodyscanner is a commercially viable compromise for general hospital use, and the 7070 is another compromise, but with general improvements in beam geometry. Below is a table of these features compared with the ultrasonic tomogram/X-ray densitometer system, which is labelled US/X-ray.

Table 1.1 - Comparisons with Bodyscanners

System	Scan Time (secs)	Average Surface Dose (rads)	Spatial Resolution (mm)	Absorption Value Error (%)
70 20	20	0.5	1.0	± 0.5
70 20HR	60	1.5	0.5	± 0.7
70 70	3-30	0.5	0.8	± 0.5
US/X-ray	25	0.15	0.3	± 1.0

As can be seen from Table 1.1, the scan time of the system involving the ultrasonic tomogram and X-ray bone densitometer compares favourably against those for other bodyscanners. A short scan time reduces error due to patient movement, but may affect resolution, as not enough spatial information is obtained. This is the case for the 7070 scanner, and is an important disadvantage, as will be explained later.

In most cases, it is envisaged that only one scan of the ulna cross-section need be made of the patient using the ultrasonic tomogram, as the dimensions of the bone will not alter significantly. The bone densitometer will then be used to make the serial measurements of bone mineral content required. Thus, for the same allowed X-ray dosage, this system could be employed with about three times the frequency of a bodyscanner. This is more in keeping with the clinical requirements for the study of decalcification *in vivo*.

If one considers the ulna to have a width of about 10 mm, then the error of the ultrasonic tomogram due to spatial resolution will be about $\pm 3\%$, which is far better than any bodyscanner or alternative ultrasonic technique. As this value is much higher than the error of absorption values obtained with the densitometer, then the overall accuracy in the bone density will depend mainly on the spatial resolution of the tomogram. This will apply also to the bodyscanner systems, as both the absorption value accuracy and the spatial resolution will be involved in the computation of the absolute absorption values. Thus, as the spatial resolution of the system used gives a large error due to the size of the bone, the need for better resolution precludes the need for more accurate absorption values, and defeats what may initially appear to be an advantage in the case of the bodyscanners.

Another important disadvantage of using the computed X-ray tomography systems is cost. Apart from the initial capital outlay for such a system, the running costs are so high that the scanner must be put to its best use at all times. The time required in fitting all the necessary brackets and in rearranging computer programs and output systems to convert a bodyscanner to a bone densitometer would be time and money wasted, and the clinical importance attached to bodyscanning in most hospitals would outweigh that given to the measurement of bone density. Thus, although bone densitometry is an important subject, it would not be allowed very much time on the average hospital bodyscanner.

A machine could be specifically designed, employing the latest Emiscan techniques, to obtain more accurate results than those possible with the present system. However, this would be extremely expensive, and such a machine would be limited to scanning limbs only.

From these arguments, it can be seen that the combined system of bone densitometer and ultrasonic tomogram for measuring bone density in vivo is still viable today due to its low dose rate, good spatial resolution, and low cost.

A detailed description of the X-ray bone densitometer may be found in Edwards (1973) and Al-Jarallah (1976), and will not be further expounded as no other improvements to this apparatus have been required.

CHAPTER 2
Tomogram Electronics

2.1 Introduction

The original suite of electronics for the ultrasonic tomogram was designed and built by Bashter (1976), and full details of these circuits can be found in his thesis. However, a short description of the concepts involved in the original system will be given below to set the present work in context. The improvements made to the tomogram electronics by Dr Archer-Hall in the year between the end of Bashter's work and the beginning of the present work will also be outlined to illustrate exactly the state of the electronics before the present author began, and the amount of reconstruction and improvement that has been achieved.

The rest of this chapter will present an extensive description of the present electronic design, including details of how well each circuit performed separately, and how well the completed suite acted.

2.1.1 Description of Original System

The original circuit design presented by Bashter (1976) had the same circuit elements as shown in Fig. 2.1, with the exception of the bias control system. The simplest way to describe broadly the initial system is to explain its method of operation and thus invoke the original design concepts of that system.

A 7MHz oscillator was used to create a pulse of 120 μ s duration, after which the oscillator was sharply cut off. The pulse was amplified through respective driver amplifiers and fed to the bone and reference transducers. The two received signals were to be isolated from any remaining drive signal or secondary reflections and preamplified in their respective isolator preamplifiers, which were identical in design. Each signal was then to be fed to an integrated circuit amplifier and a final amplifier before entering the discriminator. These two R.F.

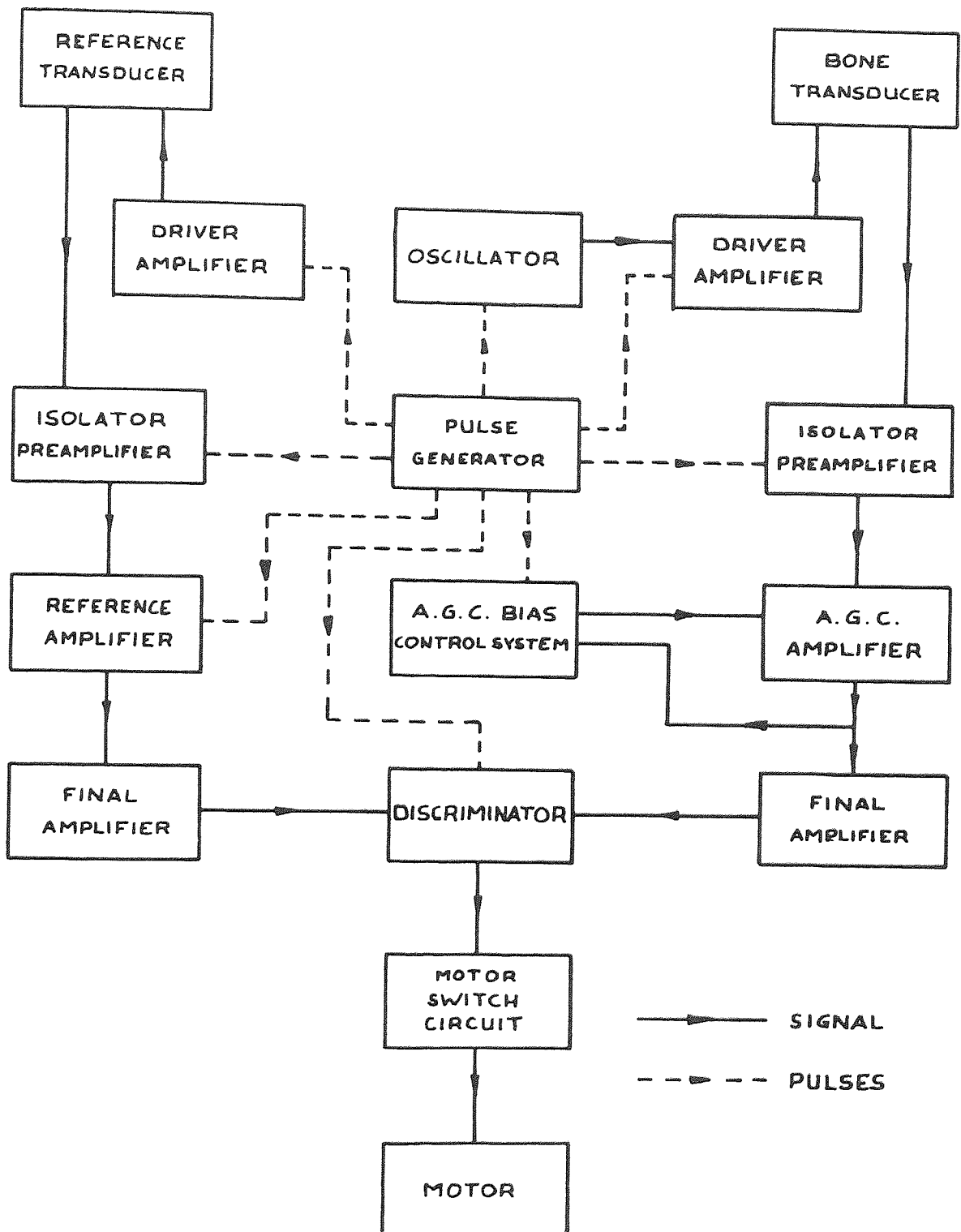


FIG.2.1 Block Diagram of Electronics

signals were then to be full-wave rectified to produce two d.c. levels. The d.c. component derived from the bone signal was to be fed back directly to the automatic gain control (A.G.C.) input of the bone main amplifier to provide the gain required to make the two d.c. levels in the discriminator of the same size. The discriminator would then compare the times of flight of each signal by the sharp cessation of the d.c. level, and provide a pulse to the motor switch circuit which would drive the bone transducer in or out to keep the bowl in focus on the surface of the ulna.

The first problem encountered with the original design concepts involved the shape of the wave-train. After extensive research by Bashter into backing and matching layers for the transducers, it was concluded that the abrupt cessation of the pilot wave could not be made sharp enough to enable accurate time-of-flight discrimination between the two received signals. Towards the end of Bashter's work it was thus decided to change the shape of the pulse to that shown in plate 2.1. Here the 7MHz pilot wave was made to fade almost exponentially to avoid "ringing" of the bowl transducer, and was followed by a sharp spike, or impulse, with which the relative times of the two reflections were compared.

The second problem was that the integrated circuit A.G.C. amplifier failed to have a wide enough range of gain to accommodate weak signals received from an obliquely deflected bone signal. Although two A.G.C. integrated circuits were tried in cascade, the result was still unsatisfactory, and further compounded by the poor bandwidth of both the A.G.C. and corresponding fixed gain integrated circuits. Work then began on the design of a new three stage A.G.C. amplifier incorporating discrete components, and a design using an FET on each of the first two stages

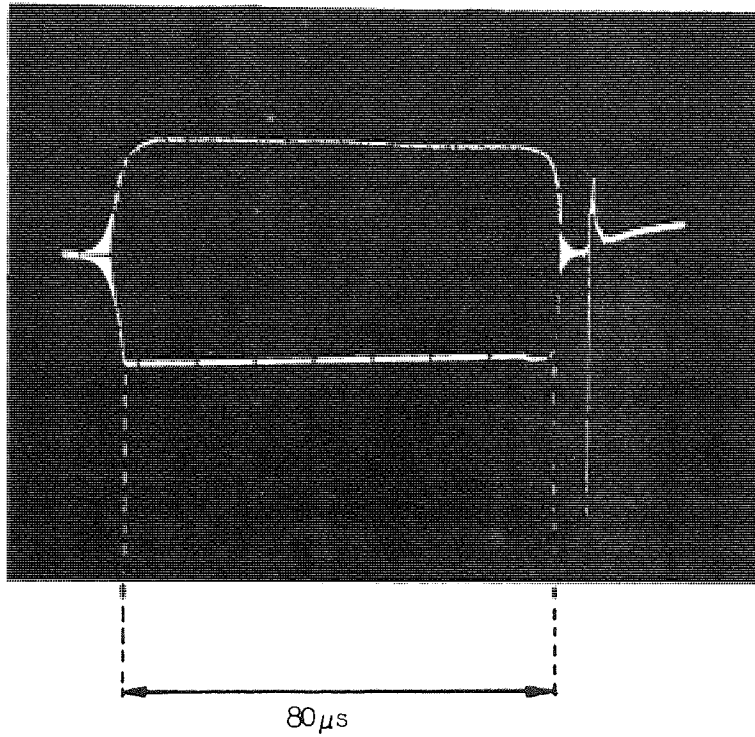


PLATE 2.1 Transmitted Wave Train

for attenuation was completed that had a wider gain range and bandwidth, although the former was still not quite wide enough. However, this improvement brought about the next difficulty.

It was found that the A.G.C. bias obtained from the discriminator rectifier was not stable enough, and was also interfering with the operation of the bone impulse within the discriminator circuit. This became apparent after Bashter had presented his thesis. Dr Archer-Hall began devising and constructing a bias control system which took its input from the primary of the discriminator rectifier, i.e. the collector load of the final amplifier. This operated through a diode pump system as described in Appendix 2, and was the one in operation when the present author began his research.

2.1.2 Objectives in Electronic Development

The circuit elements that required immediate attention in the beginning were the discriminator, the timing system and the bias system. The main problem with the discriminator was that it would not reset properly at the end of each period, and was prone to lock according to which was the later, or sometimes larger, impulse. The timing system was showing signs of drifting in some of the pretimed pulses. The bias system was unsatisfactory for two reasons; the maximum possible range of the A.G.C. amplifier was not considered great enough to allow for weak signals received from oblique angles of reflection, and also the complete system was found to oscillate at high gain, either due to the bias servo loop or the A.G.C. amplifier itself.

The initial aims of the project on the tomogram electronics were to remedy these three major faults. The discriminator reset was improved by replacing all the MOSFETs by transistors, and including a

feedback circuit to enable more positive cross lock.

The unreliability of the MOSFETs in the discriminator led to the removal and replacement of some in the pulse generator in an attempt to make the timing system more accurate. Eventually it was discovered that the drift in this system of multivibrators was due to the changing in value of the ceramic capacitors used. Once these had all been replaced by silver mica capacitors, the problem was solved.

The range of gain available from the original integrated circuit A.G.C. amplifier had already been proved to be totally inadequate. The new amplifier design using discrete components was an improvement, but still unsatisfactory. A further modification in this design was made by the author which achieved a tenfold increase in available gain.

Once the A.G.C. amplifier had been improved, considerable difficulty was experienced in dealing with instability of the complete system. It was eventually realised that this instability was liable to arise from two principle causes. The first of these is the closed loop involved in the A.G.C. system, and the second is unwanted feedback over the complete receiver amplifier chain. If the A.G.C. amplifier is operating at its maximum gain the overall voltage amplification is 1.6×10^6 .

The improvement in the performance of the A.G.C. amplifier required an improvement in the stability of the bias system controlling it, and several designs, along with their associated servo theory, were tried before the present one was found to work. The evolution of the present bias control system brought about another change in the basic concepts of the tomogram electronics. This was that it was unnecessary to transmit a pilot signal from the reference transducer, and hence the driver amplifier circuits need not be identical.

It was eventually realised that instability caused by feedback

through the complete system was due to the resonant response of the couplings between driver amplifier, transducer, and isolator preamplifier. This problem was solved by developing a more appropriate theory and circuit which displayed no resonance peak.

Of the complete list of circuit elements found in the block diagram of Fig. 2.1, only the motor and motor switch circuit have remained unchanged since the beginning of this project. As already shown, the discriminator, reference and A.G.C. amplifiers and the bias control system have all been completely redesigned. The timing of the pulse generator has been improved, some of the monostable circuits removed and others installed along with two auxiliary pulse modifiers, to suit the needs of the present system. The switching of the isolator preamplifiers has been improved, and the gains altered to suit the requirements of the new reference and A.G.C. amplifiers. The design and operation of the driver amplifiers has been modified, and a new theory of operation in their coupling to the transducers introduced (see Appendix 2). This has also involved some modification of the oscillator circuit. The bone and reference transducers and their backing layers have not been altered, although it was found necessary to encase them in new transducer housings. Thus it may be seen that the work on the ultrasonic tomogram has involved extensive reconstruction and improvement of the electronic system, the details of which will now follow.

2.2. General Description of Present Tomogram Electronics

The present suite of tomogram electronics is mounted, as before, in the revolving drum above the two transducers, and is fed from an external power pack through two copper slip rings on the top and bottom of the drum. The individual circuits are enclosed in aluminium boxes to

prevent radio frequency and static interference, and are connected with short coaxial leads. Leads carrying timing pulses do not need to be coaxial, as these carry relatively large voltage changes and are thus not as susceptible to interference. However, the timing pulse leads are colour coded to avoid confusion.

The block diagram (Fig. 2.1) illustrates the order in which circuit elements are connected and which require electronic gating by pretimed pulses. As can be seen from the diagram, the system is divided into two halves, the bone and reference sides, and the heart of the system is the pulse generator. This final system may be broadly described in the same manner as the original system, by explaining its method of operation and thus invoking the present concepts involved in the electronic design.

2.2.1 Method of Operation

In this system, the oscillator only provides a pilot wave for the bone transducer, as the reference transducer will always receive the pilot wave at the same amplitude. As the bone pilot wave is to be compared with that of the reference, then it is simpler to compare the former against a constant d.c. potential after it has been rectified rather than to amplify and rectify the latter.

Thus the oscillator only feeds the bone side driver amplifier, which adds the impulse onto the end of the faded pilot wave and transmits the complete wave train, while the reference driver amplifier takes an identical impulse and transmits it through the reference transducer. These signals are reflected by a stainless steel rod in the case of the reference side, and from the ulna on the bone side.

The signals received from the transducers are gated through the isolators, which attenuate transmitted signals in order to prevent them

causing oscillations in the following amplifier chains. Once separated from the larger drive signals, the received signals are amplified in the preamplifiers and main amplifiers, The amplified bone pilot signal is then used, through the bias control system, to set the gain of the A.G.C. amplifier to a level which will make the following bone impulse the same size as the reference impulse. Thus the whole system accommodates for received bone signals of varying amplitude.

The two signals are then amplified in identical final amplifiers before being compared in the discriminator. This circuit is designed to lock such that the motor is driven one way or the other, through the motor switch circuit, according to which impulse arrives first. The discriminator is also able to give no signal if the two impulses arrive simultaneously, and hence the motor is not driven. It will be seen, therefore, that the apparatus constitutes a three state servomechanism, whereby the bowl focus is maintained on the surface of the bone throughout the scanning period.

A three state servomechanism is inherently more stable than a two state. In the two state system, the motor will be forced to run all the time, either backwards or forwards.

2.3 Descriptions of Circuits

More detailed descriptions and diagrams of each circuit are now dealt with. The individual testing and performance of each circuit will be included, along with any additional data. In all the following circuit diagrams, the values of capacitance, inductance and resistance are given in Farads, Henries and Ohms respectively.

2.3.1 Pulse Generator

The following figures illustrate the pulse generator (Fig. 2.2)

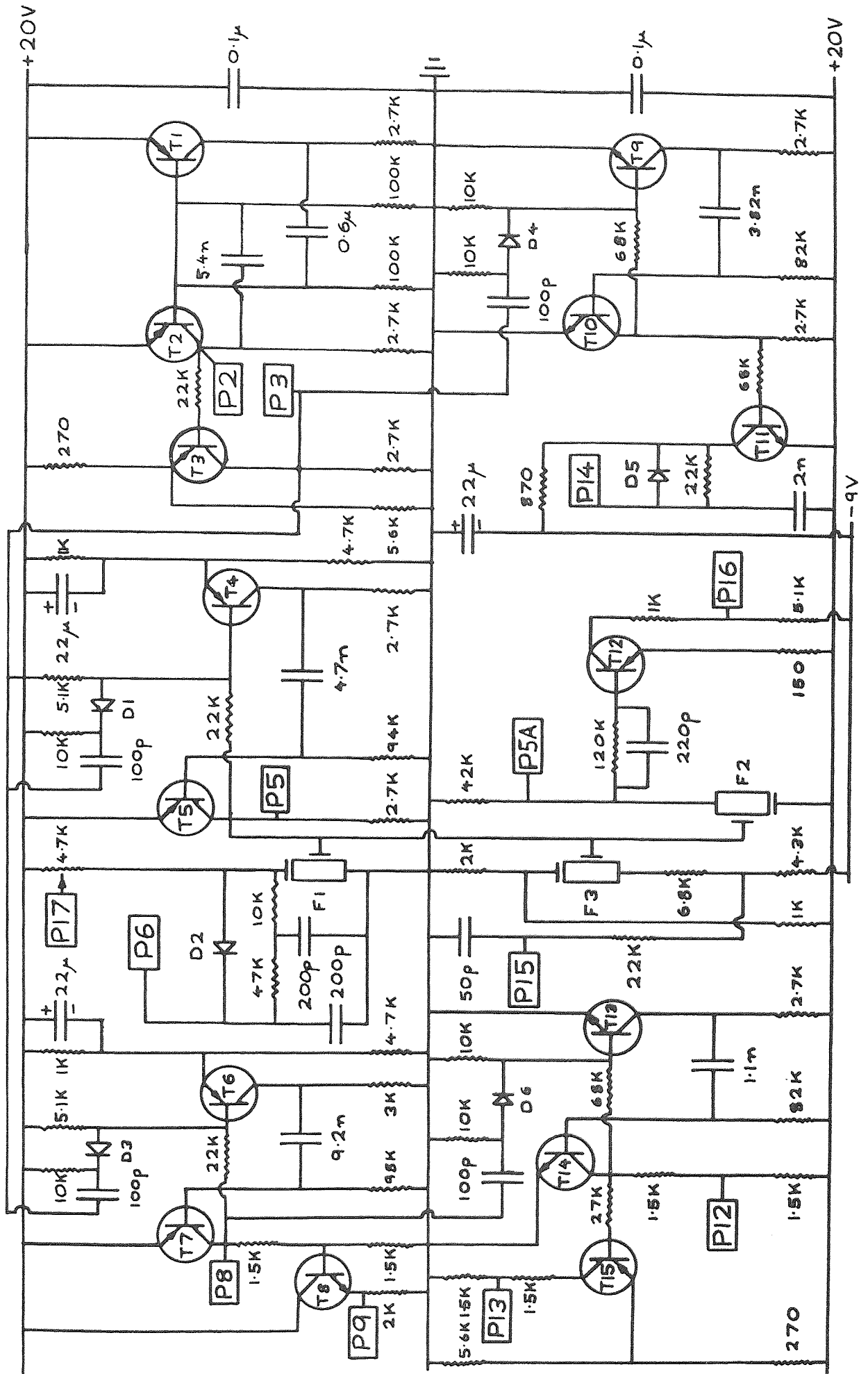


FIG.2.2 Pulse Generator

Components of Pulse Generator

Transistors

T1,T2,T11,T12 = V 723

T3,T15 = BCY 71

T4,T5,T6,T7 = BFX 48

T8 = EC 109

T9,T10,T13,T14 = BC 184L

FETs

F1,F2,F3 = 3N 155A, P channel MOSFET

Diodes

D1,D3,D4,D6 = Silicon Bead

D2 = 1N 918, Silicon

D5 = 1GP 10, Germanium

and a table of pulse shapes provided by the pulse generator (Fig. 2.3) which includes the actions of the pulses in gating the elements of the electronic system.

The transistors T1 and T2 form an astable multivibrator with a repeat time of 2 ms. The output P2 is buffer-amplified and inverted by T3 to drive three monostable multivibrators; (T4 and T5; T6 and T7; T9 and T10). The outputs of these are suitably processed to provide pulses P6, P9, P14, P15, P16 and P17 of the required voltage levels and sense. The output of the second monostable, T6 and T7, is also used to drive a fourth monostable multivibrator, T13 and T14, to provide pulses P12 and P13 after suitable processing and inverting.

Initial work on the pulse generator was with the purpose of improving the reliability and timing accuracy of that previously built by Bashter. It was considered that the main cause of failure in several of the circuits was due to the MOSFETs in the original design (Bashter, 1976) breaking down, even when they were being run well below their safe working voltages. The breakdown is believed to be due to the fast rise-time of the pulses being applied. Thus most of these MOSFET circuits were replaced by more reliable transistor circuits, the only remaining MOSFETs having relatively substantial source and drain resistors to protect them. This move greatly improved the reliability of the circuit.

The timing accuracy was improved when it was discovered that most of the times given by the monostables were liable to drift when the pulse generator had been working for some minutes, although the repeat time remained constant. Upon examination of the circuitry, it was found that all of the timing capacitors in the monostable multivibrators were made of ceramic, whereas the larger valued astable capacitor

PULSE	SHAPE		ACTION
	0 μ s	120 140 240 250 270 μ s	
P2	+20V +2V		ASTABLE TIMER
P3	+18V 0V		MONOSTABLE DRIVER
P5	+20V +2V		MONOSTABLE DRIVER OSCILLOSCOPE TRIGGER
P5A	+19V 0V		OUTPUT TO PULSE MODIFIER
P5B	+20V +10V		OSCILLATOR ATTENUATOR
P6	+18V +7V		DRIVER BIAS CHOPPER
P8	+20V +2V		MONOSTABLE DRIVER
P9	+8.8V +0.2V		OUTPUT TO PULSE MODIFIER BIAS OSCILLATOR CHOPPER
P9A	+9.5V 0V		DISCRIMINATOR RESET
P10	+19V +9.5V		DISCRIMINATOR RESET
P12	+20V +10V		DISCRIMINATOR GUARD
P13	+10V 0V		DISCRIMINATOR GUARD
P14	0V -9V		ISOLATOR GATE REFERENCE AMPLIFIER ATTENUATOR
P15	-1V -9V		DRIVER AMPLIFIER GUARD
P16	+14V -9V		DRIVE CHOPPER
P17	+20V +10V		ISOLATOR GATE

FIG.2.3 Pulse Shapes

(0.6 μF) was of paper construction. This led to the suspicion that the heat produced by the transistors in the enclosed box was causing the values of the ceramic capacitors to drift. This was confirmed when a test ceramic capacitor was heated with a soldering iron, and the timing of the circuit into which it had been clipped was altered by as much as 50%. A similar experiment on silver mica capacitors showed a drift of less than 10% after continual heating, in which the outer layer of the capacitor was almost destroyed.

Thus all the ceramic capacitors involved with timing were replaced by ones made of silver mica. No drift in timing accuracy was found even when the circuit had been left on for several hours.

Values of some of the components in the pulse generator have been altered during the work done by the author to suit new requirements due to further developments in other electronic elements of the system. The circuitry in Fig. 2.2 is the latest in this long line of minor modifications, and has performed satisfactorily since the two major improvements already mentioned.

2.3.2 Pulse P9 Modifier

The original pulse generator inverted pulse P9 within the pulse generator box, and provided two outputs, P9 and P10, of opposite sense, both acting at 240 μs , to reset the discriminator.

However, it was found that the operation of other pulses at 240 μs caused stray signals to enter the discriminator, so it became necessary to delay the reset pulses. The additional circuit (Fig. 2.4) is external to the pulse generator box, and delays the pulse P9 by 10 μs , giving pulse P9A as well as the mirror image pulse P10. This auxiliary pulse circuit has worked perfectly since its inception and has not

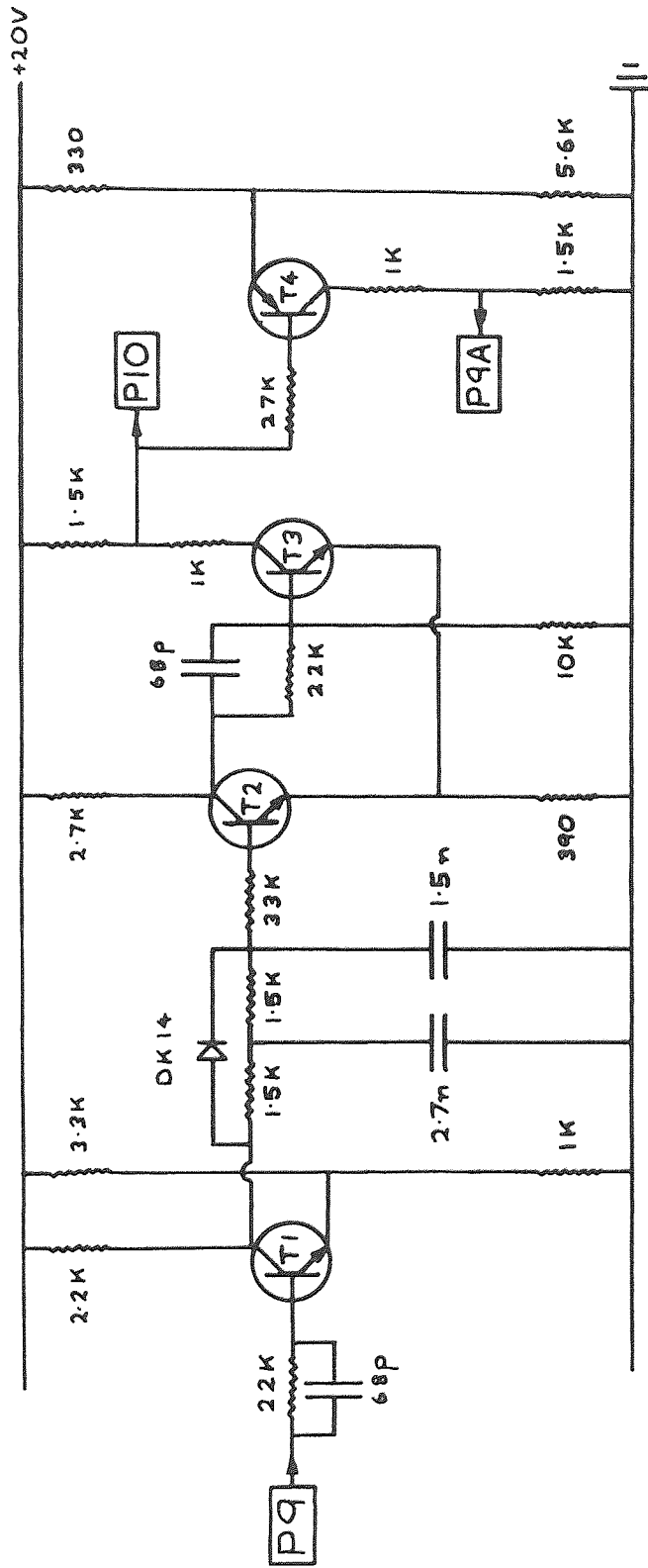


Fig 2.4 Pulse P9 Modifier

T1, T2, T3 = BC 109

T4 = BFX 48

required any more modifications.

2.3.3 Pulse P5A Modifier and Oscillator

Pulse P5A is further modified by an accessory monostable multi-vibrator (T1 and T2 in Fig. 2.5) to provide P5B, which is adjustable both in amplitude and pulse length. P5B is then used to effect the almost exponential decline of the pilot wave as already shown in Plate 2.1. This pulse is applied to the base of T4 in the oscillator circuit (Fig. 2.6) which inverts the pulse and feeds F1, a P channel MOSFET. When this conducts, the transformer is by-passed, and thus the positive feedback to T5 is effectively disconnected, hence stopping the oscillator.

This auxiliary circuit had been designed and built in the time between the end of the work by Bashter and the beginning of that by the author, and has undergone some minor modifications since then, resulting in the circuit shown (Fig. 2.5). The circuit is in a separate box to those in the pulse generator, as it was considered desirable to be able to adjust the pulse length and height when the machine was completely reassembled. This was so that the time between the end of the pilot wave and the impulse could then have its effect monitored experimentally by observing the output of the discriminator. Also, external adjustment between the radio frequency amplitude and the impulse height was desired to set the operating conditions of the bias control system.

The oscillator itself (Fig. 2.6) is a simple tuned radio frequency L-C circuit, suitably pulsed and amplified to provide a sine wave output of about 0.5V peak to peak and a frequency adjustable around the range of 6.85 MHz. The oscillator was originally designed so that the frequency could be adjusted in situ to give similar responses from both

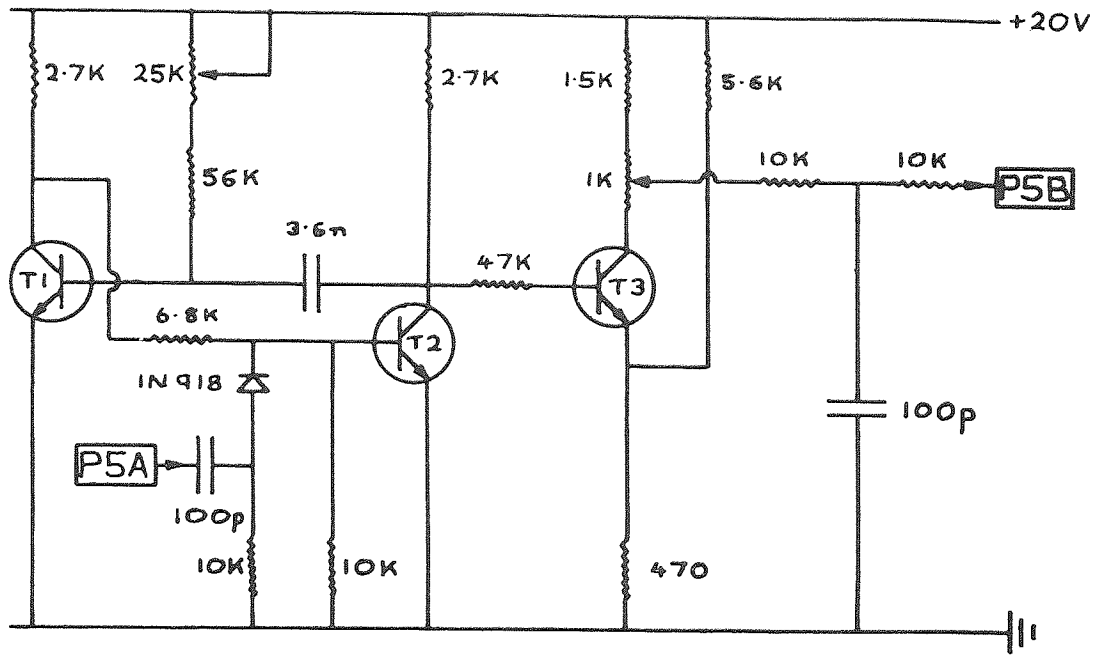


FIG.2.5 Pulse P5A Modifier

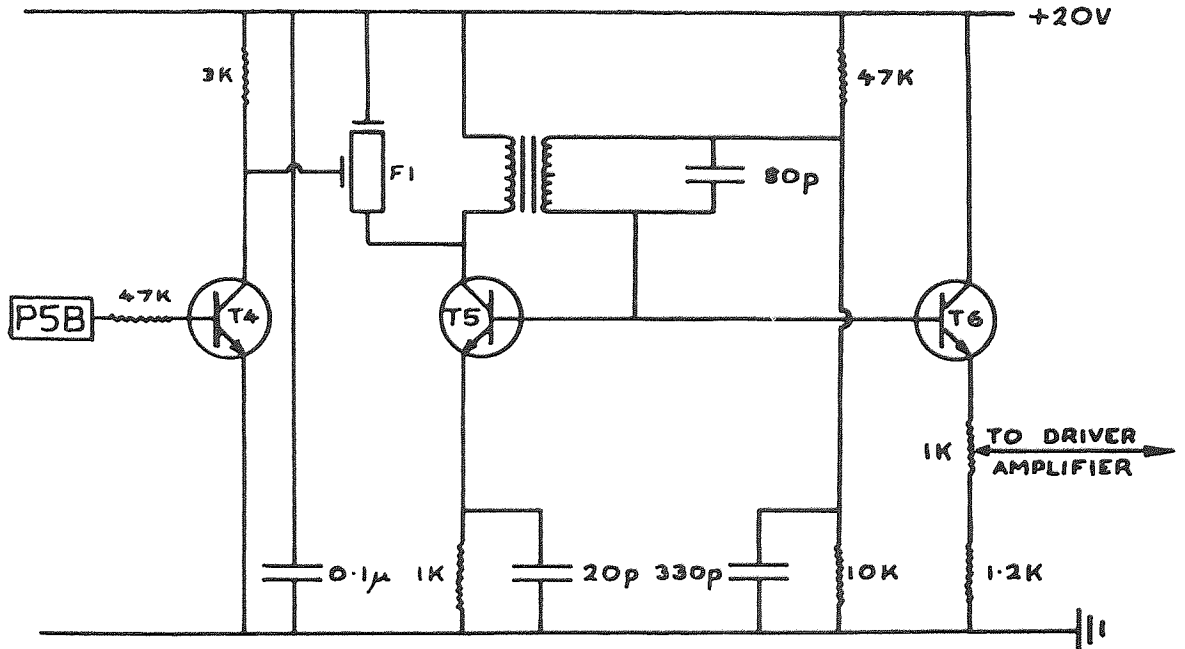


FIG.2.6 Oscillator

T1,T2,T5 = BC 184L
 T3,T4,T6 = BSX 39

the bone and reference transducers that it fed (Bashter, 1976). This was because the transducers, their housings and backing layers, would combine to give slightly different resonant frequencies, and a balance would have to be sought to keep the size of each signal identical. When it was decided during the present work to feed only the bone transducer with a pilot signal, this frequency was readjusted to give an optimum resonance. The circuit has not been modified since then and has worked without failure.

2.3.4 Bone Side Driver Amplifier

This circuit is illustrated in Fig. 2.7. The output from the oscillator is further attenuated by P5B acting on T1 and F1, causing T1 to conduct, and F1 to cut off, thus diverting the signal to + 20V, which is an effective a.c. ground.

The sausage-shaped pilot wave is then amplified through T2. This driver amplifier is then cut off through the operation of P6 and P15. By making T3 conduct, P6 raises the bias on T4, thus cutting it off. P15 causes F3 to conduct at the same time, which is just after 120 μ s. At 120 μ s, P16 causes F2 to conduct vigorously, and an impulse resulting from the preset capacitor and D2 is fed into the base of T4. The capacitor is adjusted to match the size of the impulse on this side to that on the reference side.

D3 has been selected to give a low voltage drop with d.c. flowing, but to present a very large resistance to small voltages. As the voltages derived from the echo signal do not exceed 100 mV, D3 is cut off while the transducer is receiving. Detailed theoretical considerations of the couplings between the driver amplifier, transducer and preamplifier are given in Appendix 2.

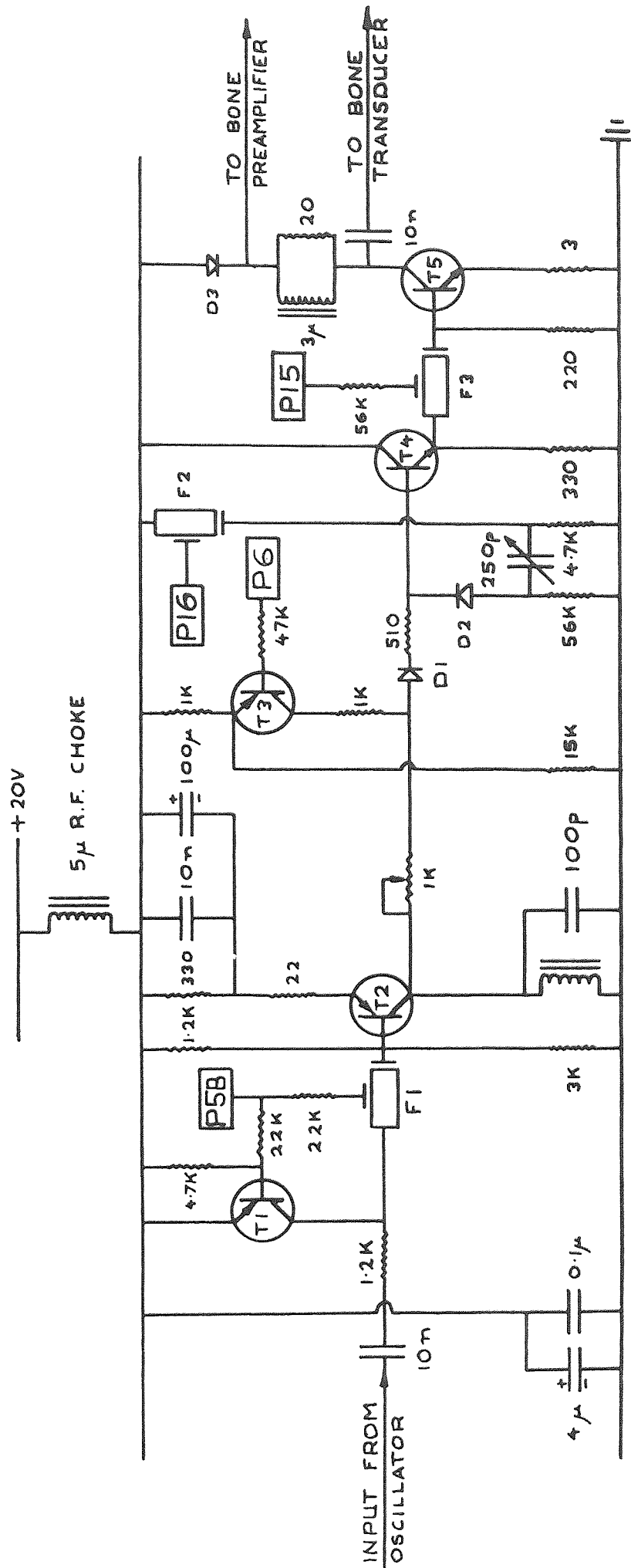


Fig 2.7 Bone Side Driver Amplifier
 T1 = 2N 4062 T4 = 2N 2219
 T2 = 2N 2905 T5 = GED 44C3, Power Transistor D2 = 1GP 10, Germanium
 T3 = BFX 48 P1, F2, F3 = 2N 4859 N Channel JFET D3 = 4 x OA47, Germanium

This circuit, as far as F2, has only undergone minor modifications from the original Bashter design, such as the replacement of an unreliable P channel MOSFET by the transistor T3, and the adjustment of the associated resistor circuitry. However, the signal fed to T4 in Fig. 2.7 was originally split and fed to two identical amplifier stages similar to that shown in the figure, the outputs supplying each transducer with identical signals. As this has been found unnecessary for the reasons already stated, the present circuit feeds only the bone transducer, and a separate circuit has been built to supply the reference transducer with its impulses.

The other great improvement in this circuit in comparison with the Bashter design is in the coupling to the driver amplifier, transducer and preamplifier. A $20\ \Omega$ resistor has been added in parallel with the $3\ \mu\text{H}$ inductance and an $80\ \text{pF}$ capacitor originally in parallel with D3 has been removed. This coupling provides a satisfactory signal with a bandwidth as shown in Fig. A.3.3 in Appendix 3. It is considered that the liability to oscillation of the bone side amplifier system was accentuated by the presence of the peak at $8.5\ \text{MHz}$ in the original system.

When the present circuit was devised and the theory of its operation developed, it was found that a small resistance would give a relatively flat response above $5\ \text{MHz}$, with no peak or maximum to promote oscillation. When the circuit was built and installed, it was found that the behaviour of the complete system was less prone to oscillation, thus allowing the bias control system to work properly by sampling only signal voltages, and not oscillatory artefacts.

2.3.5 Reference Driver Amplifier

This circuit (Fig. 2.8) is a copy of the last part of the bone side

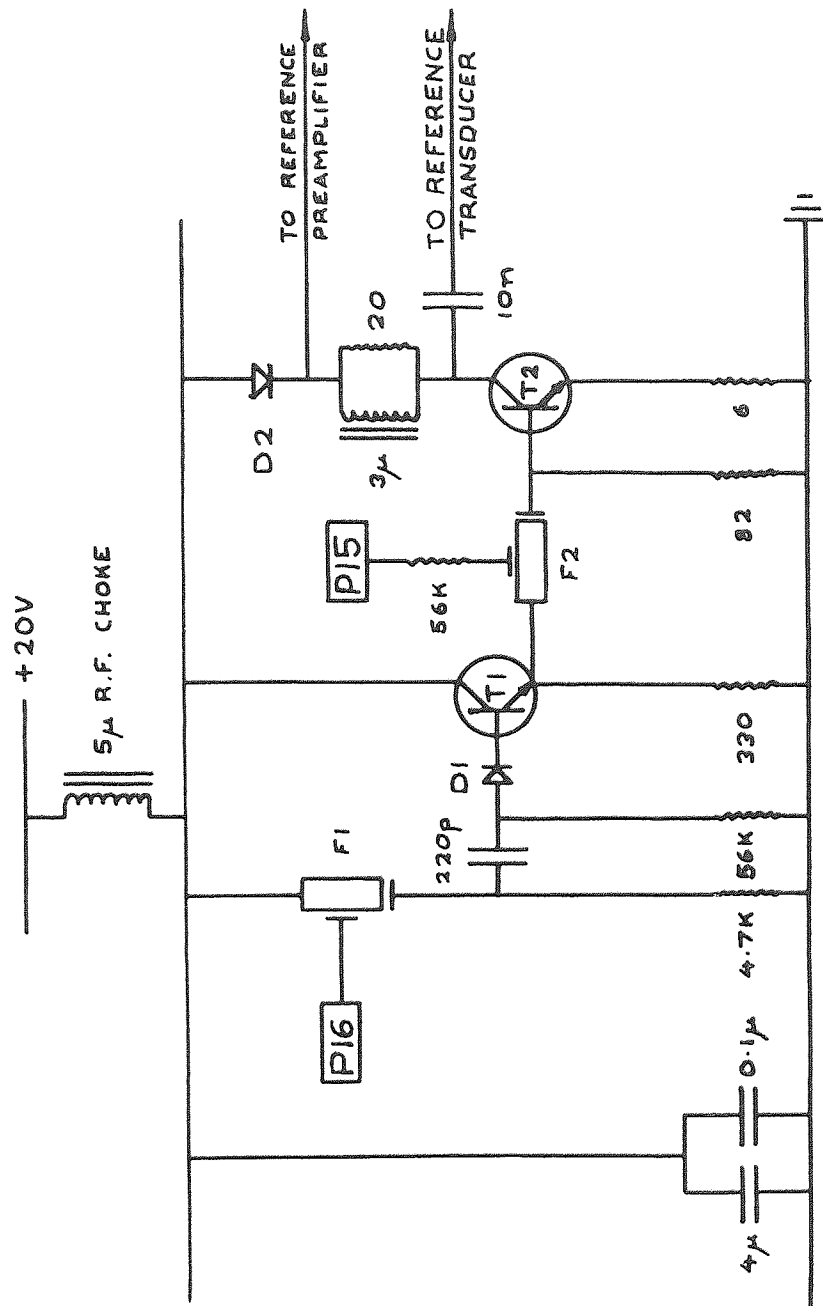


Fig 2.8 Reference Driver Amplifier

T1 = 2N 2219

D1 = 1GP 10, Germanium

T2 = GED 44C3, Power Transistor

D2 = 2 x DK 14, Germanium

driver amplifier, with the exception that the 220pF capacitor is of a fixed value. The impulse caused by the operation of P16 is thus processed in the same manner as that for the bone side, and transmitted to the reference transducer. Both the reference and bone side driver amplifiers have worked consistently since they were installed, although much care has to be taken when operating them without a transducer load, in that they must be switched off and any charges allowed time to leak to earth before re-connecting the transducer. This must be done to avoid any unnecessary damage to the transducers.

2.3.6 Isolator Preamplifiers

These are shown in Figs. 2.9 and 2.10. Here P14 and P17 are used to isolate the received signals from any residual transmitted signal by use of F1, T1, F2 and F3. The reference preamplifier has a lower gain than the bone preamplifier, because its signal is derived from a wave which is always normally reflected from a hard stainless steel surface, while the wave on the bone side will be liable to undergo oblique reflection and attenuation from its passage through tissue. F4 provides further pulsed attenuation of 8:1 on the bone side as the difference between the received and transmitted signals will be greater.

T2 and T3 provide the actual amplification, in a cascade configuration also used in later amplifier stages. Here T2 is the collector load of T3, thus reducing the Miller effect of transistor self-capacitance which can be a source of loss of signal at high frequencies.

The response of both isolator preamplifiers is flat to within 3dB from 2MHz to 14MHz. The gain of the bone side isolator preamplifier is 18 and the reference side 6.

When the present work began, both preamplifiers were identical. However, it was soon realised that the gain of the reference

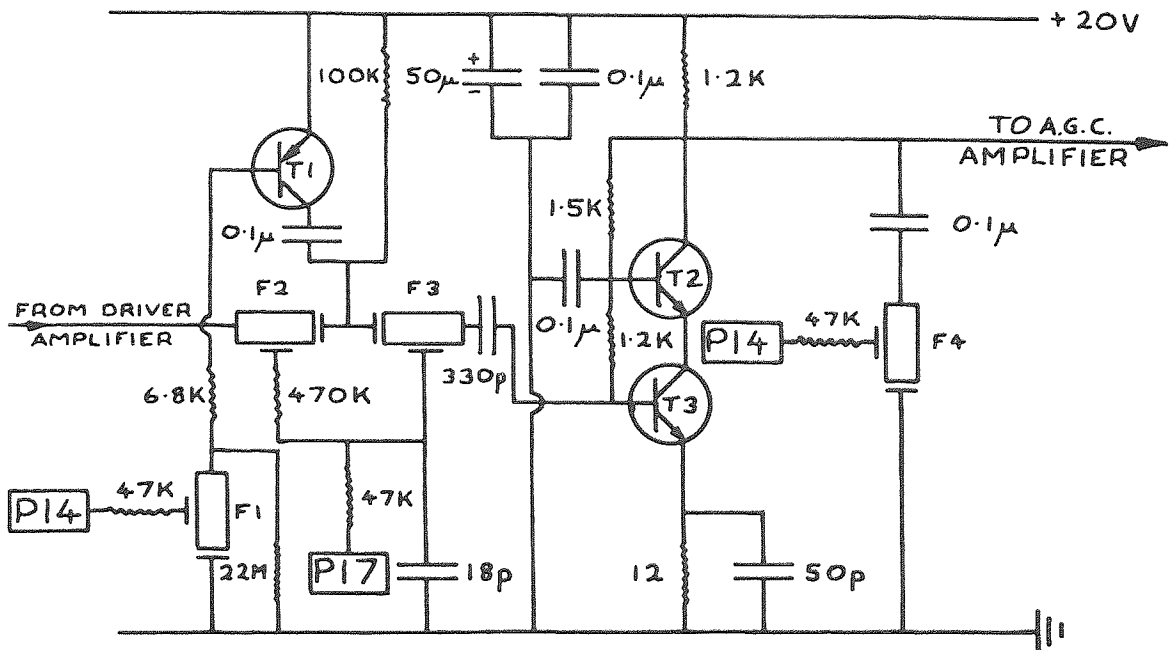


FIG.2.9 Bone Side Isolation Preamplifier

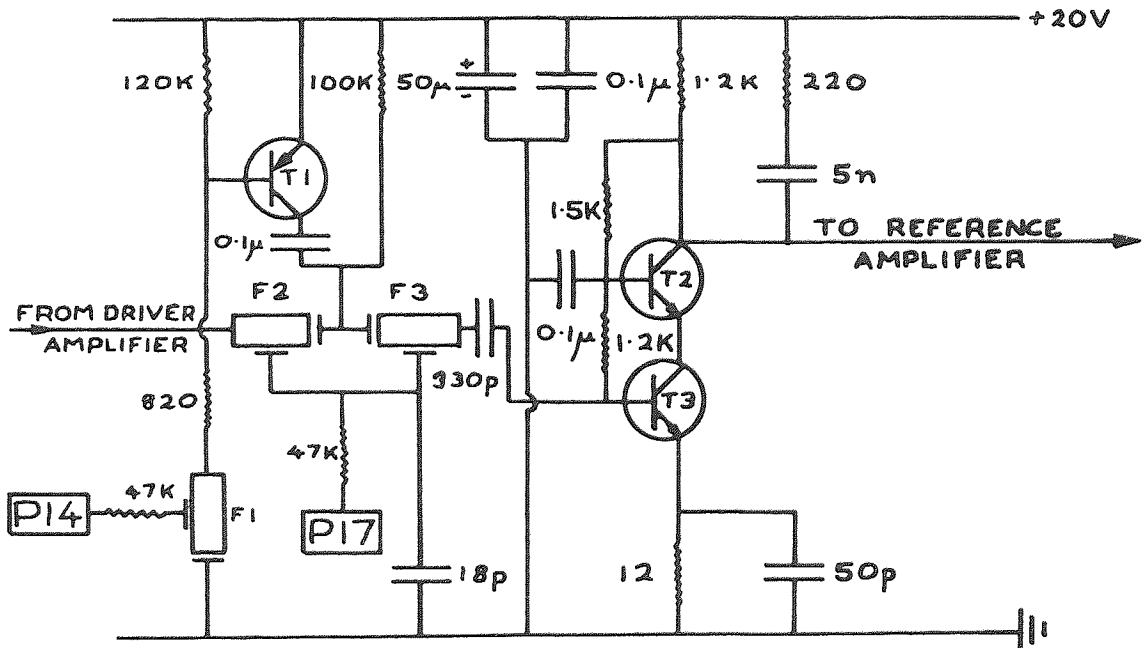


FIG.2.10 Reference Isolator Preamplifier

T1 = 2N 2905
 T2, T3 = BC 109
 F1, F2, F3, F4 = 2N 4859, N channel JFET

preamplifier could be reduced, as the received bone signal would never be as large as one from a stainless steel rod. Experiments on the change in gain from a bone as opposed to a rod showed that the gain on the reference side could be reduced by at least a half. It was eventually reduced to a third by the inclusion of a 5nF capacitor and a 220 Ω resistor to leak away some of the amplified signal.

As the size of the received signal on the bone side is much smaller, the difference between this and any residual transmitted signal will be less, and hence a greater degree of isolation will be required on the bone side. This further attenuation was achieved by the pulsed signal leak system of F4.

2.3.7 Bone Side A.G.C. Amplifier

The A.G.C. amplifier, Fig. 2.11, is a three stage system comprising three individual cascade amplifiers; T1 and T2; T4 and T5; T8 and T9; linked by three emitter followers; T3, T7 and T10. The gain is voltage controlled in the first stage, and current controlled in the second.

The bases of T1 and T8 are held at steady d.c. levels by the zener diodes D1 and D2, as it was found that the simple potentiometers first devised were insufficient. This was not necessary or desirable on the second stage, as the operation of the bias and signal leak transistor T6 would be affected by maintaining a steady d.c. on the base of T4.

In the first stage, the signal can be attenuated by F1 due to a signal V_F . Attenuation in the second stage due to I_T is effected through T6, which is made to conduct and leak away both a.c. signal and d.c. bias. V_F and I_T have been arranged to vary in proportion, so a reading of V_F is sufficient to monitor the gain control.

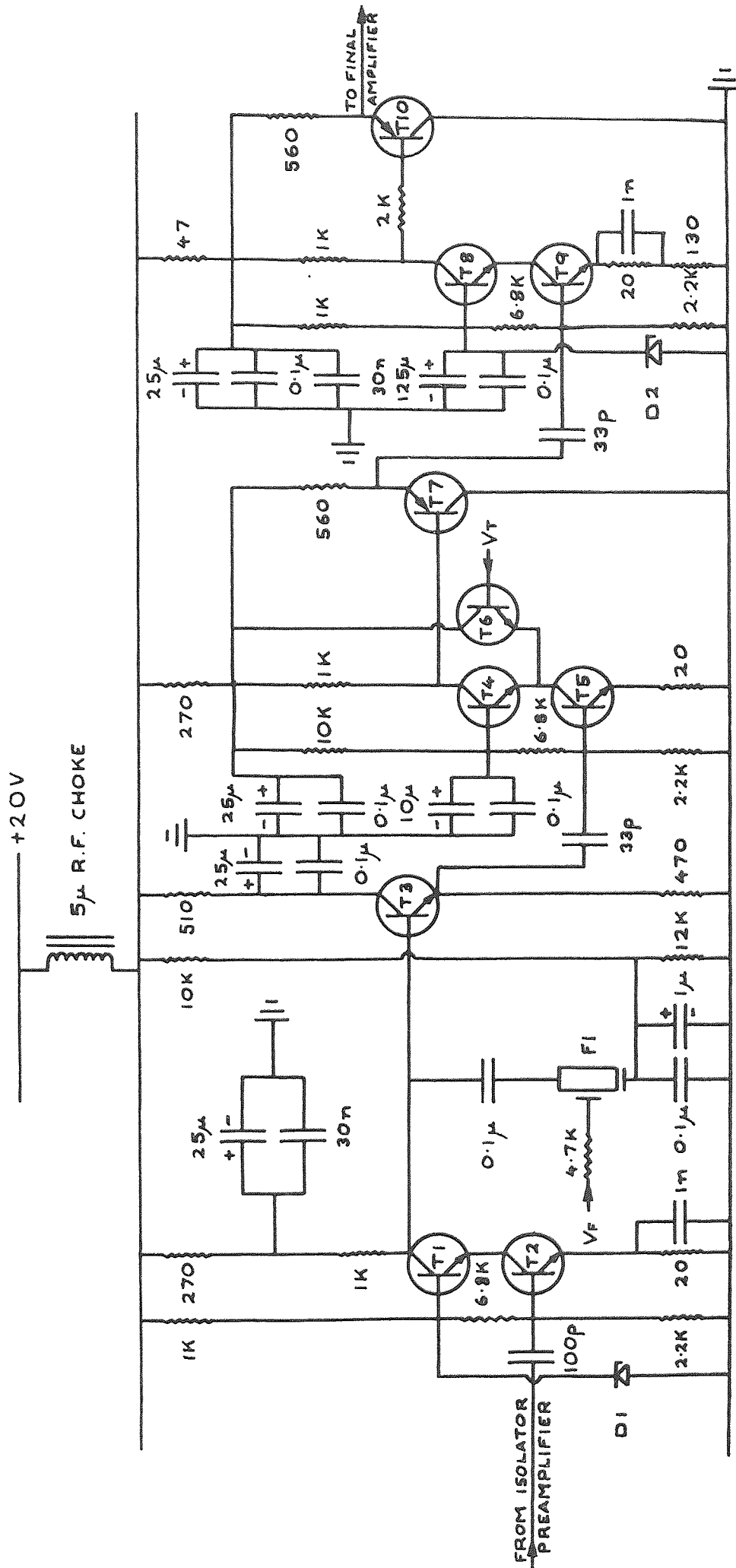


Fig 2.11 A.G.C. Amplifier

- T1, T4, T8, T9 = 2N 2219
- T2, T3, T6 = BC 109
- T5 = BC 108B
- T7 = 2N 2905
- F1 = 2N 4859, N Channel JFET
- D1 = BZY 88C, 2.7V Zener
- D2 = BZY 88C, 6.2V Zener

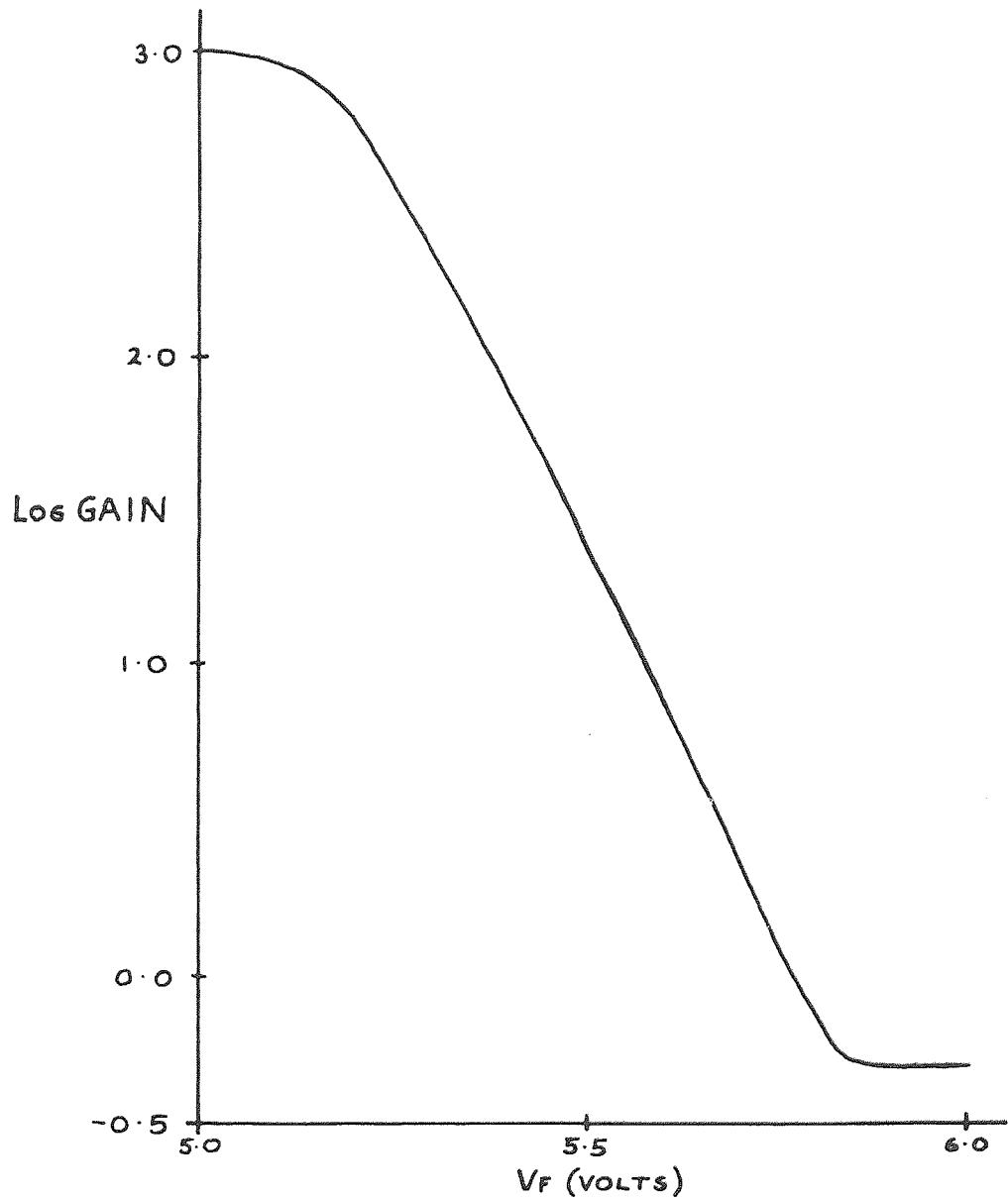


FIG.2.12 Graph of V_F vs log GAIN for
A.G.C. Amplifier

Fig. 2.12 is a graph of V_F against log gain, and shows that the gain varies almost exponentially with V_F . A change in V_F of 1 volt can effect a change in gain of about 2000 times. The response of the amplifier is flat to within 3dB from 5MHz to 12MHz.

The design of this three stage amplifier was started by Dr Archer-Hall and completed during the present project, as it was found that the range of gain attainable from the integrated circuit A.G.C. amplifier in the original electronics was insufficient, and its bandwidth was too narrow. Initially, it was proposed to attenuate both first and second stages of amplification by JFETs. This had just been completed when the author began, and it was found that this method did not provide sufficient attenuation.

The idea of using transistors to leak away both a.c. signal and d.c. bias was realised and tried on both stages. However, this provided too much gain range, and was very unstable, becoming oscillatory even for small amounts of gain. The compromise circuit shown in Fig. 2.11 was then tried, and found to work very well. At this stage, both FET and transistor were being fed from the same A.G.C. voltage acquired from the initial bias system (see Appendix 2). Only when the bias control system had been sufficiently improved was it found necessary to improve further the operation of the A.G.C. amplifier by arranging to feed the attenuating transistor T6 with a current derived from the voltage fed to F1, to make the operation of the transistor more linear. The grounded-base constant current circuit designed to supply T6 is given in section 2.3.10 of this chapter.

2.3.8 Reference Amplifier

This is shown in Fig. 2.13, and is a cascade amplifier (T1 and T2)

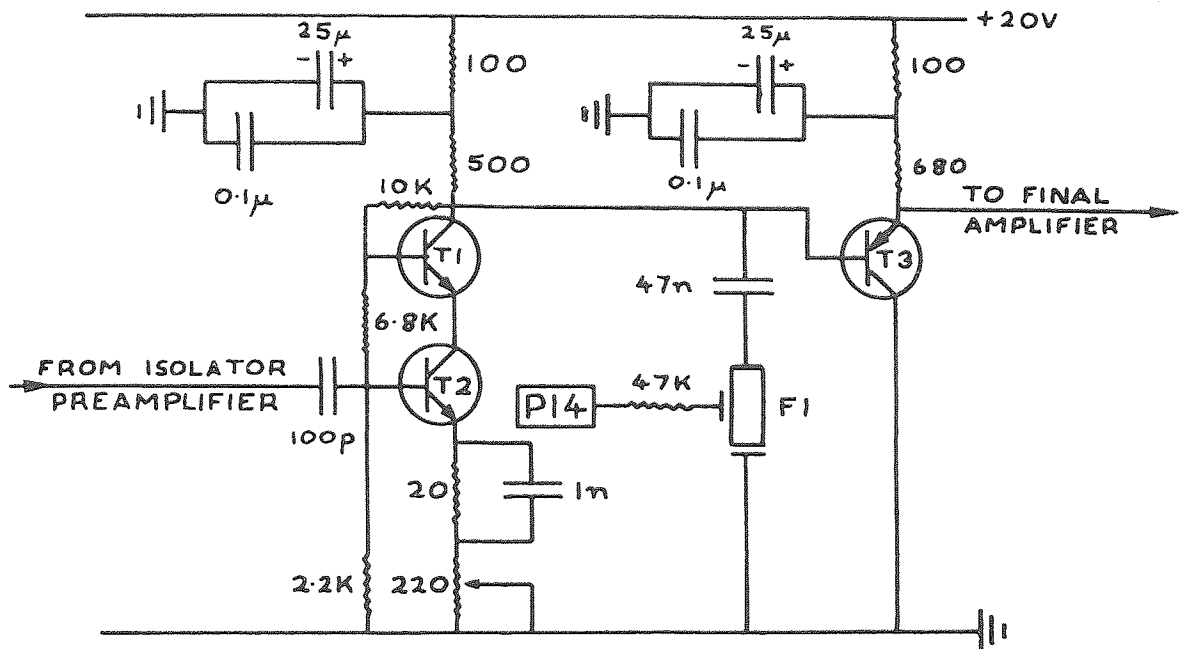


FIG. 2.13 Reference Amplifier

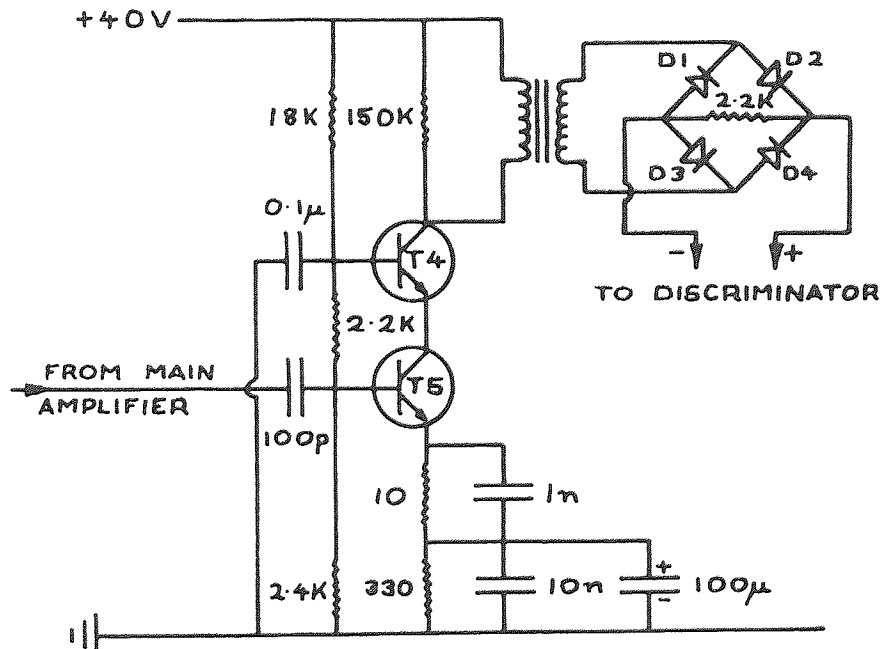


FIG. 2.14 Final Amplifiers

- T1, T2, T4, T5 = 2N 2219
- T3 = 2N 2905
- F1 = 2N 4859, N channel JFET
- D1, D2, D3, D4 = 1N 918, Silicon

with an adjustable gain via the 220Ω potentiometer, which alters the feedback fraction. The gain attained can be altered between 0.4 and 4, even when the complete system is assembled. The output is matched to the following stage by an emitter follower, T3. The amplifier has a bandwidth of 13MHz, its response being flat between 1MHz and 14MHz.

Work on the design and building of this amplifier was started by Dr Archer-Hall and finished by the author. The amplifier replaced the integrated circuit reference amplifier of the original Bashter design. This was done to ensure that the reference signal would pass through an almost equivalent main amplifier to that on the bone side, and hence any time delays or distortions of the impulse would be similar on both sides.

2.3.9 Final Amplifiers

This is shown in Fig. 2.14, and is another cascade amplifier of a fixed gain of 40. The collector load of T4 is a transformer, the output of which is full wave rectified to provide a potential difference which is fed to the discriminator. The final amplifiers of the bone and reference sides are identical, the main amplifier referred to in the circuit diagram being either the reference or A.G.C. amplifier.

The gain of this amplifier is measured in d.c. out for half peak R.F. signal in. The amplifier has a bandwidth of 12MHz, being flat between 2MHz and 14MHz, these frequencies being measured at the input and compared to a 3dB drop in d.c. output.

2.3.10 Bias Control System

Fig. 2.15 illustrates the bias control system of the A.G.C. amplifier. Here, the output of the A.G.C. amplifier is further

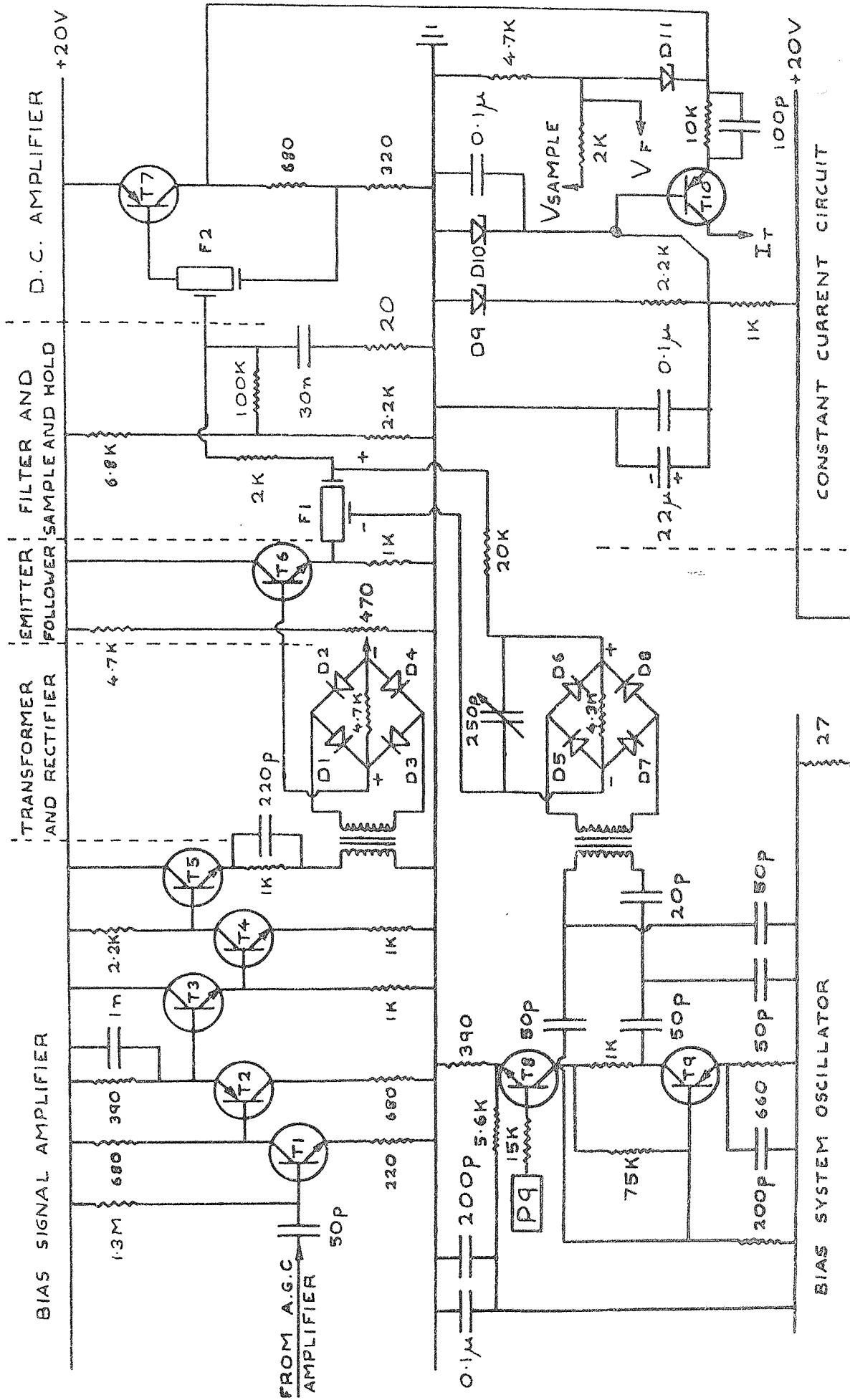


FIG.2.15 Bias Control System

Components of Bias Control System

Transistors

T1,T3,T4,T6,T8 = BC 109

T2,T10 = BFX 48

T5 = 2N 2219

T7,T9 = 2N 2905

FETs

F1 = 2N 4859, N channel JFET

F2 = 2N 3821, N channel JFET

Diodes

D1,D2,D3,D4 = OA 91, Germanium

D5,D6,D7,D8 = OA 90, Germanium

D9 = BZY 88C, 13.5V zener

D10 = BZY 88C, 4.7V zener

D11 = BZY 88C, 8.2 V zener

amplified about 40 times in the direct coupled bias signal amplifier, which has a bandwidth of 9MHz, between 3MHz and 12MHz. The amplified signal is full wave rectified and the resulting output is then separated from preceding stages by an emitter follower, T6, acting as a buffer amplifier.

The output of the emitter follower is fed through the hold FET, F1, to the d.c. amplifier, which has a gain of 2.8 and also adds 2.6 volts. The potentiometer network on the 30nF capacitor provides a passive lift system, which causes the final voltage V_F to rise slowly after the gain of the A.G.C. amplifier has been set. This allows the received impulse to pass through this amplifier, but tends to lower the gain afterwards. This was found necessary to attenuate further any secondary echoes received by the bone transducer, which may have found their way into the discriminator. The lift system also prevents the A.G.C. amplifier from staying at a possible high gain for the rest of the 2 ms period, thereby reducing the risk of oscillation.

The switching of the hold system is governed by the pulse P9, which is used to make T8 conduct and provide power for the bias system oscillator. This is a Gouriet oscillator, working at 25MHz, the output of which is full wave rectified to provide an earth-free potential, which is then used to switch F1 and hence provide the hold.

The 30nF hold capacitor also acts as a filter on the full wave rectified bias signal, so that the output from the d.c. amplifier is a slowly changing d.c. level in the region of 13 to 14 volts. This output is fed to the grounded-base amplifier, T10, which provides I_T at a constant voltage. The zener diode D11 subtracts 8.2 volts from the output of the d.c. amplifier to provide V_F . The monitoring of the bias voltage is taken through 2K Ω to avoid any accidental shorting, and is



referred to in the circuit diagram as V_{SAMPLE} .

The original circuitry by Bashter (1976) had no bias control system whatsoever. By the time the author began his work, the initial bias control system built by Dr Archer-Hall had been included (see Appendix 2). Several improvements were made to this initial system before it was eventually discarded. The first problem of this system was that the sampling point was on the primary of the final amplifier, which tended to interfere with the operation of the discriminator. This was avoided by building two bias signal amplifiers. A sample and hold system similar to that in the present bias system was the next modification.

Eventually, however, it was realised that the diode pump system of obtaining two d.c. levels to compare the sizes of each signal would be prone to instability even when working perfectly, and was discarded. The reasons for this are given in full detail in the following chapter and in Appendix 2, but they were basically that the servosystem was both third order and involved a long time constant, and thus would be unstable in nearly every circumstance.

It was at this stage that two of the basic concepts of the ultrasonic tomogram were changed. It was realised that there was no need to transmit a pilot wave in the reference signal, as this would always return with the same magnitude, and once rectified would just be a constant d.c. level. Thus it was arranged that the rectified bone pilot wave could be more easily compared directly with an adjustable d.c. level within the bias system, and so the reference pilot wave was discarded. This carried the further advantage that the oscillator could then be tuned to obtain a maximum resonance with the bone transducer, and hence avoid the need for such a great deal of amplification.

From the servomechanism theory shown in Chapter 3, it became obvious that a short time constant for the bias acquisition would be necessary so the method of altering the bias by small increments was superseded by a technique in which a new value of bias is quickly obtained for each received wave train, and then discarded before the next signal appears.

Although testing of each circuit within the bias system may prove satisfactory, it is the performance of the complete system that must be ascertained. This was achieved by feeding the bias system with an R.F. signal modulated by a square wave, and examining the rise time of the bias obtained when no hold is being used. The signal was derived from a four diode, low capacitance bridge rectifier, suitably loaded and fed from an untuned R.F. transformer. For a 7MHz R.F. signal, this gave a rise time of about $0.2\mu\text{s}$, i.e. about $1\frac{1}{2}$ cycles of the R.F. signal. This was believed to be the bias acquisition time for the complete system, and indicated that the bias control system was working in agreement with the theory.

2.3.11 Discriminator

The potentials from the rectifying bridges of the two final amplifiers are connected as shown in Fig. 2.16. T1 and T5 are guard transistors, which only conduct between $240\mu\text{s}$ and $270\mu\text{s}$. T2 and T6 are shorting transistors, which only conduct between 0 and $250\mu\text{s}$. Thus the discriminator line A is set at 10 volts until $250\mu\text{s}$.

Assuming an impulse to arrive from the bone side first, then the line B will become positive with respect to line A, causing T1, D9, T3 and T4 to conduct, and the collector of T3 will rise to twenty volts. This causes D10 to conduct, reinforcing the base current to T3. At

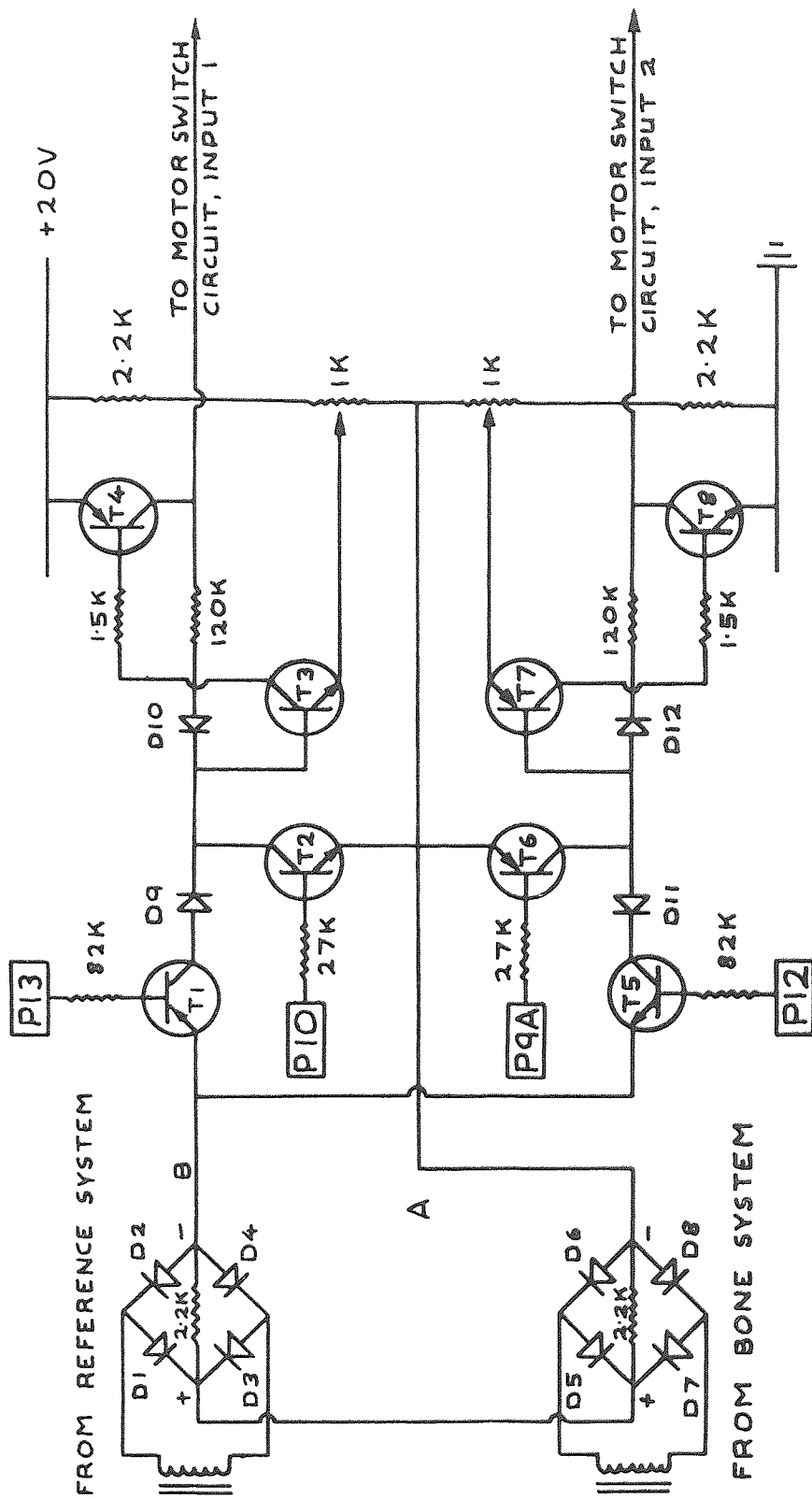


Fig 2.16 The Discriminator

T1, T5, T7 = BFX 48

D9, D11 = DK 14, Germanium

T2, T6 = BC 109

D10, D12 = Silicon Bead

T3 = BC 107

D1 - D8 = IN 918, Silicon

the same time, the collector potential of T3 rises, causing line A to follow, which makes T6 conduct and prevents any signal arriving on the reference side from altering the lock.

There is a threshold of about two volts on the discriminator inputs, and any stray signal less than this will not operate it. This threshold can be adjusted on each side by operating the $1K\Omega$ potentiometers, which have been arranged to be in such a position as to be accessible when the complete system is assembled except for the motor switch circuit, which does not have to be present to check the in-house performance of the discriminator.

Hence a signal arriving first from the bone side final amplifier will cause the discriminator to lock upwards, at the same time ignoring any signal following on from the reference side, until T2 and T6 are reset at $0\mu s$. This dual bistable circuit will thus lock in one direction for an impulse first from the opposing final amplifier, in the other direction for an impulse first from the other final amplifier, and will do nothing if both impulses arrive at the same time, provided they are of the same magnitude to within $\pm 20\%$.

By the time the author began his project, the principle of operation of this circuit was well established, and a very similar circuit had been built. However, this initial circuit was found to operate inconsistently and unreliably. The reliability of the circuit was improved by replacing the four MOSFETs by the transistors T1, T3, T5 and T7, and exchanging the two BC 109 transistors used as diodes (by connecting base and collector together) by the Germanium DK 14 diodes D9 and D11. These modifications made the discriminator less prone to breakdown, but did not improve its consistency in reacting to impulses. This was achieved by including the two $120K\Omega$ resistors and

diodes D10 and D12, which were not in the original design. This positive feedback line greatly improved both the effectiveness of the lock and the cross lock. These improvements then allowed the discriminator to measure up to its expected operating conditions, namely to react to an impulse with a rise time of less than $0.1\mu\text{s}$, and to disregard any following impulses from the opposite system, however large they may be.

The discriminator has been tested in three ways. The first experiment was to feed one side with a 500Hz square wave and to examine the rise time of the line A, which is fitted with a monitor lead. The rise time was found to be a fraction of a microsecond for either side. During this experiment both sensitivity potentiometers were adjusted to give the same threshold on each side. The second test involved the construction of a manual keying circuit which gave a spike from a charged capacitor to whichever side was desired according to which of the two keys was depressed. This experiment proved that the discriminator would remain locked in one direction, even when a spike impulse of 20 volts was applied to the other input. The third test was carried out when the entire electronics were assembled. Impulses coming from real signals were observed to cause the discriminator to lock at a time after $250\mu\text{s}$, which proved that the reset pulses did not interfere with the operation of the circuit. The modifications and improvements to the original discriminator were made at the very beginning of the work by the author, and there has been no need to alter this circuit as it has performed satisfactorily since then.

2.3.12 Motor Switch Circuit

This converts the lock pulses from the discriminator to power surges applied to the armature windings of the motor, and is illustrated

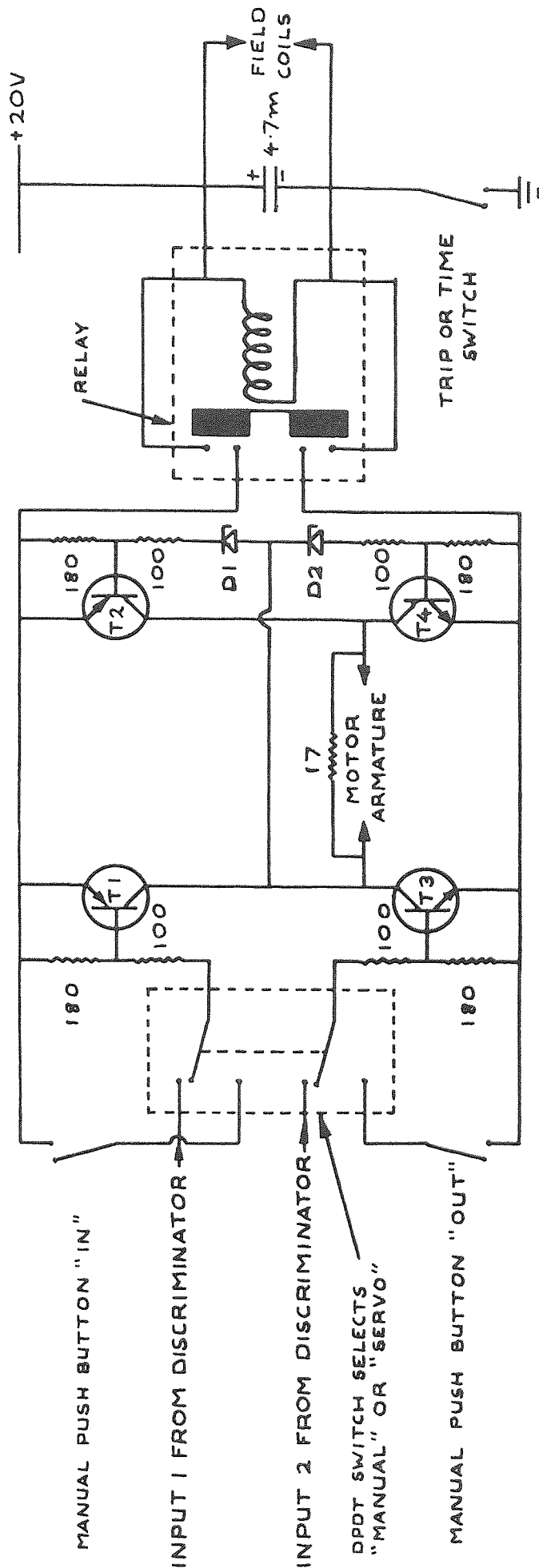


Fig 2.17 Motor Switch Circuit

T1, T2 = MJE 1290, Power Transistors

T3, T4 = MJE 1661, Power Transistors

D1, D2 = IS 501, 5A, 15V Zener

in Fig. 2.17. From the time of operation of the relay, the motor field coil current is constant, and of a large enough value so that a maximum torque is obtained when the twenty volts are applied to the brushes from the motor switch.

A 17Ω resistance has been incorporated into the initial design concepts to improve the mechanical servo stability of the motor. When the motor is switched off, the resistance across the brushes gives dynamic breaking by making the motor operate as a dynamo. It is considered that this is capable of bringing the motor to rest in less than $1/200$ th of a second, i.e. less than two repeat periods of the transmitted impulse. As the system is capable of detecting an error of about 0.1 m.m., which is about five repeat periods, it may be seen that the motor is arranged not to overshoot. This damping of the motor amounts to a servo lag of less than $1/10$ th of a degree, and will thus not affect the accuracy of the scan obtained.

Auxiliary switching is included to allow for a timed sweep of the ulna, and for positioning of the bone transducer to receive a good signal before a scan is taken.

This circuit is the only one in the entire electronics that has not required modification or improvement, the only work being done on it being to replace two of the power transistors that were inadvertently short circuited and burnt out. The circuit is included for completeness, and because the circuit given by Bashter did not illustrate the auxiliary switching.

2.3.13 The Motor

This was originally designed to operate as a 12 volt series motor. It was selected by reason of its small overall size and low moment of inertia of its rotor.

In the tomogram, it is operated as a 20 volt parallel motor, to provide as large a value of angular acceleration as possible. When run continuously, it could develop as much as 1/10 H.P., which would probably cause it to overheat within a minute. However, some cancelling of the signals within the discriminator when the bone transducer is in focus on the bone surface will help to avoid overheating, and the fact that no signal is applied to the motor for the first 250 μ s of the 2ms period, and that only a 275° scan is envisaged, which should take about 25 seconds. Again, this has only been included for completeness, as no further work or repair has been required in connection with the motor.

2.3.14 Transducer Housing

A new transducer housing has been designed, built and tested. It is illustrated in Plate 2.2 and Fig. 2.18. The previous housing was found to leak, and although several types of liquid sealant were tried, they proved to no avail. The housings were tested for water leakage before being connected to the electronics by being assembled and left underwater over a weekend, and then being dismantled and checked for any signs of leakage. None were found, and one of the new housings has been in use for over two years and has given no trouble due to water leakage during this time.

2.4 Conclusions

As can be seen from this chapter, the work involved on the electronics of the ultrasonic tomogram has been extensive, in that all except one of the fifteen circuits has been modified, some often several times. Many circuits have been completely redesigned, and some have been added.

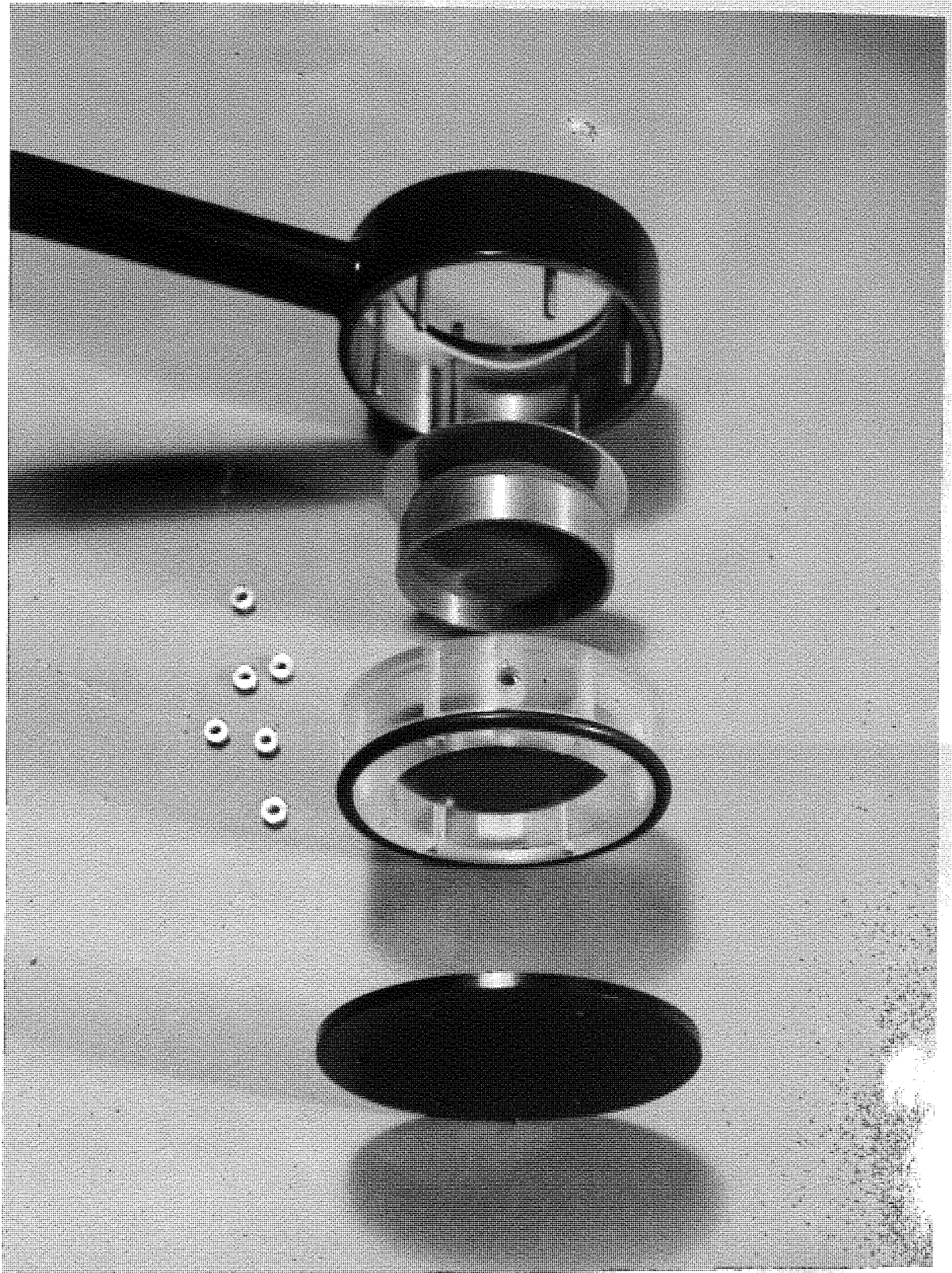
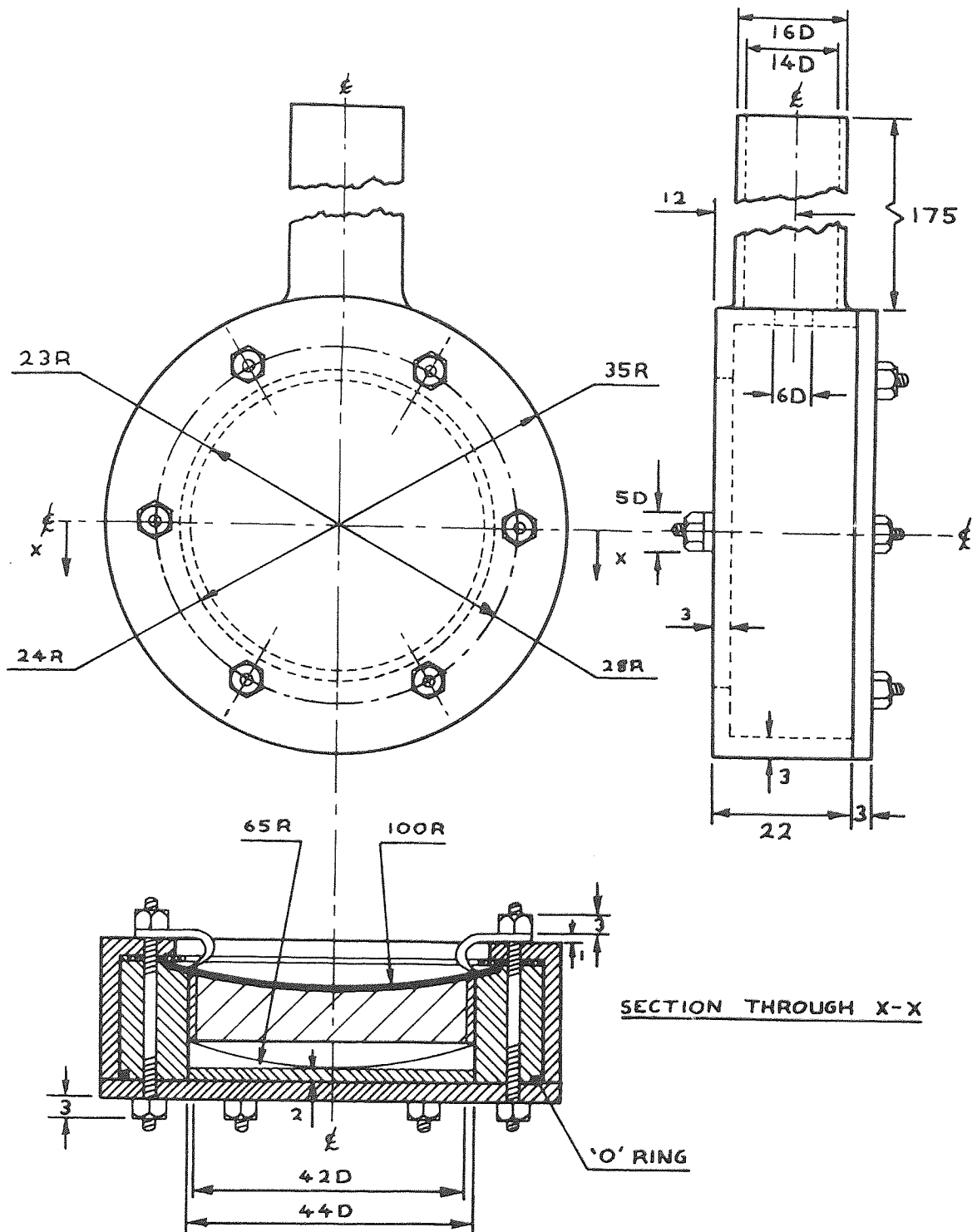


Plate 2.2. Transducer Housing



FIRST ANGLE PROJECTION	SCALE: FULL SIZE
ALL DIMENSIONS IN MILLIMETRES	
ALL NUTS AND STUDS - 6 B.A.	'O' RING - 3 WIDE, 670.0.
HATCHING: = BOWL TRANSDUCER	
= BRASS	= SILICONE RUBBER
= PERSPEX	= TUNGSTEN RUBBER

FIG.2.18 Transducer Housing

In practice, the tomogram has worked and traced several test pieces of cylindrical configuration, as well as following the outline of a flat object to an angle of oblique reflection of up to 40° without incurring any instability. However, no reproducible results could be obtained as the second transducer housing began to leak just before the end of the project, and the transducer was unfortunately cracked in being transferred to the new housing. The results obtained did show the complete system to work satisfactorily, and it is believed that little further work is needed on the electronics of the tomogram.

Further work, especially at this stage, could involve the development of a larger bowl transducer, or at least the replacement of the damaged one. The results already obtained on test pieces could then be confirmed. The next step would be to devise a procedure to set up the machine and to calibrate it against samples of an accurately known cross-section.

One area of work that has not been considered in the present project that would then need to be examined is the matter of the rubber cuff. The cuff used at the moment does not afford a very good water-tight seal around the arm, and tends to perish as it is made of rubber. The requirements of the rubber cuff are that it should form a watertight seal fitting comfortably around the arm, be adjustable to suit varying sizes of forearm, and be resistant to continuous exposure to sweat and water. Materials to be investigated for feasibility could include neoprene, nitriles, chloroprene or perhaps a silicone rubber.

Once this has been achieved, the tomogram would be ready for clinical trials. An experiment to measure the power of the ultrasonics being concentrated at the focus of the bowl would have to be performed to determine the dose of ultrasonics being given to a patient. Although cavitation has not been observed in water, and it is not believed that

the machine is powerful enough to cause cavitation, experimental evidence should be given before clinical trials can begin, as non-cavitation in water is not a reliable guide. Although recent work has not uncovered any great danger of ultrasonics to the human body (Wells, 1977, Fry, 1979), this research has usually been with planar transducers, and some consideration should be taken of any possibility of adverse effects due to bowl transducers.

CHAPTER 3

Bias Theory

3.1 Consideration of Time Constants

As has been shown from previous discussion, it is required that the reflected signals from the bone and reference sides be equal within limits of about 20% when presented to the discriminator in order to provide a three state servomechanical drive.

As the signal from the ulna may vary in amplitude by a factor of as much as 1000 times due to different angles of reflection and thicknesses of attenuating tissue, it is clear that a variable gain will be required. The system has been designed so that an appropriate gain shall be determined for each reflected bone pulse by means of a pilot wave transmitted immediately prior to the timing impulse. It is also necessary that the bias control voltage, V_B , should approach very closely to its equilibrium value, V_E , within the available time, which is $80\mu\text{s}$ (see Plate 2.1).

The establishment of a value, V_E , of a gain control bias, from the amplitude of the reflected pilot wave, of necessity involves a closed loop or feedback system. The analysis of the stability and response of this system requires consideration of the time constants in the loop. This bias control system produces a slowly changing voltage from the 7MHz R.F. signal. Once this voltage, V_E , has been attained, it is held until the beginning of the next cycle.

The order of the electrical servo loop system may in general be equal to the number of time constants which it incorporates (Westwater and Waddell, 1961). These may be considered as follows:

3.1.1 Bias Acquisition Time

This may be defined as the time taken to derive a signal (by rectification of the amplified R.F.) whose d.c. component is $(1 - 1/e)$

of its ultimate value. It is possible to estimate this time at as small a value as one half period of the R.F. for a full wave rectifier bridge feeding a high resistance, low capacitance load.

However, it is clearly desirable that the bias acquisition process should be able to follow both falls and rises of the R.F. amplitude equally rapidly, so the bridge must not have too high a resistive load.

It has been shown experimentally, by using a square wave modulated R.F. signal, that the bias acquisition time can be made about $1\frac{1}{2}$ cycles of the R.F. signal. This is with the use of a four diode, low capacitance bridge rectifier, suitably loaded, and fed from an untuned R.F. transformer. For a 7MHz signal, this gives a time constant τ of about $0.2\mu\text{s}$.

3.1.2 Filtration Time Constant

It is clearly necessary that there should be no ripple or R.F. component in the d.c. bias signal supplied to the A.G.C. amplifier. While ripple may be readily reduced by resistance capacitance filters, it has been seen only too easily that the time constants of such systems lead to unstable or oscillatory behaviour of the bias system.

3.1.3 Sample and Hold

If it is assumed that the loop system can attain a balance in the available time, it is necessary that the voltage it finds shall be used for gain bias when the impulse (or distance measuring echo) arrives. This can only be achieved by the use of a storage capacitor connected to the input terminals of a high impedance amplifier (Millman and Halkias, 1972). The capacitor must be capable of being charged rapidly from the bias acquisition system, and isolated by electronic

switching from that system just before the cessation of the pilot wave (R.F. signal). It is also necessary that the "instruction" to hold should not produce a disturbance of the bias voltage, so the hold capacitor needs to be large enough to absorb any possible disturbance produced by the electronic switching.

3.1.4 Actuation Time

This may be considered in relation to the rate of change of gain of the A.G.C. amplifier with change in bias signal, V_B .

3.1.5 Amplifier Response Times and Phase Shifts

Time effects under the last two headings have been kept to values which have been considered negligible by constructing amplifiers in the bias system using direct coupled, high frequency transistors with low values of load resistors. This may be illustrated by the bandwidth of the bias signal amplifier, which is about 9MHz wide, being flat to within 3dB from 3MHz to 12MHz.

Thus it would seem that the time constants under the headings 3.1.4 and 3.1.5 can be neglected at least in comparison with that under 3.1.1. A previous bias system operated with these three major time delays, and was found too unstable as it was a third order system (see Appendix 2).

The instability of this servosystem has been a major problem in the development of the tomogram, and has only been resolved by complementary practical and theoretical approaches used at each stage. Only the initial and final stages are discussed in this thesis.

A second order system is stable under certain conditions. Consideration of these led to the development of the present system, in which

the time delays due to filtration and hold are combined. It was also realised that only by a transformer feeding the diodes could an increment on the inevitable acquisition time be avoided.

The combination of the acquisition and filtration times to produce a second order system was considered, but this would only result in either serious loss of signal or very poor filtration. Thus the two remaining time delays need to be distinctly separated by an emitter follower acting as an impedance matching device. The final system is symbolically shown below in Fig. 3.1.

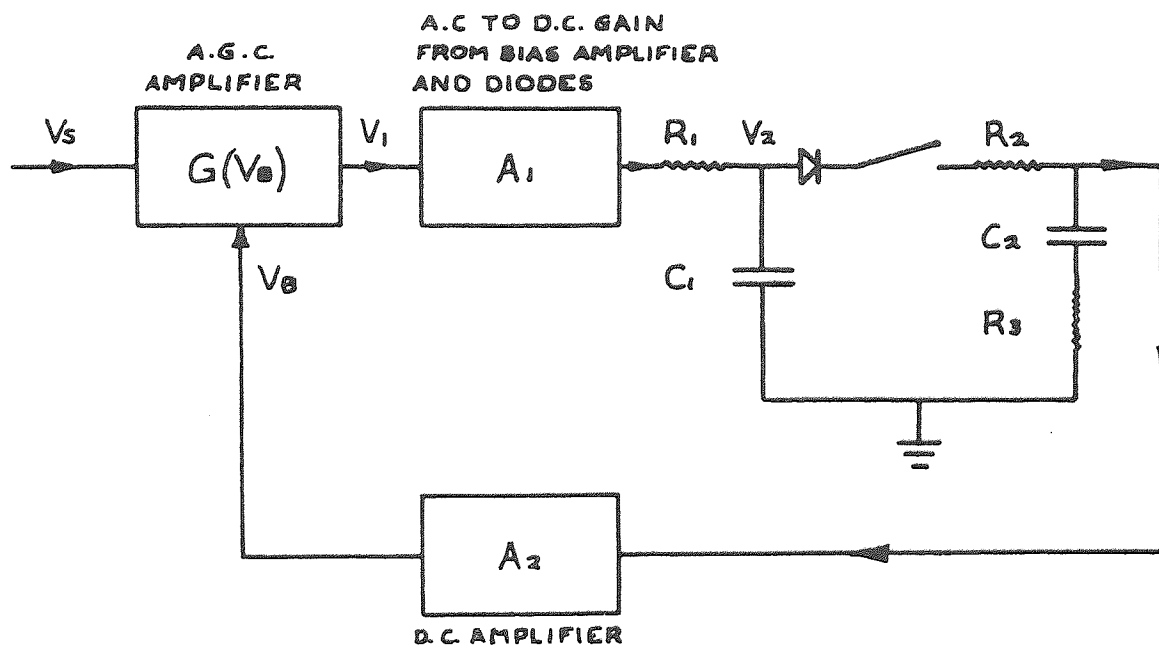


Fig. 3.1 Bias System

3.2 Bias Theory

Now, from Fig. 3.1,

$$V_r = V_s G(V_B), \text{ where } V_s = \text{modulus of R.F. signal voltage.}$$

$$V_2 = \frac{A_1 V_1}{1 + R_1 C_1 D},$$

$$V_B = \left[\frac{1 + R_3 C_2 D}{1 + (R_2 + R_3) C_2 D} \right] A_2 V_2,$$

where $R_1 C_1$ represents the acquisition time of the diode system, and thus are virtual components. R_2 , R_3 and C_2 represent real components by contrast.

Combining,

$$V_B = \left[\frac{1 + R_3 C_2 D}{1 + (R_2 + R_3) C_2 D} \right] \left[\frac{A V_S G(V_B)}{1 + R_1 C_1 D} \right] \quad (3.1)$$

where $A = A_1 A_2$.

If we now let $R_1 C_1 = \tau$,

$$R_2 C_2 = m\tau,$$

$$R_3 C_2 = p\tau,$$

then, rearranging equation (3.1),

$$(1 + \tau D) \{1 + (m + p)\tau D\} V_B = (1 + p\tau D) A V_S G(V_B) \quad (3.2)$$

If $p = 1$, the system is first order and therefore non-oscillatory for any function G . However, consideration must be given to the general requirements for stability.

In the amplifier constructed, a change of V_B from 5V to 6V changes the gain G from about 1000 to about $\frac{1}{2}$. This enables the signal V_S to have a value from 50mV to 60mV, which satisfies the signal requirement of a variation of only 20%. Thus signals at the transducer can range in strength from about 3mV to as little as a few microvolts as the preamplifier gain is 20. Analysis of the stability of the system is facilitated by putting $V_B = x + V_E$.

This gives:

$$(1 + \tau D)\{1 + (m + p)\tau D\}x = (1 + p\tau D)AV_S G(x + V_E) \quad (3.3)$$

For x small, by Maclaurin's theorem,

$$G(x + V_E) = G(V_E) + xG'(V_E) + \frac{x^2}{2!} G''(V_E) + \dots$$

Now, from equilibrium conditions

$$V_E = AV_S G(V_E) \quad (3.4)$$

$$\begin{aligned} \therefore & [(1 + \tau D)\{1 + (m + p)\tau D\}x] + V_E \\ = & [(1 + p\tau D)AV_S][G(V_E) + xG'(V_E) + \frac{x^2}{2!} G''(V_E)\dots] \end{aligned} \quad (3.5)$$

By subtracting (3.4) from (3.5), and neglecting terms in x^2 and higher, as stability is only to be considered for small disturbances for x , this gives:

$$(1 + \tau D)\{1 + (m + p)\tau D\}x = (1 + p\tau D)AV_S xG'(V_E)$$

For a particular value of V_S , and hence V_E , there will be a gain G^* (from (3.4)), and the product $V_S G^*$ will thus be a constant of magnitude $\frac{V_E}{A}$.

Therefore,

$$(1 + \tau D)\{1 + (m + p)\tau D\}x = AV_S G^* \frac{\partial G(V_E)}{\partial x} (1 + p\tau D)x \quad (3.6)$$

The right hand side of equation (3.6) may be written as $-H(1 + p\tau D)x$ for any one value of V_E .

$$\therefore (1 + \tau D)\{1 + (m + p)\tau D\}x = -H(1 + p\tau D)x \quad (3.7)$$

Rearranging:

$$[(m + p)\tau^2 D^2 + \{1 + m + p(1 + H)\}\tau D + (1 + H)]x = 0 \quad (3.8)$$

And hence

$$\left[D^2 + \left\{ \frac{1 + m + p(1 + H)}{(m + p)\tau} \right\} D + \left\{ \frac{1 + H}{(m + p)\tau^2} \right\} \right] x = 0 \quad (3.9)$$

This is to be compared with the standard equation of damped harmonic motion:

$$(D^2 + 2kD + \omega_0^2)x = 0 \quad (3.10)$$

$$\therefore k = \frac{1 + m + p(1 + H)}{2\tau(m + p)} \quad (3.11)$$

and

$$\omega_0 = \left(\frac{1 + H}{(m + p)\tau^2} \right)^{\frac{1}{2}} \quad (3.12)$$

H is a measure of the slope of the function G, and it is when this has its largest value that instability is most likely to occur.

The servosystem is to be operated in a slightly overdamped state, so the analysis will deal with a general solution for overdamping where $k = n\omega_0$, taking account of the special case where $n = 1$.

The general solution for overdamping is:

$$x = Ae^{(-k + \sqrt{k^2 - \omega_0^2})t} + Be^{(-k - \sqrt{k^2 - \omega_0^2})t} \quad (3.13)$$

In practice, the first term is the only one to be considered, as this decays more slowly with time. Expanding this term gives:

$$\begin{aligned} x &= Ae^{\{-k + k(1 - \omega_0^2/k^2)^{\frac{1}{2}}\}t} \\ &= Ae^{\{-k + k(1 - \omega_0^2/2k^2)\}t} \\ &= Ae^{-(\omega_0^2/2k)t} \end{aligned}$$

This has to be less than 1% of A in the available time of 80 μ s. e^{-5} is less than .01.

$$\therefore Ae^{-(\omega_0^2/2k)t} < Ae^{-5}$$

$$\therefore \frac{\omega_0^2 t}{2k} < 5$$

Substituting from (3.11) and (3.12), putting $k = n\omega_0$, and taking $\tau = 0.2\mu\text{s}$, $t = 80\mu\text{s}$, this gives:

$$\left(\frac{1 + H}{m + p} \right)^{\frac{1}{2}} \times \frac{40}{n} > 1 \quad (3.14)$$

Squaring and expanding:

$$40^2(1 + H) > n^2(m + p)$$

$$\therefore (m + p) < \frac{40^2(1 + H)}{n^2} \quad (3.15)$$

Now, as $k = n\omega_0$, $k^2 = n^2\omega_0^2$, and again substituting from (3.11) and (3.12) will obtain:

$$\{1 + m + p(1 + H)\}^2 = 4n^2(1 + H)(m + p) \quad (3.16)$$

Equations (3.15) and (3.16) can now be used to find the possible values of m , p and n using the information $0 < H < 35$, and the following conditions:

- (1) for adequate filtering, $m \geq 100p$
- (2) for H maximum, $p \geq 1$ for stability
- (3) for H minimum, $n = 1$ for critical damping.

Using conditions (1) and (3) on equation (3.15),

$$H = 0, n = 1$$

$$\therefore m + p < 40^2, \text{ but } m = 100p \therefore m + p = 1.01m$$

$$\therefore 1.01m < 1600$$

$$\text{or } m \approx 1600. \quad (3.17)$$

This is the maximum possible value for m , and so 16 is the maximum for p .

The maximum value that n can take is when m and H are maximum.

From (3.15),

$$m + p < \frac{40^2 \times 36}{n^2}$$

and

$$m + p < 1600$$

$$\therefore n^2 = 36, \text{ i.e. } n = 6.$$

From condition (3), we then have a range for n , i.e.

$$1 < n < 6 \tag{3.18}$$

Using conditions (1) and (2) on equation (3.16) for $H = 35$,

$$(1 + m + 36p)^2 = 4n^2 \times 36(m + p)$$

Now, $m = 100p$, $\therefore m + p = 101p$

$$\therefore (1 + 136p)^2 = 4n^2 \times 36 \times 101p$$

as $p \geq 1$, the term unity in the L.H.S. can be neglected.

$$\therefore (136p)^2 = 4n^2 \times 36 \times 101p$$

$$\therefore p = 0.78n^2.$$

Therefore, the minimum value that p could take is 0.78, but this is not allowed. The maximum value is 0.78×36 , but this is not allowed. $\therefore 1 < p < 16$ from the boundary condition (2), and the result of conditions (1) and (2) on equation (3.17), likewise $100 < m < 1600$.

The final condition on p that will give a reasonable value of m , thus allowing reasonable values of n and H , maximum and minimum, is purely practical. This is that there must be no current flowing in R_3 at the time of operation of the "hold" switch, as this would cause a disturbance in the charge on the hold capacitor C_2 , resulting in an erroneous value of bias being held.

Thus p was chosen as 3, so $m = 300$. This gave a value of R_2 and R_3 of about 2000Ω and 20Ω respectively, although R_2 was made into a variable resistance to allow for any small contribution to the stability or otherwise of the system due to those time constants

(3.1.4) and (3.1.5) ignored at the beginning of this chapter. With this system a stable bias circuit was achieved, capable of providing the required large range of gain.

3.3 Conclusions

This chapter has analysed the possible time constants involved in the bias system, and has shown how the present bias system has been designed to keep the number of time constants that cannot be neglected to a minimum. The electronic design of the bias control system has allowed two of these time constants to be incorporated, provided they are distinctly separated from any others.

The theory of the present bias system has shown that it may be stable under certain boundary conditions. Experimental values for the time constant τ and the pilot wave time have been put into the mathematics to give values for the two variables R_1 and R_2 which determine the other major time constant of the system. The validity of both the experimental value of τ and the bias theory has been proved by the fact that this system has exhibited the greatest stability yet, and has allowed the ultrasonic tomogram to work, albeit temporarily, to the degree of resolution originally envisaged in the design concepts.

Thus it may be seen that the development of the bias theory through consideration of all relevant time constants has first affected the design of the electronics, and secondly has utilised experimental data from the electronics to provide criteria for improved stability. It is believed that this bias control system is the answer to the problems of stability that have caused the major difficulties in the development of the ultrasonic tomogram, and that no further electronic design work is required. All that is necessary for satisfactory

operation of the tomogram, apart from a new reference transducer, is to calibrate the servomechanical system, and to adjust the stability servosystem to obtain maximum resolution. Hence no suggestions for further work on the bias theory or bias control system are necessary.

CHAPTER 4

Introduction to Diffraction Theory

4.1 Introduction

The next three chapters cover transducer diffraction theory for axisymmetric systems. A computer method is presented which can be applied to an acoustic field given by the general surface integral:

$$\phi_p = A \iint_S G dS \quad (4.1)$$

where A = arbitrary constant.

S = surface

G = any Green's function

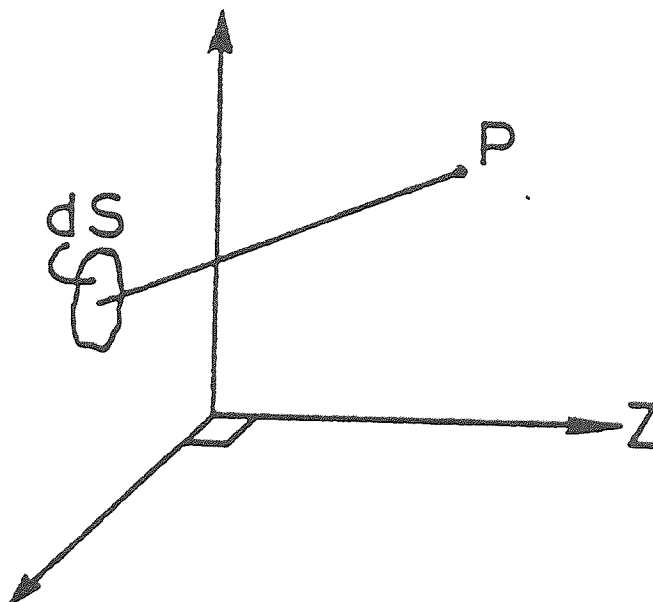


Fig. 4.1 Geometry of General Surface Integral

This integral is transformed by suitable geometry without approximation, to a single integral with fixed limits. Three Green's functions, corresponding to three sets of boundary conditions, have been applied to this method.

Until the geometrical transform described in Chapter 5 was used, no surface integral had been evaluated except for those involving the

Huygen integral. Hence comparisons can only be made with previous work from the Huygen integral results obtained using the techniques to be described in the following chapter.

An extension of this technique has been used to obtain the diffraction field for a ring transducer.

Experimental evidence is also presented which proves the accuracy of this method for a particular disc, with boundary conditions arranged to be those corresponding to the Huygen Green's function.

It has been realised that the form of the integral makes it possible to obtain expressions for the particle velocity at any point, which may be evaluated fairly simply. Values of particle velocity, in addition to pressure, have been computed in the plane of the transducer face to show the extent of agreement with theoretical boundary conditions.

The two components of particle velocity can be found at any point in the diffraction field. A method of envisaging the resultant particle velocity is described, by considering the direction of energy flow in the field. The concept used involves the defining of "diffraction fronts", in whose surface there is no energy transport. The energy flow lines and diffraction surfaces are computed and plotted for the three Green's functions already mentioned.

Although particle velocity has been calculated before (King, 1934, Oberhettinger, 1961, Greenspan, 1979, Archer-Hall and Hutchins, 1980), it has never been derived from the surface integral technique, because the integrals have not been in a form amenable to differentiation. This present technique has provided further information about the nature of the particle velocity vector that cannot be obtained from these Fourier-Bessel methods.

An alternative method of employing particle velocity is described in terms of intensity, which is the product of resultant velocity and pressure at the same point in the field. Three dimensional plots of energy intensity have been made which are similar to those obtained for pressure.

4.2 Green's Functions

A Green's function may be defined as one that obeys the d'Alembertian equation:

$$(\nabla^2 + k^2)G = 0$$

where $k = 2\pi/\lambda$

λ = wavelength

Fig. 4.2 overleaf shows three examples of Green's functions. These have been called the Huygen, Kirchhoff and Radiating Dipole functions. The choice of Green's function to be used in a particular case is dictated by the boundary conditions, and Fig. 4.2 illustrates diagrammatically the conditions to which each applies.

The conditions for the use of the Huygen function imply an ideally rigid infinite baffle surrounding the transducer. This imposes the boundary condition that the normal component of fluid velocity shall be zero in the $z = 0$ plane, except over the transducer face. In practice, a close approximation to these conditions would be a sonar device set in the side of a large ship.

The Kirchhoff function is appropriate for a transducer in a thin case, totally immersed in the acoustic medium. The rear wall of the case must be insulated from the transducer, and ideally rigid, thus imposing zero normal component of velocity on its surface.

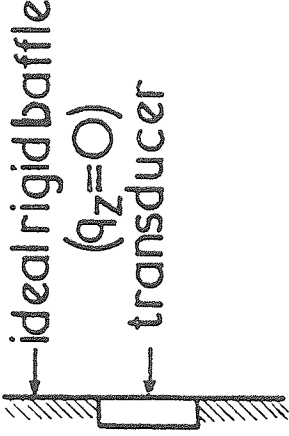
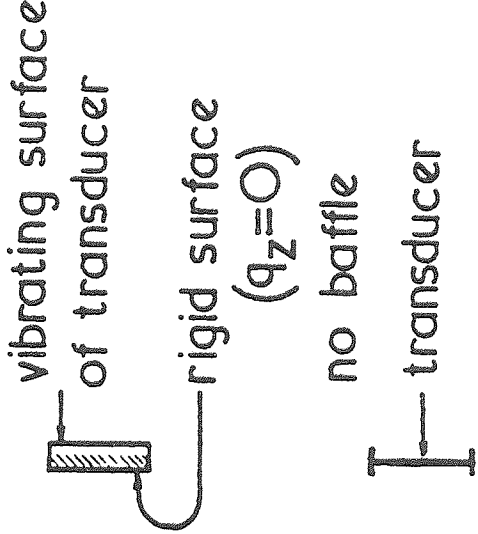

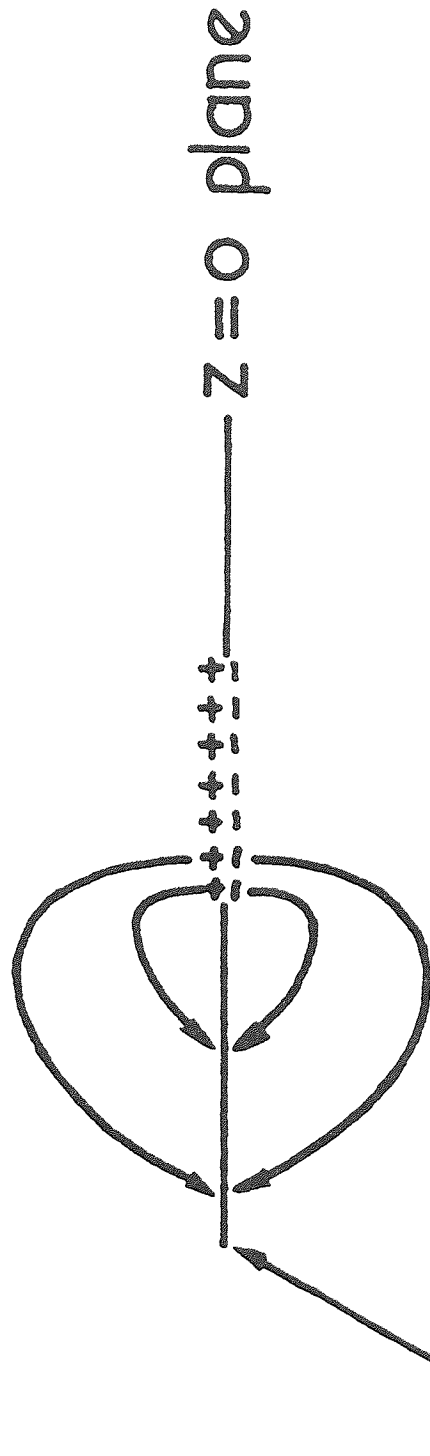
<u>Name</u>	<u>Green's Function</u>	<u>Boundary Conditions</u>
Huygen's	$\frac{e^{-jks}}{s}$	
Kirchhoff's	$\frac{e^{-jks}}{s} \left[jk \left(1 + \frac{Z}{s} \right) + \frac{Z}{s^2} \right]$	
Radiating Dipole	$\frac{e^{-jks}}{s} \cdot \frac{Z}{s} \left(jk + \frac{1}{s} \right)$	

Fig 4.2 Green's Functions

The theories of the Kirchhoff and Huygen integrals have been fully described by Baker and Copson (1939), Morse and Ingard (1968) and Coulson and Jeffrey (1977). The third of these functions, the Radiating Dipole, has only recently been used in a suitable form for ultrasonic diffraction studies. Fig. 4.3 illustrates the boundary conditions for this function, which are such that the acoustic pressure is zero in the $z = 0$ plane, outside the disc. The condition is appropriate for an air to liquid or air to solid interface on which the transducer is applied, and is much closer to that found in medical ultrasonography than for either of the other two functions.



$P \equiv 0$ as contributions
cancel outside disc

Fig 4.3 Boundary Condition of Radiating Dipole

CHAPTER 5
Radiating Dipole

5.1 Derivation of Radiating Dipole Green's Function

The Radiating Dipole Green's function is derived by considering an array of acoustic dipoles as a model. This is mathematically identifiable with the case of a freely suspended un baffled disc in an infinite medium.

Consider the single dipole shown in Fig. 5.1. It consists of two point sources, S_1 and S_2 , 180° out of phase, a distance 2δ apart. Each source is represented by the function for a spherical wave:

$$\phi_1 = \frac{e^{-jks_1}}{s_1} \quad \text{for source } S_1$$

$$\phi_2 = -\frac{e^{-jks_2}}{s_2} \quad \text{for source } S_2$$

The Radiating Dipole Green's function is a combination of these two sources:

$$G = \phi_1 + \phi_2 = \frac{e^{-jks_1}}{s_1} - \frac{e^{-jks_2}}{s_2} \quad (5.1)$$

as $\delta \rightarrow 0$, this function becomes:

$$G = \frac{\delta}{\delta z} \frac{e^{-jks}}{s}$$

$$= \left(-jk - \frac{1}{s}\right) \frac{e^{-jks}}{s} \frac{\delta s}{\delta z} \quad (5.2)$$

Since $\frac{\delta s}{\delta z} = -\cos\theta$ as $\delta \rightarrow 0$,

and $\cos\theta = \frac{z}{s}$ from the geometry of Fig. 5.1,

$$G = \left(jk + \frac{1}{s}\right) \frac{e^{-jks}}{s} \cdot \frac{z}{s} \quad (5.3)$$

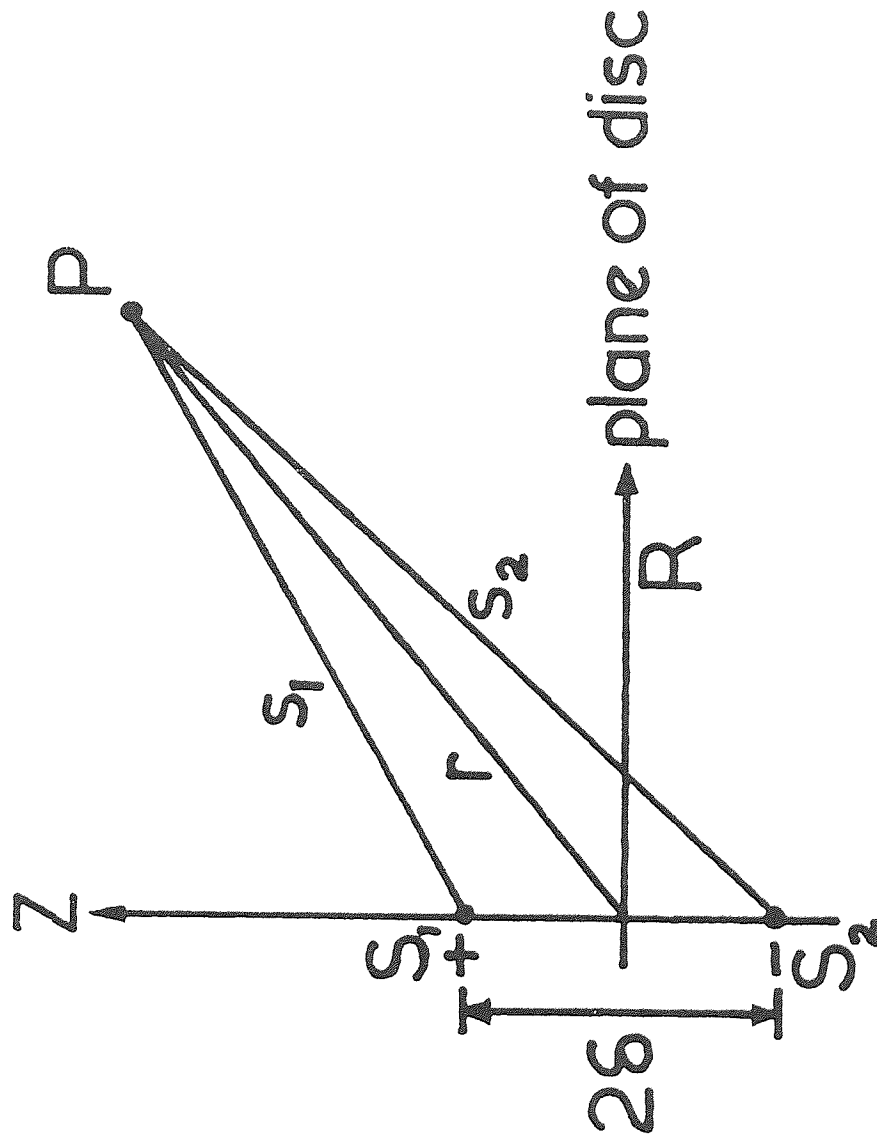


Fig 5.1 Single Dipole

Thus the integral describing the acoustic field for the free surface boundary conditions is:

$$\phi_p = A \iint_S \frac{e^{-jks}}{s} \cdot \frac{z}{s} \left(jk + \frac{1}{s} \right) dS \quad (5.4)$$

from the general equation for a diffraction field (4.1) mentioned in the introduction, where A is an arbitrary normalising constant.

For all three Green's functions illustrated in Fig. 4.2, it is possible to evaluate the surface integral for a disc analytically at an axis point. This is necessary for the present technique.

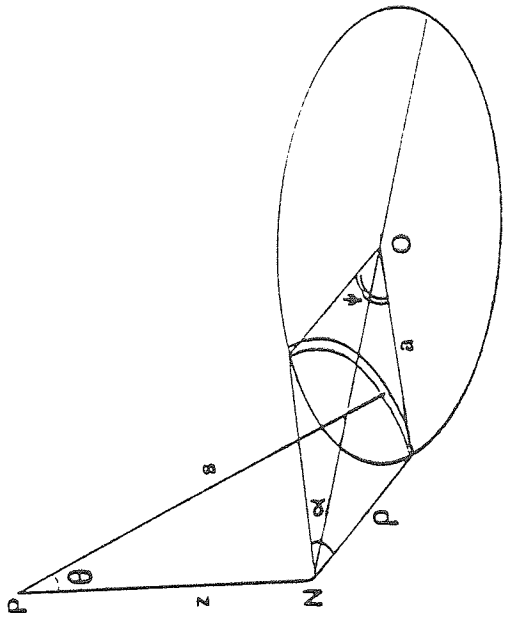
These three double integrals can be turned into single integrals by applying the geometry shown in Fig. 5.2 (Archer-Hall, Bashter, Hazelwood, 1979), which has to be considered separately for two cases. Fig. 5.2(a) applies to points whose normals to the $z = 0$ plane fall within the disc, and Fig. 5.2(b) where they fall outside. The reason for selecting this geometry is that for areas dS on the circular arcs ΔS shown, the length s and the ratio z/s are constant. This geometry has been suggested by Stepanishen (1971), but without description as to how it could be applied.

Omitting the arbitrary constant from equation (5.4) the integral required is:

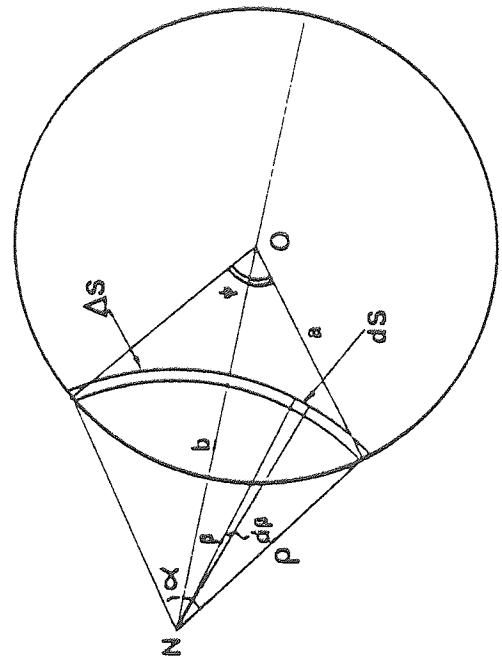
$$\begin{aligned} I &= \iint_S \frac{e^{-jks}}{s} \cdot \frac{z}{s} \left(jk + \frac{1}{s} \right) dS \\ &= \int_{s_1}^{s_2} \int_{-\alpha}^{+\alpha} \frac{e^{-jks}}{s} \cdot \frac{z}{s} \left(jk + \frac{1}{s} \right) \rho d\rho d\beta \end{aligned} \quad (5.5)$$

The first stage of integration can now be performed with respect to the only remaining variable, β :

$$I = \int_{s_1}^{s_2} \frac{e^{-jks}}{s} \cdot \frac{z}{s} \left(jk + \frac{1}{s} \right) 2\alpha \rho d\rho \quad (5.6)$$



(a)



(b)

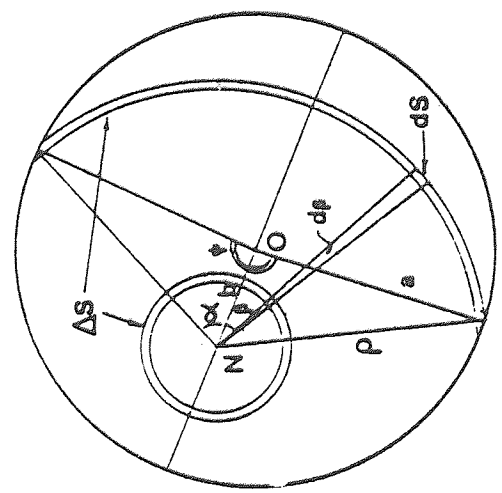
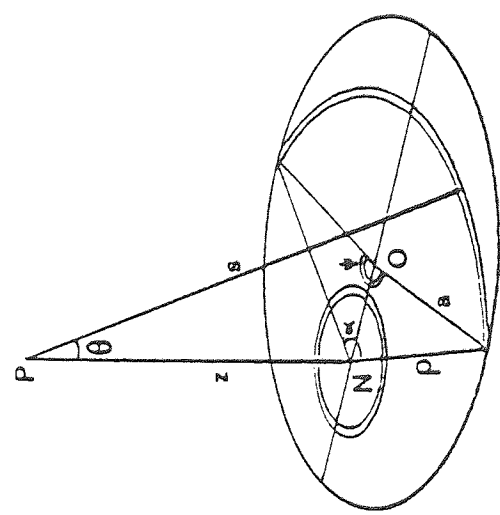


Fig 5.2 Transform Geometry

Now, from the geometry of Fig. 5.2

$$\rho d\rho = s ds \quad \text{as } s^2 = z^2 + \rho^2$$

and z is constant.

$$\therefore I = 2 \int_{s_1}^{s_2} e^{-jks} \frac{z}{s} \left(jk + \frac{1}{s} \right) \alpha ds \quad (5.7)$$

Let the factor 2 become part of the arbitrary constant A , which will be found later by normalising. The last equation can now be integrated by parts giving:

$$I = \left| - e^{-jks} \cdot \frac{z}{s} \cdot \alpha \right|_{z_1}^{s_1} \quad (5.8a)$$

$$+ \int_{z_1}^{s_1} - e^{-jks} \cdot \frac{z}{s} d\alpha \quad (5.8b)$$

The term (5.8a) becomes e^{-jkz} for points where $b < a$ and zero for $b > a$, i.e. outside the disc. The enumeration of the remaining integral (5.8b) by computer is facilitated by substituting for $d\alpha$ in terms of the angle ψ subtended by the ends of the arc elements ΔS at 0, as follows:

$$\cos \alpha = \frac{(b^2 - a^2 + \rho^2)}{2b\rho} \quad (5.9)$$

$$\cos \psi = \frac{(b^2 + a^2 - \rho^2)}{2ab} \quad (5.10)$$

$$\frac{\sin \alpha}{a} = \frac{\sin \psi}{\rho} \quad (5.11)$$

by sine and cosine rules. By differentiating equation (5.9) with respect to ρ , and substituting from equation (5.11) into the result:

$$\sin \psi \frac{d\alpha}{d\rho} = \frac{b^2 - a^2 - \rho^2}{2ab\rho} \quad (5.12)$$

differentiating equation (5.10) with respect to ρ , and dividing equation (5.12) by the result gives:

$$\frac{d\alpha}{d\psi} = \frac{b^2 - a^2 - \rho^2}{2\rho^2}$$

and from equation (5.10)

$$d\alpha = \left(\frac{ab \cos\psi - a^2}{a^2 + b^2 - 2ab \cos\psi} \right) d\psi \quad (5.13)$$

where $s^2 = z^2 + \rho^2 = z^2 + a^2 + b^2 - 2ab \cos\psi$.

The final equation presented to the computer after normalisation is:

$$\phi = e^{-jkz} + \frac{1}{\pi} \int_0^\pi e^{-jks} \cdot \frac{z}{s} \left(\frac{ab \cos\psi - a^2}{a^2 + b^2 - 2ab \cos\psi} \right) d\psi \quad (5.14)$$

(only for $b < a$)

Thus the evaluation of I in the general case involves the computation of a single integral with fixed limits, and the addition of a term such as e^{-jkz} for $b < a$, but not for $b > a$, as this is zero outside the disc.

For the actual process of computation, the two terms e^{-jkz} and the integral are split into real and imaginary parts. The integration is performed using Patterson's quadrature method (Patterson, 1968, 1973), called from a NAG library subroutine. The modulus of the acoustic potential ϕ is found by taking the square root of the sum of the squares of the real and imaginary results.

Values have been plotted graphically using GINO and GINOSURF subroutines, to give "axis plots" ($r = \text{constant}$), "cross plots" ($z = \text{constant}$), or three dimensional isometric plots by varying both r and z .

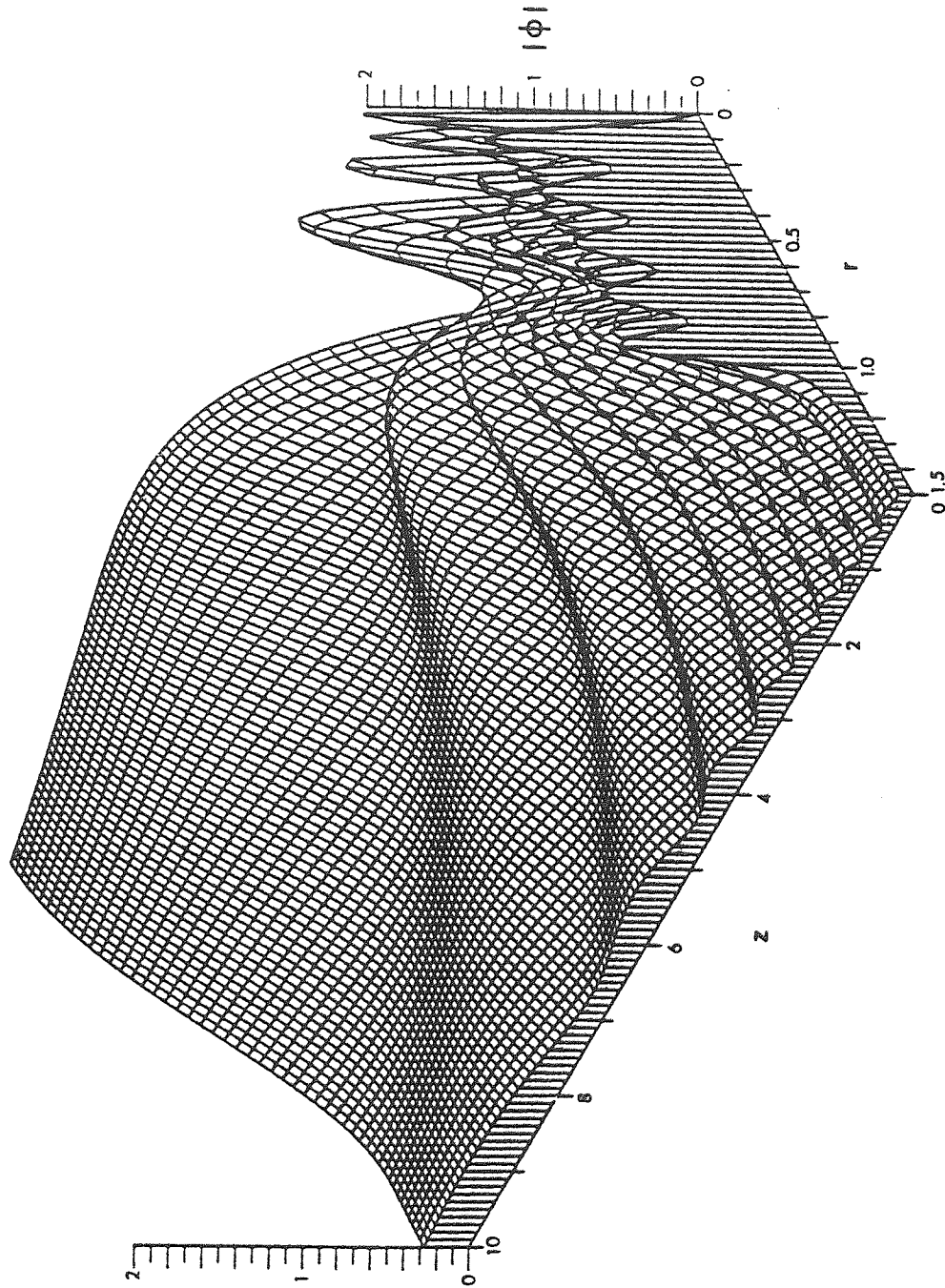
5.2 Theoretical Results

For comparison against previous work plotted in other papers (Zemanek, 1971, Lockwood and Willette, 1973, Hutchins, 1978, Archer-Hall et al, 1979, 1980), most of the graphs were plotted with $a = 5\lambda$, where a is the disc radius.

Figs. 5.3, 5.4, 5.5, 5.6 and 5.7 show the three dimensional plots of the Huygen, Kirchhoff and Radiating Dipole diffraction fields. Fig. 5.3 agrees with the three dimensional plot produced by Zemanek, who used a far greater amount of computing time in evaluating a complete double integral as a double summation. The new algorithm has been estimated to give a factor of at least 30,000 times less computing "costs" (see Appendix 4) than the Zemanek algorithm (1971). Lockwood and Willette (1973) estimated their single integral technique to be a/λ times better than that of Zemanek, and hence the technique presented here is at least 5,000 times better, for $a = 5\lambda$, than Lockwood and Willette's. Again, agreement of results from the Huygen plots using the present technique is very good with the steady state results in the paper by Lockwood and Willette (1973).

Figs. 5.6 and 5.7 illustrate a further advantage of the GINOSURF graphplotting subroutines, in that the three dimensional model can be "turned around" to show any of four views, without having to compute any further results. This extra latitude of graphical illustration has not been presented in previously published work, as many subroutines require the results to be computed anew for each diagram.

Figs. 5.8 and 5.9 are the axis plots ($r = 0$) and cross plots ($z = 0$) of the Radiating Dipole function, compared with those of the Kirchhoff and Huygen functions. In the axis plots, the salient features are that the Huygen integral gives a set of zero minima and



$$a = 5\lambda$$

Fig 5.3 Huygen Three Dimensional Diffraction Field

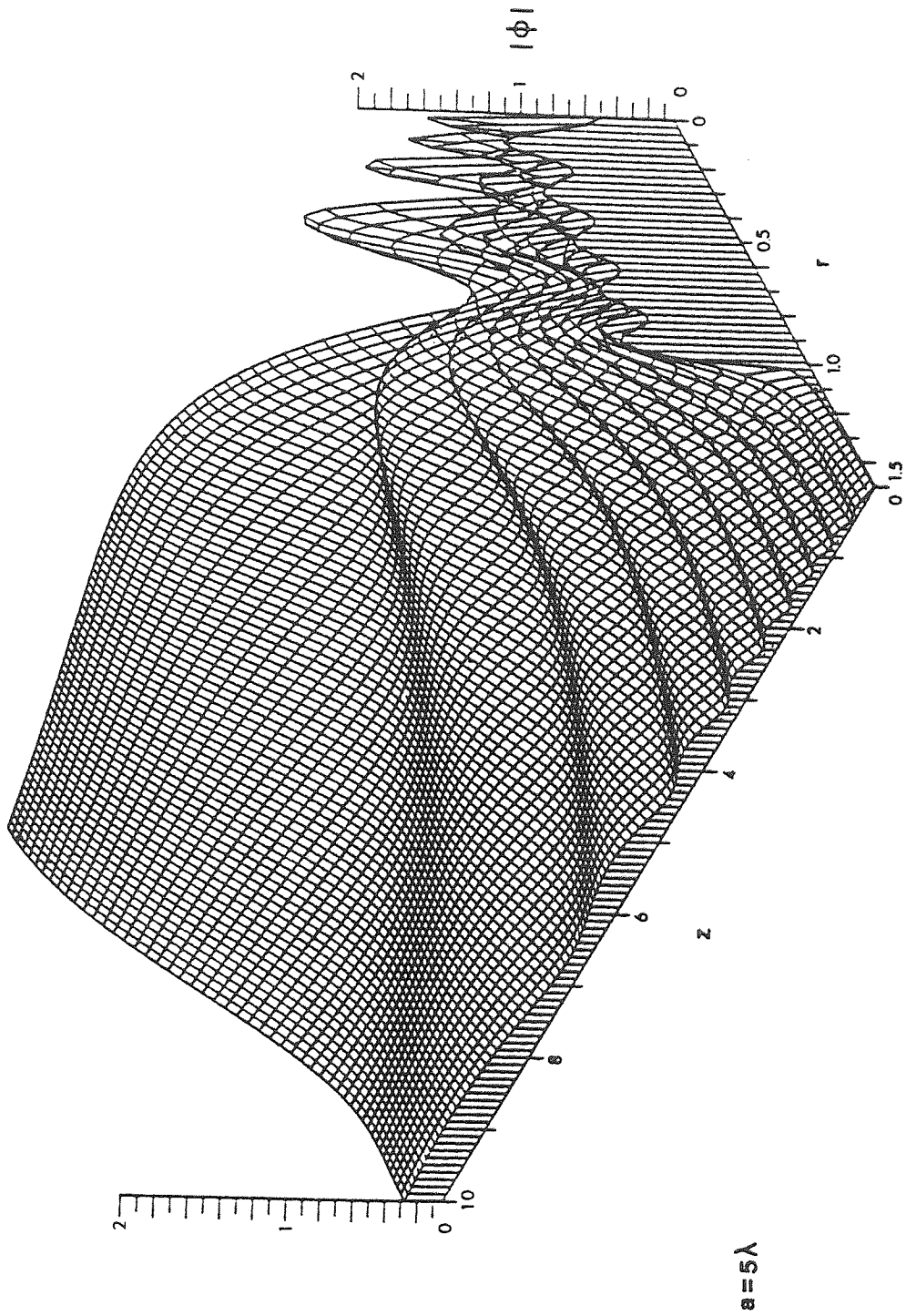


Fig 5.4 Kirchhoff Three Dimensional Diffraction Field

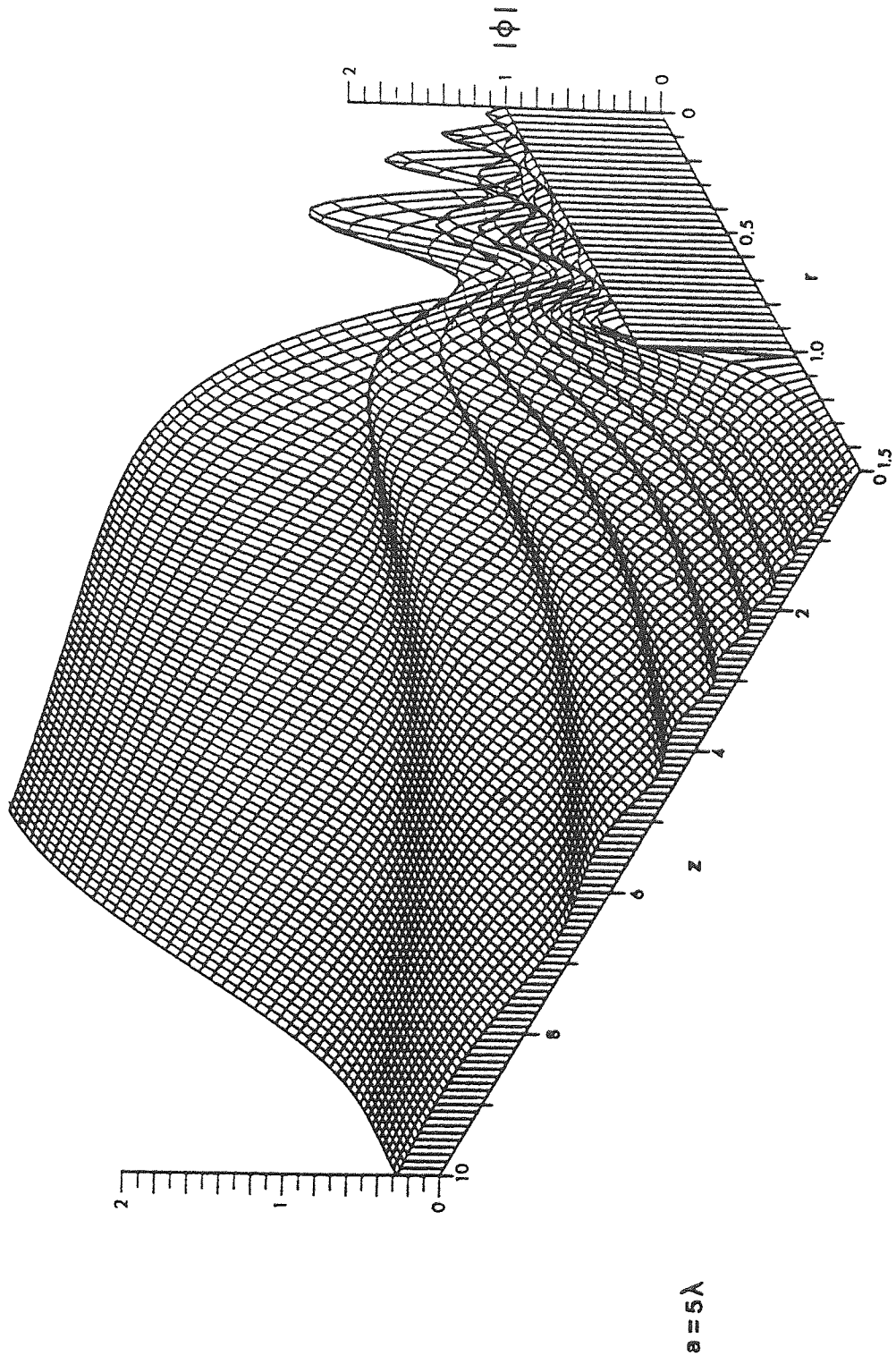
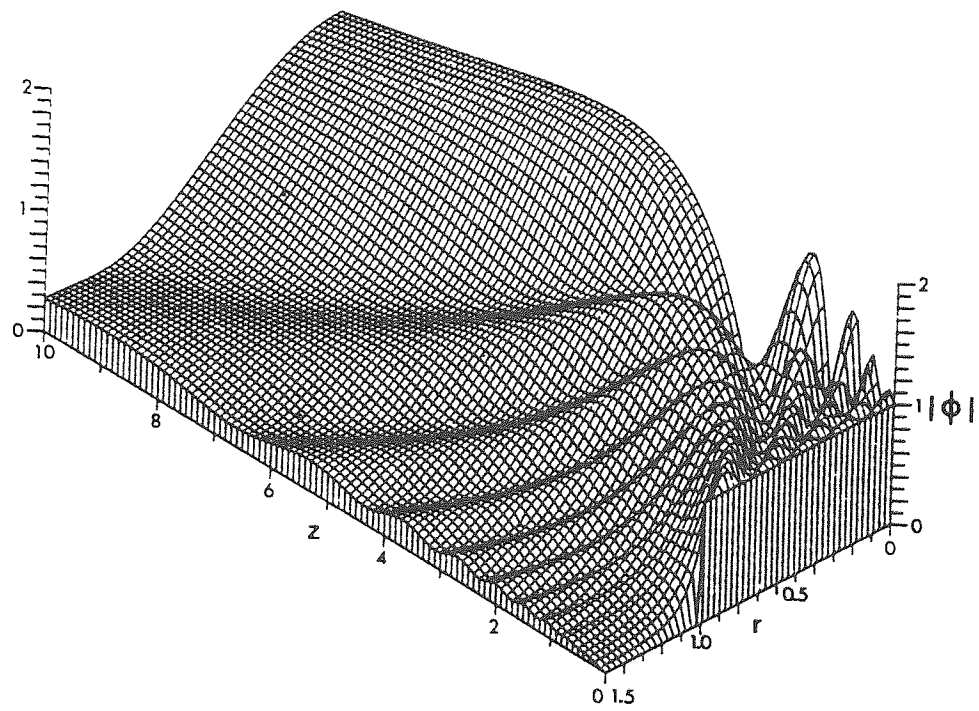


Fig 5.5 Radiating Dipole Three Dimensional Fraction Field



$$a = 5\lambda$$

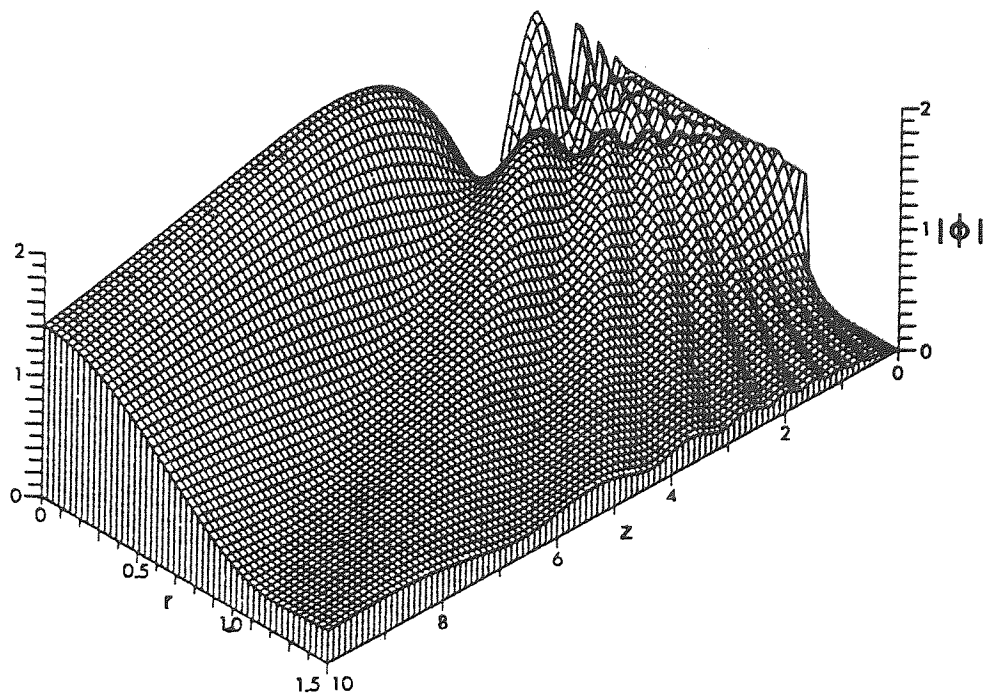
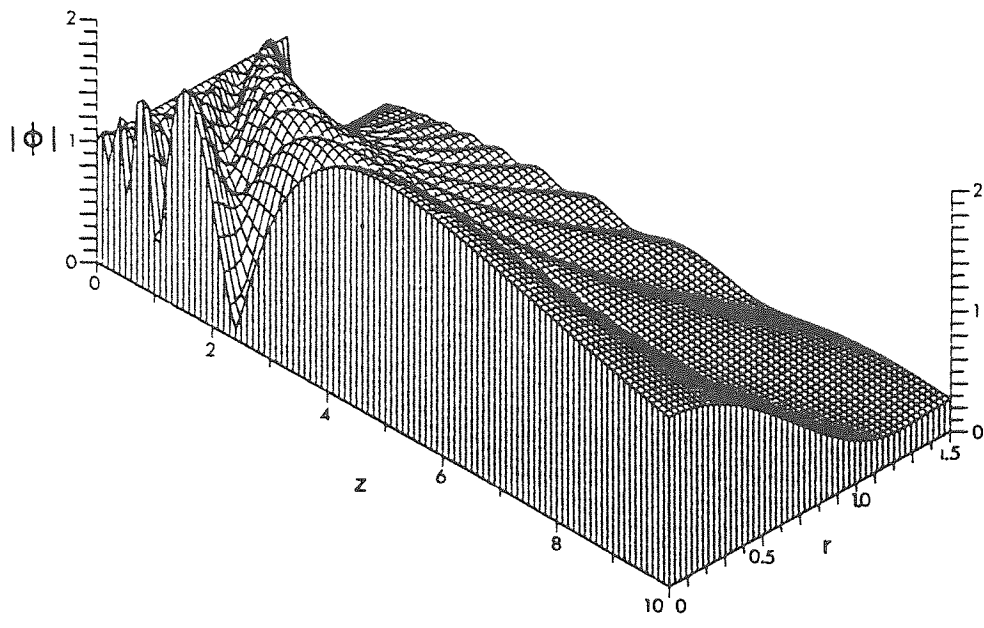


FIG.5.6 Alternative Views of Radiating Dipole Field



$$a = 5\lambda$$

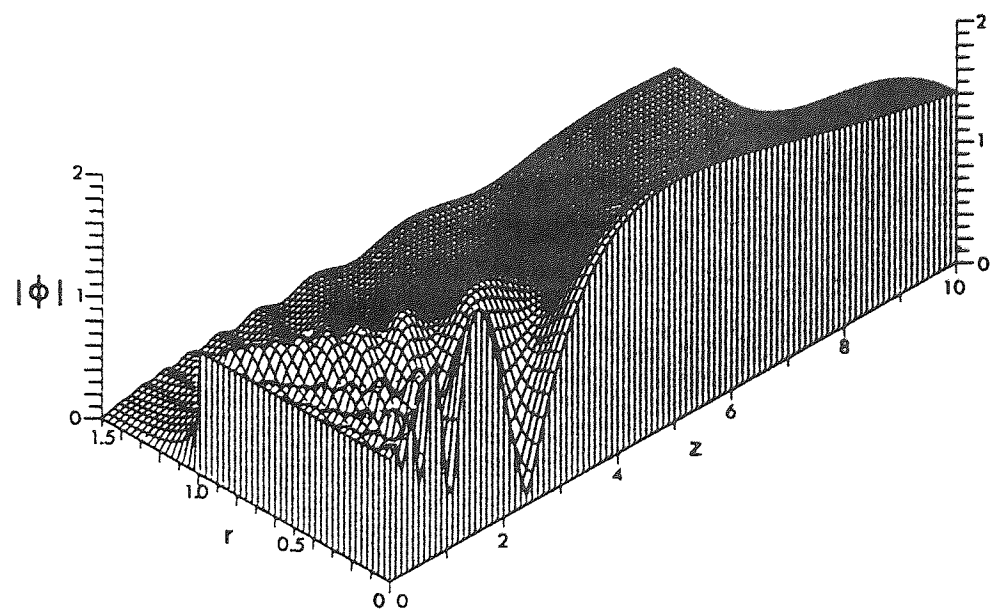


FIG.5.7 Alternative Views of Radiating Dipole Field

and equal maxima, the Kirchhoff varies less, and the Radiating Dipole less still. All three converge to the same result in the Fraunhofer far-field region.

The cross plot illustrates a boundary condition for the Radiating Dipole that the acoustic potential, and thus the pressure, is zero outside the disc face in the $z=0$ plane. The Radiating Dipole has a constant pressure across the disc face, and again the Kirchhoff varies about this value and the Huygen varies even more. In fact, the Huygen results even predict a zero in the centre of the transducer face.

Comparison of these results with workers using transient techniques (e.g. Oberhettinger, 1961, Freedman, 1960, 1962, 1970, 1971, 1972, 1977, Stepanishen, 1971, 1972, 1974, 1976, 1978, Robinson et al, 1974, and Weyns, 1980) cannot be made unless their methods allow for steady state solutions, as does that of Lockwood and Willette. Other workers have achieved steady state solutions by using first the transient approach of Lockwood and Willette and Stepanishen, and then considering single frequencies, but have tended to solve for square or curved transducers. Excellent three dimensional results are presented by Penttinen and Luukkala (1976) for a curved transducer, but no comparison of computing "costs" is made. The comparisons mentioned, however, only involve the Huygen integral, as very few workers have attempted other boundary conditions except Dekker, Piziali and Dong (1974), and Greenspan (1979). Of these two, the former investigated damped oscillators, finally concluding that further work was required on the understanding of the boundary conditions. The latter had little understanding of the conditions at all, dividing them into two distinctly separate types, Dirichlet (pressure) and Neumann (particle velocity), and solving for each, without considering a practical situation where both may arise together.

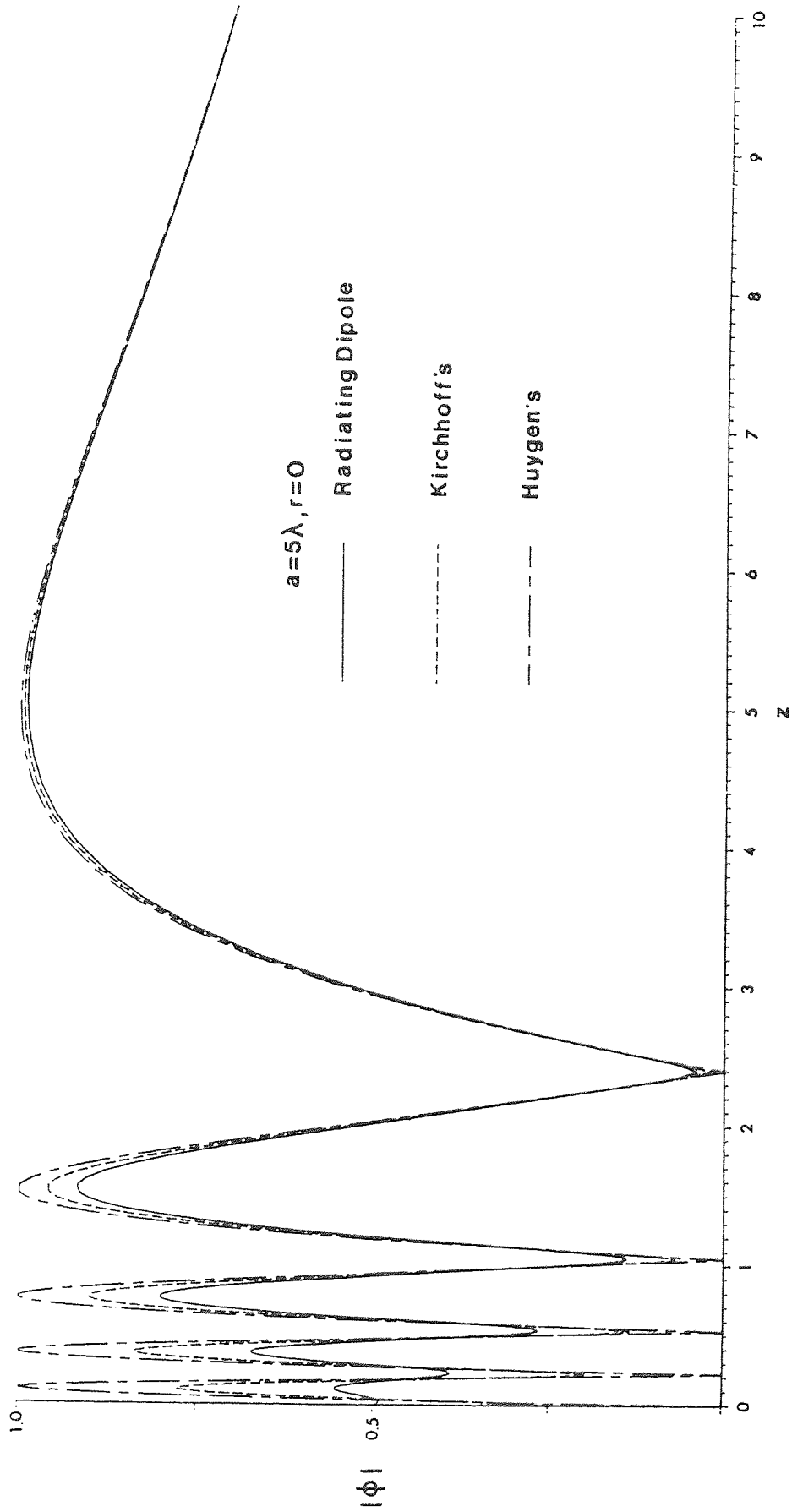


Fig 5.8 Axis Plots

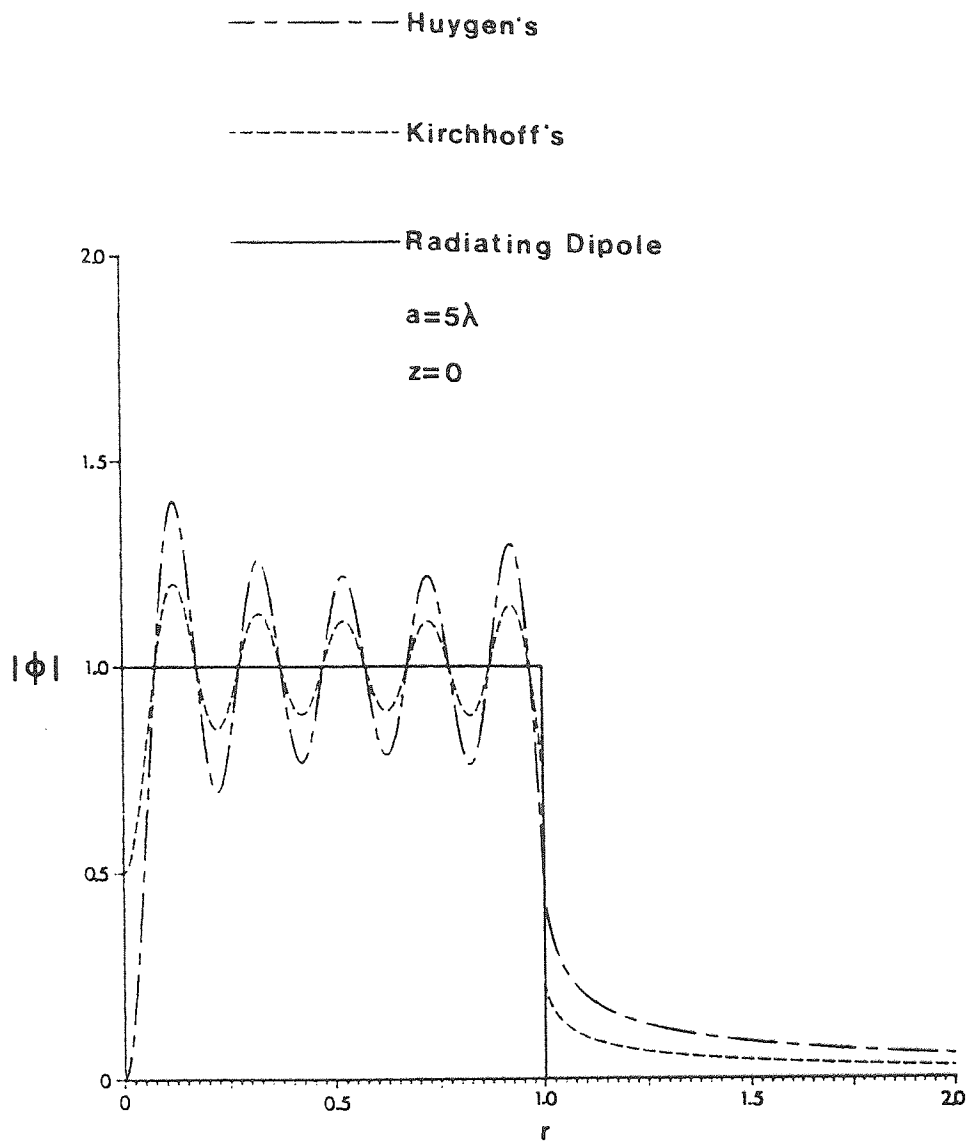


FIG.5.9 Cross Plots

No literature has been found in ultrasonic diffraction theory that deals with the Radiating Dipole function, except the alternative approach of King (1934) which has been developed by Hutchins (1978) and Archer-Hall and Hutchins (1980) to take account of varied boundary conditions. Comparison of the results of the two methods show the single integral technique to be more reliable, although further work is required to remove artefacts in the results of Archer-Hall and Hutchins.

The Kirchhoff boundary conditions have been discussed in various parts of the literature, e.g. Spence (1949), but no computations of the complete field have been made until Archer-Hall et al (1978), and then no mention was made of the boundary conditions of the transducer that this theory would describe. Only now is it possible to examine these boundary conditions by considering the forms of the three single integrals after geometrical transformation.

The technique already described has been extended to deal with ring transducers using the Radiating Dipole function. This is done by subtracting the real and imaginary results for two discs of slightly different radii before the modulus is taken.

A ring has been arranged to have a width of 4λ , operating at $a = 25\lambda$. For a real ring of 4 cm. diameter, this gives a ring width of 3.2 mm, with an ultrasonic frequency in water of about 2 MHz.

Figs. 5.10 and 5.11 show a series of cross plots and an axis plot, which clearly illustrate a workable "tube" of focus from about $5a$ to $15a$, i.e. 10 cm to 30 cm from the disc face. A three dimensional plot of this diffraction field, Fig. 5.12, shows the focus "tube" quite distinctly. Two other values for the ring width, 2λ and 8λ , have been investigated, but 4λ appears to be an optimum.

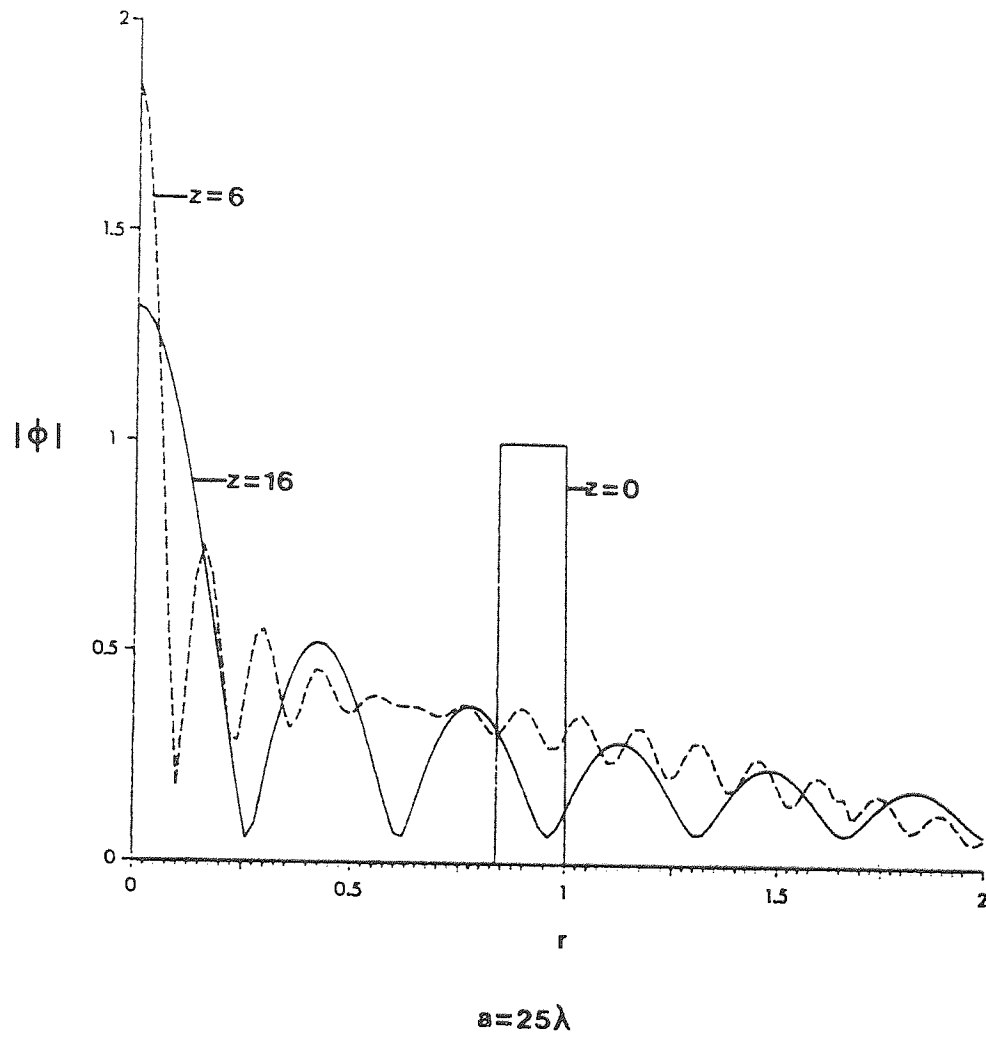


FIG.5.10 Ring Transducer Cross Plot

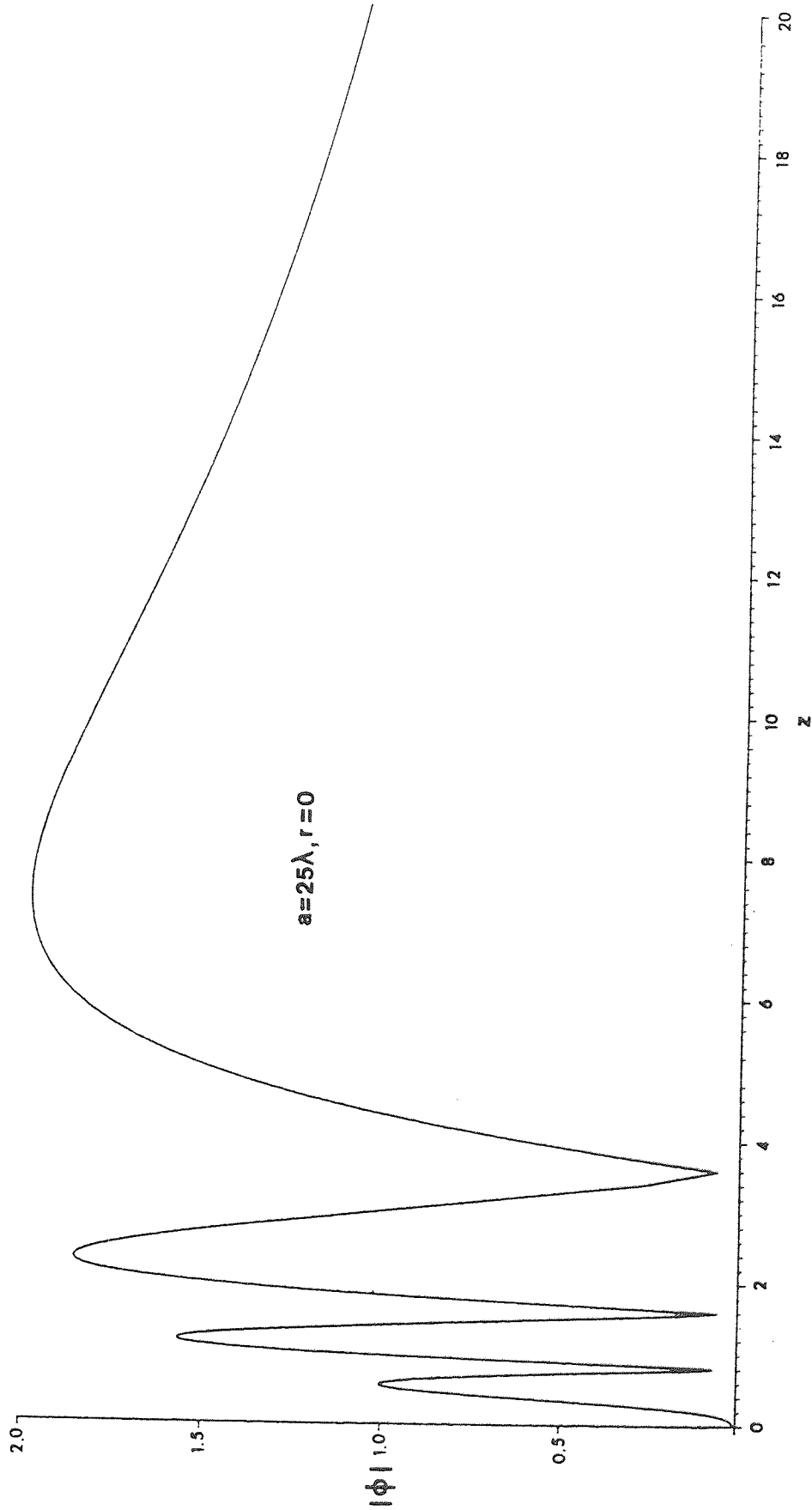


Fig 5.11 Ring Transducer Axis Plot

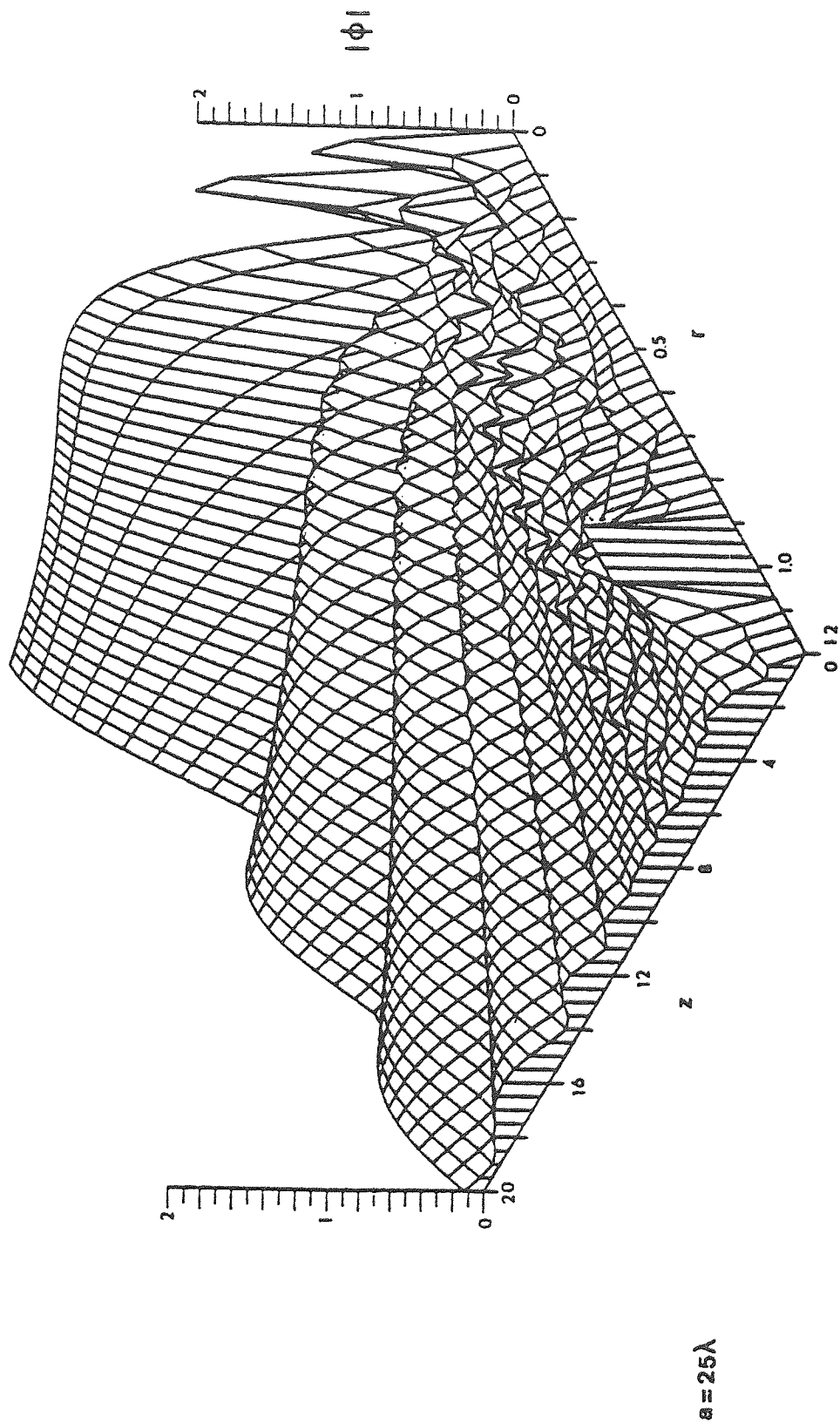


Fig 5.12 Three Dimensional Ring Transducer Diffraction Field

The practical application of such a transducer is open to some discussion, for it seems that a thin ring of a particular width may be able to give as good a resolution as methods involving zone delay focussing with elaborate electronics used at present in medical ultrasonography (Wells, 1963, 1969, 1972, 1977, Macovski, 1979).

Although several of the theoreticians already mentioned have dealt with ring transducers, again comparisons cannot be made, as this is the first time such a configuration has been computed using the Radiating Dipole function. In fact, no steady state acoustic fields for ring transducers have been computed even for the Huygen function, although this should be possible using either the Zemanek or Lockwood and Willette transforms. Such an investigation has not been attempted, probably because the extra computing time using such cumbersome algorithms may prove to be prohibitive.

5.3 Experimental Results

An experiment has been devised to confirm the theoretical results of the Huygen type transducer. The boundary conditions for the Huygen Green's function imply that the transducer is surrounded by an ideally rigid, perfectly reflecting baffle. A close practical approximation to these conditions is shown in plate 5.1.

The baffle is made of an asbestos and concrete mixture, measuring about 2m by 2.6 m by 2.5 cm thick. The transducer was arranged to have a diameter of 48 mm, and was provided with two aluminium cylinders, attached to the front and back faces. This caused the PZT planar transducer to be resonant at 16.65 KHz, as opposed to its natural resonance of 200 KHz. The reasons for this were two-fold. The most important reason was to attempt to keep the radiating face in a common

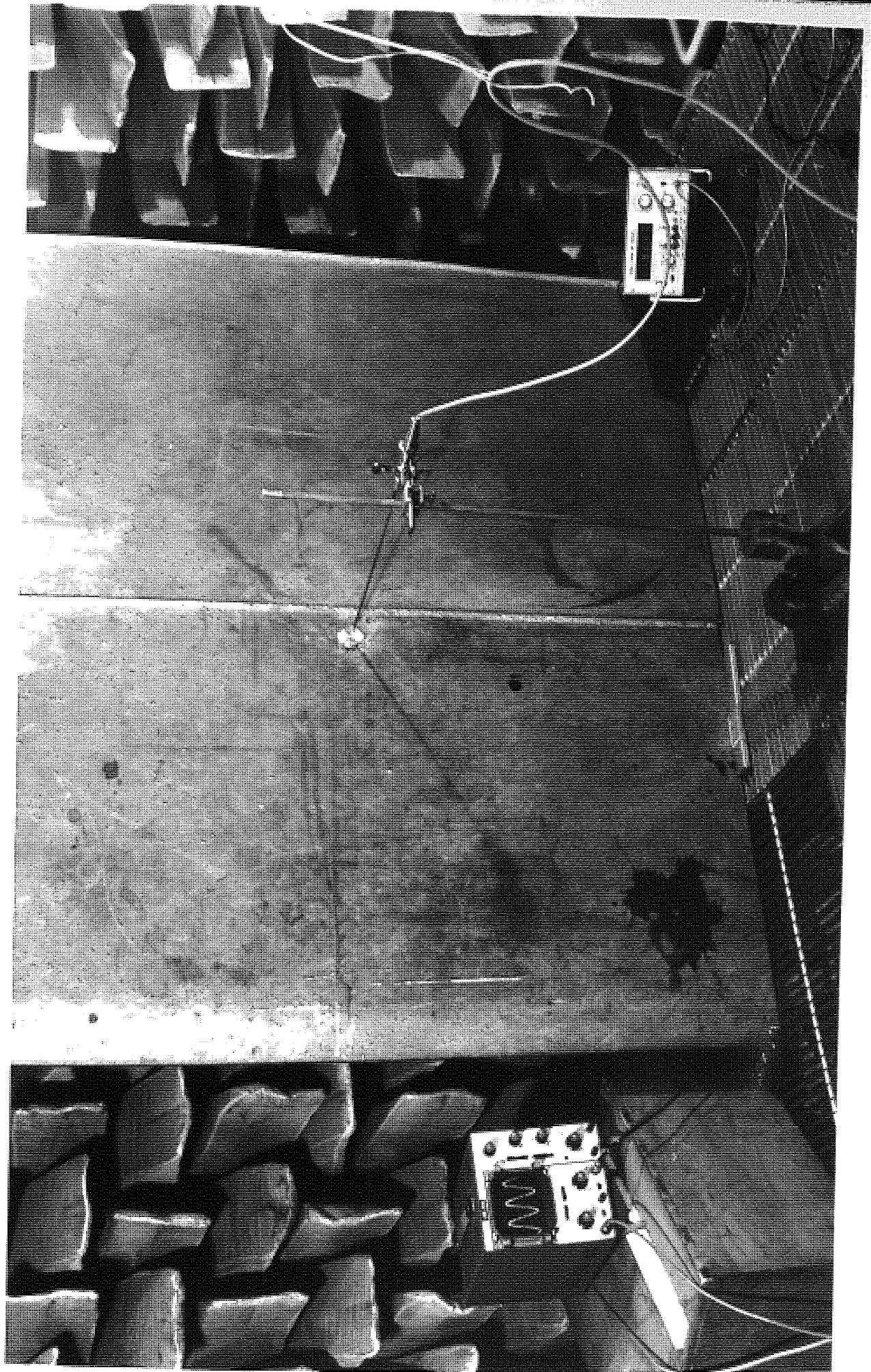


Plate 5.1. Experimental Investigation of Huygen Function

phase and amplitude, the second reason being to reduce the frequency to the audio range to enable the baffle to approximate more closely to the conditions of ideal rigidity and perfect reflectivity.

A Bruhl and Kjør capacitor microphone, fitted with a long thin pressure sampling tube, was used to measure the R.M.S. pressure. The instrument was traversed by a long screw drive, servocoupled to the plotting paper. The experiment was designed to be done in air to ensure almost perfect reflection at the baffle surface, giving zero normal velocity in the $z = 0$ plane.

Figs. 5.13 and 5.14 show the experimental axis plot compared with that computed for the same value of $a = 1.2\lambda$ used. Agreement between theoretical and practical results is good, the lack of a smooth experimental trace being due to the finite element of pen recorder response.

Again, comparison with other published results is difficult, as these usually involve measurement of transient responses, which are used more commonly in medical ultrasonics (e.g. Shaw, 1956, Shaw and Sijur, 1960, Lobdell, 1966, Kikuchi, 1969). However, two sets of published results have been found, namely papers by Allipi and Palmieri (1971), and Weight and Hayman (1978), in which steady state Huygen radiators have been examined. Both methods involve Schlieren photography (Newman, 1973, Hutchins, 1978, Archer-Hall and Hutchins, 1979, 1981). Unfortunately, Allipi and Palmieri decided to conduct their experiments on rectangular transducers, and hence cannot be compared, as the present theoretical technique is purely for axisymmetric systems.

The results obtained by Weight and Hayman, however, can be compared in part to those obtained here. Before going into an extensive investigation of transient response, Weight and Hayman measured the on-axis amplitude for a long pulse of continuous 1 MHz ultrasonic waves.

Fig 5.13 Experimental Huygen Axis Plot

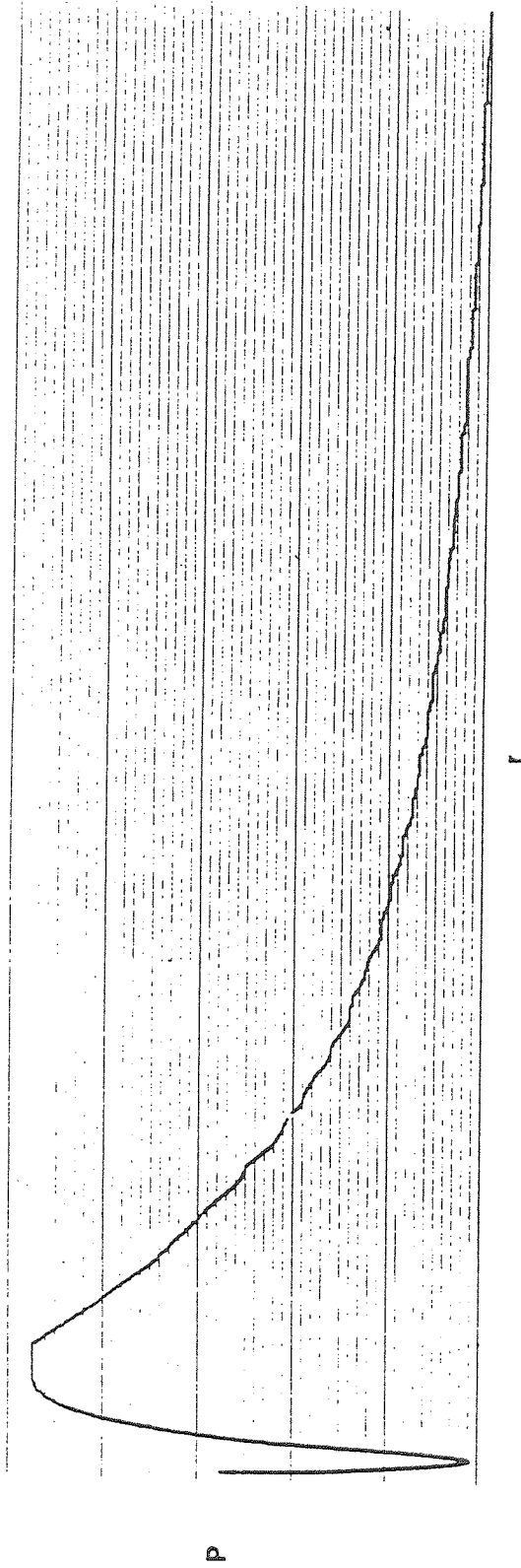
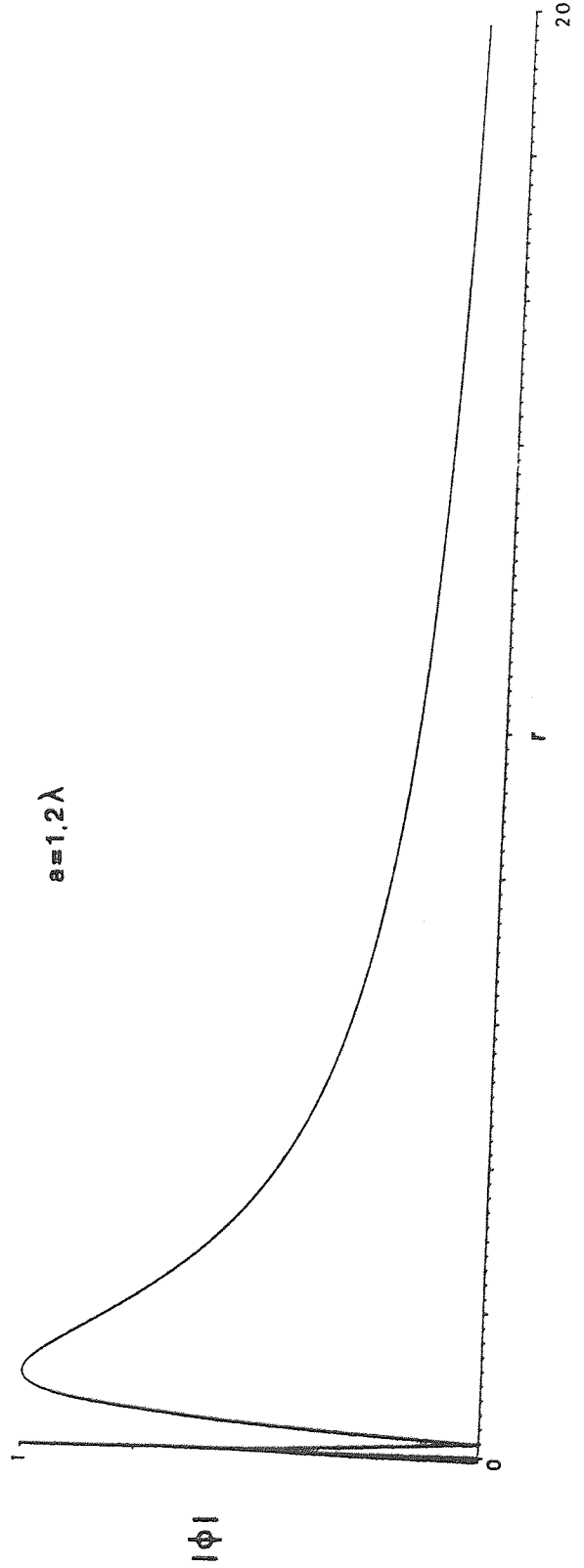


Fig 5.14 Computed Huygen Axis Plot



Although the graphical results depicted are rather unclear, it does appear that their experimental results did not fit as well as those shown here. This could be for two possible reasons. The first reason is that the present experiment was performed in an anechoic chamber, and hence reverberations from the walls of the chamber could be neglected. The second reason for the fit not being perfect is that the transducer and baffle used were not made to fit the boundary conditions of a Huygen radiator as carefully as in the experiment described in this chapter. Although the transducer construction is described, no mention is made about the reflectance and extent of the baffle. It is suspected that because the baffle was not perfectly reflecting, Weight and Hayman have failed to record zeros as predicted by the Huygen theory for on-axis pressures.

The close adhesion to the Huygen boundary conditions in the present experiment is one advantage over the Weight and Hayman apparatus. Another advantage is that the wavelength is about 60 times longer in the experiment described here, which enables the manufacture of a larger probe, and still avoids any great disturbance of the diffraction field due to reflections from the probe.

5.4 Conclusions

It has been realised that the geometrical transform first developed by Archer-Hall et al (1978) can be used to obtain the diffraction pattern of any Green's function. Consideration of the transducer boundary conditions found in medical ultrasonography has led to the derivation of the Radiating Dipole Green's function in a form amenable to transformation and hence computation of its diffraction pattern. This particular function has never been evaluated before using the surface

integral technique, and the results obtained have been shown to be better than those from the Fourier-Bessel technique of Hutchins (1978) and Archer-Hall and Hutchins (1980).

Further work in this area would involve the examination of the boundary conditions of transducers used in other cases, such as in non-destructive testing and physiotherapy on limb joints. This might lead to the development of other Green's functions that could be processed to find their diffraction patterns using the geometrical transform and computation already developed.

The technique has been extended to deal with ring transducers, and the results obtained have pointed to the possible replacement of zone-delay focussing techniques by ring transducer techniques. The resolution of only a few rings has been examined, and further work is needed in this area. The technique could also be used to investigate series of concentric rings of differing widths in an attempt to make the focus more defined.

The results of the Radiating Dipole ring transducer have been found, but those of the Huygen and Kirchhoff could also be computed. It is possible to write a program that could compute the results using either the Zemanek (1971) or Lockwood and Willette (1973) algorithms. Although this may result in prohibitive computing costs, agreement between the three techniques could then be further examined.

An experiment to confirm the results of the Huygen diffraction pattern has been performed that is believed to yield better results than those previously obtained for steady state solutions. Further work in this field could be in the devising of an experiment to determine the diffraction pattern of a transducer with boundary conditions of the Radiating Dipole Green's function. It may be possible to arrange the

"pressure release" conditions by suspending the transducer just on the surface of a water and air interface, but complications may occur as measurements would have to be taken in the water. It is considered that the boundary conditions for the Kirchhoff Green's function could not easily be fabricated. This is probably due to the fact that they are a mixture of the conditions of the other two Green's functions mentioned.

Comparison with impulse response or transient techniques could also be examined. This would involve either transforming all the results obtained by these techniques into steady state solutions, a Herculean and probably impossible task, or developing a method of transforming the technique described here to deal with transients or pulses. It is believed that this problem may be approached by use of a Fourier technique, or the insertion of a Dirac delta function into the surface integral, but no work has yet been done on this problem.

CHAPTER 6
Particle Velocity

6.1 Derivation of the Particle Velocity

One conclusion to be drawn from the previous chapter can be illustrated here. The three Green's functions for the acoustic potential shall be called ϕ_H , ϕ_K and ϕ_{RD} for the Huygen, Kirchhoff, and Radiating Dipole functions respectively. After normalisation and transformation into forms suitable for computation, these functions are:

$$\phi_H = e^{-jkz} + \frac{1}{\pi} \int_0^\pi e^{-jks} \left(\frac{\arccos\psi - a^2}{a^2 + r^2 - 2ar\cos\psi} \right) d\psi \quad (6.1)$$

$$\phi_K = e^{-jkz} + \frac{1}{2\pi} \int_0^\pi e^{-jks} (1 + z/s) \left(\frac{\arccos\psi - a^2}{a^2 + r^2 - 2ar\cos\psi} \right) d\psi \quad (6.2)$$

$$\phi_{RD} = e^{-jkz} + \frac{1}{\pi} \int_0^\pi e^{-jks} \frac{z}{s} \left(\frac{\arccos\psi - a^2}{a^2 + r^2 - 2ar\cos\psi} \right) d\psi \quad (6.3)$$

$$\therefore \phi_K = \frac{\phi_H + \phi_{RD}}{2} \quad (6.4)$$

Thus the acoustic potential for the Kirchhoff Green's function can be shown to be the average of those for the Huygen and Radiating Dipole functions. This conclusion may be seen quite clearly from the graphs in Figs. 5.8 and 5.9 of the preceding chapter.

Note that the symbol b in the previous chapter has been changed for the general space coordinate, r . The reason for this will become clear later.

It follows from equation (6.4) that any partial derivative of ϕ_K will also be the average of those of ϕ_H and ϕ_{RD} . The advantage of this conclusion for the present chapter will be seen later.

Partial derivatives of any of these functions may be found with respect to the space coordinates, r and z , by differentiating under the integral sign. This is facilitated by having arranged that the integration is with respect to ψ , which is not a function of r or z , and that

the limits are constant, and so are also independent of the space coordinates.

Now, two components of the particle velocity can be calculated from the expressions:

$$\underline{q}_z = \hat{z} \frac{\partial \phi}{\partial z}$$

$$\underline{q}_r = \hat{r} \frac{\partial \phi}{\partial r}$$

where \underline{q}_z and \underline{q}_r are the z and r components of the particle velocity, \hat{z} and \hat{r} being unit vectors in those respective directions.

In the forms shown, ϕ_H and ϕ_{RD} can be partially differentiated before integration to yield the appropriate results. ϕ_K could also be differentiated, but it is easier just to take an average of the other two derivatives. The differentiation will only be shown for the Radiating Dipole, as it is quite a lengthy process.

$$\text{Now } \phi_{RD} = e^{-jkz} + \frac{1}{\pi} \int_0^\pi e^{-jks} \frac{z}{s} \left(\frac{a \cos \psi - a^2}{a^2 + r^2 - 2ar \cos \psi} \right) d\psi$$

$$\therefore \frac{\partial \phi_{RD}}{\partial r} = \frac{1}{\pi} \frac{\partial}{\partial r} \left\{ \int_0^\pi e^{-jks} \frac{z}{s} \left(\frac{a \cos \psi - a^2}{a^2 + r^2 - 2ar \cos \psi} \right) d\psi \right\}$$

$$\text{Now } \frac{\partial s}{\partial r} = \frac{r - a \cos \psi}{s}$$

$$\text{as } s^2 = a^2 + z^2 + r^2 - 2ar \cos \psi$$

$$\text{and } \frac{\partial}{\partial r} \left(\frac{a \cos \psi - a^2}{a^2 + r^2 - 2ar \cos \psi} \right) = \frac{a(2ar - a^2 \cos \psi - r^2 \cos \psi)}{(a^2 + r^2 - 2ar \cos \psi)^2}$$

$$= \frac{a\{(a \cos \psi - r)(r \cos \psi - a) + ar \sin^2 \psi\}}{(a^2 + r^2 - 2ar \cos \psi)^2}$$

$$\therefore \underline{q}_r = \hat{r} \frac{\partial \phi_{RD}}{\partial r}$$

$$= \frac{1}{\pi} \int_0^\pi e^{-jks} \frac{z}{s} \frac{a}{s^2 - z^2} \left\{ \frac{ar \sin^2 \psi}{s^2 - z^2} + (a \cos \psi - r)(r \cos \psi - a) \left(\frac{jk}{s} + \frac{2-z^2/s^2}{s^2 - z^2} \right) \right\} d\psi$$

(6.5)

This integral can easily be split into two real and two imaginary functions which, although they may appear clumsy, are readily handled by procedure calls in the computer program.

One thing to note is that \underline{q}_r is zero at $z = 0$ for the Radiating Dipole, and thus all components of the particle velocity are normal to the transducer at the disc face. The r component of the particle velocity for the Huygen function is:

$$\underline{q}_r = \hat{r} \frac{\partial \phi_H}{\partial r}$$

$$= \frac{1}{\pi} \int_0^\pi e^{-jks} \frac{a}{s^2 - z^2} \left\{ \frac{ar \sin^2 \psi}{s^2 - z^2} + (a \cos \psi - r)(r \cos \psi - a) \left(-\frac{jk}{s} + \frac{1}{s^2 - z^2} \right) \right\} d\psi \quad (6.6)$$

Thus it can be shown that for the Huygen function (and hence that of the Kirchhoff) the r component of particle velocity is not zero across the disc face (i.e. $z = 0$). This means that the resultant particle velocity will not necessarily be normal to the disc face at all times, as it will be changing its direction and magnitude, as explained later.

By a similar process, \underline{q}_z for the Radiating Dipole is:

$$\underline{q}_z = \hat{z} \frac{\partial \phi_{RD}}{\partial z} = -jke^{-jkz} + \frac{1}{\pi} \int_0^\pi \frac{e^{-jks}}{s} \left(\frac{a \cos \psi - a^2}{a^2 + r^2 - 2ar \cos \psi} \right) \left(-\frac{jkz^2}{s} + 1 - \frac{z^2}{s^2} \right) d\psi \quad (6.7)$$

The term $-jke^{-jkz}$ is added only across the disc face. The value of \underline{q}_z at $z = 0$ for value of r across the disc face is not constant (Fig. 6.1) as the term (+1) in the integral causes a slight change to the main term $-jke^{-jkz}$, which is in fact $-jk$ for $z = 0$.

\underline{q}_z for the Huygen function is given by:

$$\underline{q}_z = \hat{z} \frac{\partial \phi_H}{\partial z} = -jke^{-jkz} + \frac{1}{\pi} \int_0^\pi \frac{e^{-jks}}{s} \frac{z}{s} \left(\frac{a \cos \psi - a^2}{a^2 + r^2 - 2ar \cos \psi} \right) d\psi \quad (6.8)$$

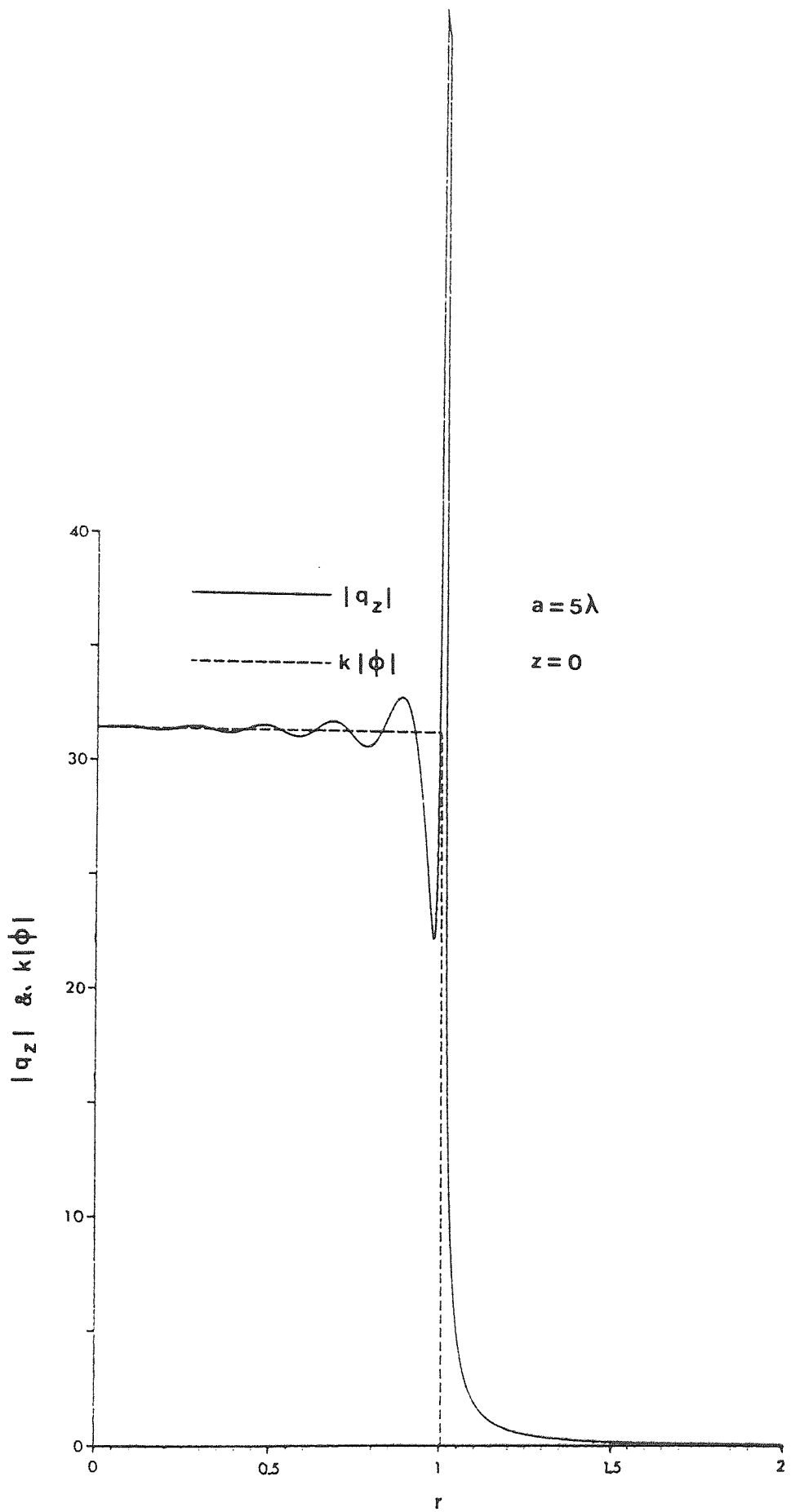


FIG.6.1 Cross Plot of Radiating Dipole Particle Velocity

If this equation is compared with equation (6.3), then for the Huygen function:

$$\underline{q}_z = \hat{z} \frac{\partial \phi_H}{\partial z} = - \hat{z} j k \phi_{RD}$$

Thus \underline{q}_z is constant across the disc face of a Huygen transducer, which is in accordance with the boundary conditions already stated (see Figs. 4.2 and 5.9).

6.2 Consideration of Resultant Particle Velocity

It has been realised that the ratio of the real parts of the velocity components \underline{q}_r and \underline{q}_z is not equal to the ratio of the imaginary parts, for a general point (r,z) in the field. It follows from this that the resultant vector

$$\underline{q} = \underline{q}_r + \underline{q}_z$$

is not in a constant direction in space. Investigation shows \underline{q} to be an elliptic vector, rotating and changing its magnitude cyclically with time. This is seen as follows:

If $\underline{q}_z = RQZ + j IQZ$, this can be written as

$$= A e^{j\alpha}$$

Multiplying by $e^{-j\omega t}$

$$\underline{q}_z(r,z,t) = A e^{j\alpha} e^{-j\omega t} = A e^{-j(\omega t - \alpha)}$$

Similarly, $\underline{q}_r(r,z,t) = B e^{-j(\omega t - \beta)}$

Now, if t is set to zero by arranging that \underline{q}_r is in phase with ϕ , i.e.

$\underline{q}_r = B e^{-j\omega t}$, \underline{q}_z will be out of phase by $(\alpha - \beta)$, i.e.

$\underline{q}_z = A e^{-j[\omega t - (\alpha - \beta)]}$, or vice versa.

This type of motion will cause the resultant velocity to describe the locus of an ellipse, and can be defined by the direction and magnitude of its major and minor axes. (Fig. 6.2).

The angle γ which defines this locus may be found in one of the two following ways:

$$1) \text{ Let } \underline{q}_z = A e^{j\alpha}$$

$$\underline{q}_r = B e^{j\beta}$$

Now, as stated before, when $\underline{q}_z = A e^{-j\omega t}$,

$$\underline{q}_r = B e^{-j\{\omega t + (\alpha - \beta)\}}$$

Let $\epsilon = \text{phase angle} = \alpha - \beta$

$$\text{and } \underline{q}_z = A \cos \omega t = x \quad (6.9)$$

$$\underline{q}_r = B \cos(\omega t + \epsilon) = y \quad (6.10)$$

From (6.9), $\cos \omega t = \frac{x}{A}$

Substituting into (6.10)

$$y = B(\cos \omega t \cos \epsilon - \sin \omega t \sin \epsilon)$$

$$= B \left(\frac{x}{A} \cos \epsilon - \sqrt{1 - \frac{x^2}{A^2}} \sin \epsilon \right)$$

$$\therefore y - \frac{Bx}{A} \cos \epsilon = -B \sqrt{1 - \frac{x^2}{A^2}} \sin \epsilon$$

Squaring both sides:

$$y^2 - \frac{2B}{A} xy \cos \epsilon + \frac{B^2 x^2}{A^2} \cos^2 \epsilon = B^2 \left(1 - \frac{x^2}{A^2} \right) \sin^2 \epsilon$$

$$\therefore A^2 y^2 - 2ABxy \cos \epsilon + B^2 x^2 - A^2 B^2 \sin^2 \epsilon = 0 \quad (6.11)$$

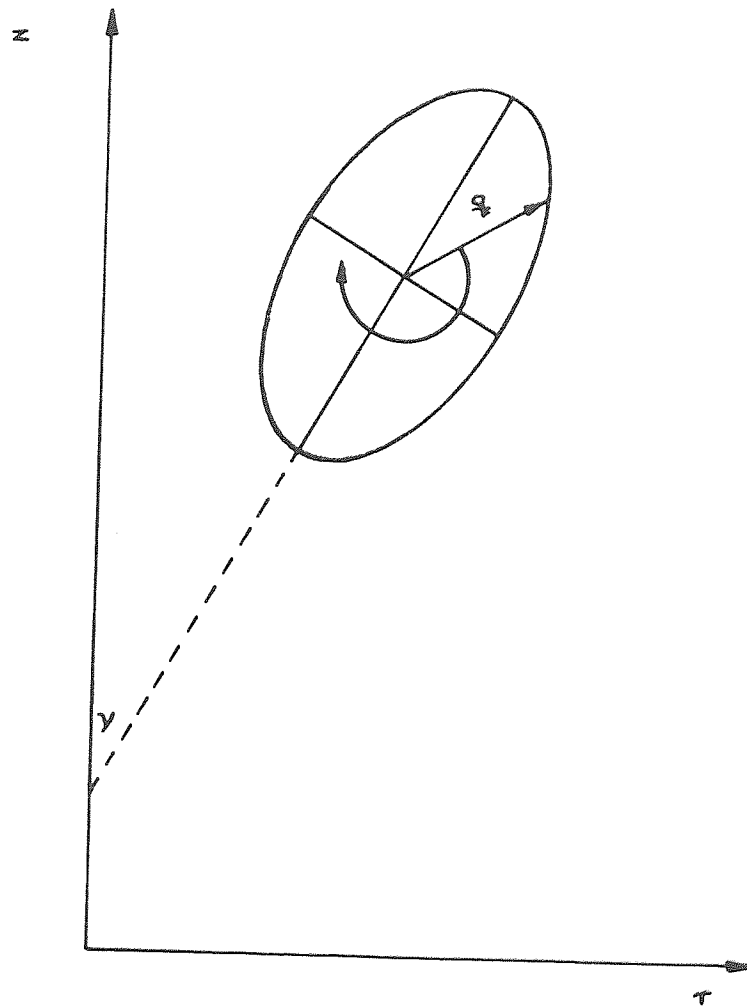


FIG.6.2 Elliptic Nature of Resultant Particle Velocity

1) continued

This is the equation of an ellipse, and is of the form:

$$ay^2 + 2hxy + bx^2 + c = 0 \quad (6.12)$$

where $a = A^2$

$$b = B^2$$

$$h = Ab \cos \epsilon \quad (6.13)$$

$$c = A^2 B^2 \sin^2 \epsilon$$

If we rotate the axes of such an ellipse from x and y to X and Y by the usual formulae:

$$x = X \cos \gamma - Y \sin \gamma,$$

$$y = X \sin \gamma + Y \cos \gamma,$$

we obtain, from substitution in equation (6.12)

$$\begin{aligned} & a(X^2 \cos^2 \gamma - 2XY \sin \gamma \cos \gamma + Y^2 \sin^2 \gamma) \\ & + 2hXY(\cos^2 \gamma - \sin^2 \gamma) + 2h(X^2 - Y^2) \sin \gamma \cos \gamma \\ & + b(X^2 \sin^2 \gamma + 2XY \sin \gamma \cos \gamma + Y \cos^2 \gamma) = 0 \end{aligned}$$

For this equation to be an ellipse, the terms in XY must vanish, therefore:

$$(-2a + 2b) \sin \gamma \cos \gamma + 2h(\cos^2 \gamma - \sin^2 \gamma) = 0$$

$$\therefore (b - a) \sin 2\gamma = -2h \cos 2\gamma$$

$$\therefore \tan 2\gamma = \frac{2h}{a - b} \quad (6.14)$$

Substituting values from equations (6.13),

$$\tan 2\gamma = \frac{2AB \cos \epsilon}{A^2 - B^2} \quad (6.15)$$

Now, let

$$\underline{q}_z = Ae^{j\alpha} = RQZ + j IQZ \quad (6.16)$$

$$\underline{q}_r = Be^{j\beta} = RQR + j IQR \quad (6.17)$$

where RQZ and RQR are the real parts of \underline{q}_z and \underline{q}_r respectively, IQZ and IQR being their respective imaginary parts. This type

1) continued

of labelling has been adopted to signify results from computation and to avoid confusion in later stages. Thus the terms in capital letters, i.e. RQZ, RQR, IQZ, IQR, can be computed.

∴ from (6.16) and (6.17)

$$A = \sqrt{RQZ^2 + IQZ^2}$$

$$B = \sqrt{RQR^2 + IQR^2}$$

$$\alpha = \tan^{-1} \left\{ \frac{IQR}{RQR} \right\}$$

$$\beta = \tan^{-1} \left\{ \frac{IQZ}{RQZ} \right\}$$

Substituting these into (6.15) yields:

$$\tan 2\gamma = \frac{2\sqrt{RQZ^2 + IQZ^2} \sqrt{RQR^2 + IQR^2} \cos \left\{ \tan^{-1} \left\{ \frac{IQR}{RQR} \right\} \tan^{-1} \left\{ \frac{IQZ}{RQZ} \right\} \right\}}{(RQZ^2 + IQZ^2) - (RQR^2 + IQR^2)} \quad (6.18)$$

Now, $\cos(\alpha - \beta) = \cos\alpha\cos\beta - \sin\alpha\sin\beta$

$$\begin{aligned} \therefore \cos(\alpha - \beta) &= \frac{RQZ}{\sqrt{RQZ^2 + IQZ^2}} \cdot \frac{RQR}{\sqrt{RQR^2 + IQR^2}} \\ &+ \frac{IQZ}{\sqrt{RQZ^2 + IQZ^2}} \cdot \frac{IQR}{\sqrt{RQR^2 + IQR^2}} \end{aligned} \quad (6.19)$$

Substituting (6.19) into (6.18):

$$\therefore \tan 2\gamma = \frac{2(RQZ \cdot RQR - IQZ \cdot IQR)}{(RQZ^2 + IQZ^2) - (RQR^2 + IQR^2)} \quad (6.20)$$

All of the terms on the R.H.S. of equation (6.20) can be readily computed from the particle velocity functions for both the Huygen and Radiating Dipole functions, and hence also for that of the Kirchhoff.

- 2) The second method achieves the same result with simpler mathematics, by differentiating $|Q_\gamma^2|$, and equating to zero to find its maximum or minimum value.

As before,

$$\underline{q}_r = RQR + j IQR$$

$$\underline{q}_z = RQZ + j IQZ$$

$$\text{Now, } \underline{q} = \underline{q}_r + \underline{q}_z$$

The magnitude of the resultant particle velocity vector \underline{q} shall be called Q_γ , and is given by

$$\begin{aligned} Q_\gamma &= (RQZ + j IQZ)\cos\gamma + (RQR + j IQR)\sin\gamma \\ &= (RQZ\cos\gamma + RQR\sin\gamma) + j(IQZ\cos\gamma + IQR\sin\gamma) \end{aligned}$$

$$\begin{aligned} \therefore |Q_\gamma^2| &= RQZ^2\cos^2\gamma + 2RQZ.RQR\sin\gamma\cos\gamma + RQR^2\sin^2\gamma \\ &\quad + IQZ^2\cos^2\gamma + 2IQZ.IQR\sin\gamma\cos\gamma + IQR^2\sin^2\gamma \end{aligned} \quad (6.21)$$

For the angle γ to be along the major axis of the ellipse

$$\frac{d(|Q_\gamma^2|)}{d\gamma} = 0$$

i.e. $|Q_\gamma^2|$ is a maximum. Therefore, differentiating equation (6.21) with respect to γ and equating to zero:

$$\begin{aligned} &-2RQZ^2\sin\gamma\cos\gamma + 2RQZ.RQR(\cos^2\gamma - \sin^2\gamma) \\ &+ 2RQR^2\sin\gamma\cos\gamma - 2IQZ^2\sin\gamma\cos\gamma \\ &+ 2IQZ.IQR(\cos^2\gamma - \sin^2\gamma) + 2IQR^2\sin\gamma\cos\gamma = 0 \end{aligned}$$

Rearranging,

$$[(RQR^2 + IQR^2) - (RQZ^2 + IQZ^2)]\sin 2\gamma + 2(RQZ.RQR + IQZ.IQR)\cos 2\gamma = 0$$

$$\therefore \tan 2\gamma = \frac{2(RQZ.RQR + IQZ.IQR)}{(RQZ^2 + IQZ^2) - (RQR^2 + IQR^2)} \quad (6.22)$$

which is the same result as equation (6.20).

The magnitudes of the semi-major and semi-minor axes can be found by direct inspection of Fig. 6.2.

$$\begin{aligned} \text{Semi-major axis} &= |\underline{q}_z| \text{Cos}\gamma + |\underline{q}_r| \text{Sin}\gamma \\ &= (\text{RQZ}^2 + \text{IQZ}^2)^{\frac{1}{2}} \text{Cos}\gamma + (\text{RQR}^2 + \text{IQR}^2)^{\frac{1}{2}} \text{Sin}\gamma \end{aligned} \quad (6.23)$$

$$\begin{aligned} \text{Semi-minor axis} &= |\underline{q}_z| \text{Sin}\gamma = |\underline{q}_r| \text{Cos}\gamma \\ &= (\text{RQZ}^2 + \text{IQZ}^2)^{\frac{1}{2}} \text{Sin}\gamma - (\text{RQR}^2 + \text{IQR}^2)^{\frac{1}{2}} \text{Cos}\gamma \end{aligned} \quad (6.24)$$

6.3 Conclusions

Both of these methods yield the same conclusion, that the resultant vector of the particle velocity at any point in space is spinning, i.e. changing its magnitude and direction as though following the locus of an ellipse. This concept is somewhat analogous to that of a spinning vector of spherically or elliptically polarised light found in optics, although it has never been realised in any of the literature in acoustic diffraction theory.

Although this is believed to be the case for particle velocity vectors in diffraction fields, this concept gives little practical information, and is difficult both to visualise and to illustrate diagrammatically.

It is, however, possible to present the information obtained from the complex components of the particle velocity, together with those of the acoustic pressure, in terms of an energy transport vector, $R_{pt}(\underline{Pq})$, and a new concept which has been called the diffraction front. It is considered that this concept contributes to the understanding of the dynamics of diffraction processes, and will be explained in greater detail in the following chapter.

One of the most important conclusions to be drawn from the theory presented in this chapter concerns the boundary conditions of the three

Green's functions being used.

The boundary conditions of the Huygen function are that the normal component of particle velocity (\underline{q}_z in the present geometry) is constant across the disc face and zero elsewhere in the $z = 0$ plane. This has been proved analytically, and has been found to be equal to $-jk$ times ϕ_{RD} , the value of the acoustic potential for the Radiating Dipole, in the $z = 0$ plane.

The values of \underline{q}_z in the $z = 0$ plane have been computed for the Radiating Dipole and are illustrated in Fig. 6.1. These should be constant across the disc face and zero elsewhere in that plane according to the boundary conditions. The results obtained are not a perfect fit, although much of the deviation is believed to be due to the computer failing to handle successfully the large number of procedure calls at the discontinuity where $r = 1$, i.e. on the edge of the transducer. This is believed to account for the large spike, but the small deviations cannot be explained to any degree of satisfaction. It is thought that if the results are not due to computer error, they are the product of a mathematical Gibb's phenomenon, or may be due to some edge effect on the un baffled transducer. Clearly, further computing is required before more certain conclusions may be drawn. The dotted line on the diagram can be considered to represent values of \underline{q}_z for the Huygen function.

From the conclusion drawn at the beginning of the chapter, it is seen that the values of \underline{q}_z for the Kirchhoff function will be an average of the two lines shown in Fig. 6.1. However, no boundary conditions involving \underline{q}_z are defined for the front face of the Kirchhoff transducer, although the back face should be perfectly absorbing, i.e. \underline{q}_z should be zero. To ascertain the value of \underline{q}_z across this back face requires the consideration of the values of \underline{q}_z on the back faces of the other two types of transducer.

An immediate problem arises in the case of the Huygen function. This is that the postulates of the original Huygen theory (Coulson and Jeffrey, 1977) involve the consideration of a plane wave being diffracted through an aperture, the surface integral being taken over a semi-infinite hemisphere. This clearly does not allow for any negative values of z , and indeed, inspection at the limit of z negative of the expression for \underline{q}_z (equation 6.8) yields the same result as for z positive. However, consideration of the practical conditions of a Huygen transducer show that the directions of particle velocity on either face should be opposing, and hence the values of \underline{q}_z on the back face are 180° out of phase, and should be -1 times the values on the front face.

This problem does not arise in the case of the Radiating Dipole, as no such discontinuity appears at $z = 0$, and hence the values of \underline{q}_z are essentially the same on either face, which is in keeping with the practical considerations of the operation of a sheet of dipoles.

Thus it may be seen that the values of \underline{q}_z across the face of a transducer described by Kirchhoff boundary conditions will be the difference of the two lines shown in Fig. 6.1, which is almost zero, apart from computer artefacts.

Improvement of the results for the values of \underline{q}_z for the Radiating Dipole is required to further confirm these boundary conditions. However, the results obtained to date do show some development in the understanding of the boundary conditions of the Kirchhoff function, a subject that has been neglected in the literature.

CHAPTER 7
Diffraction Fronts

7.1 Diffraction Fronts

7.1.1 Derivation

It has been considered that a useful presentation of the information obtained about the particle velocity is given in terms of "diffraction fronts". These are defined as surfaces in which there is no net energy transfer, and which therefore must be at right angles to lines of energy flow.

A classical wavefront, over all parts of which the value of the pressure is the same at any instant, may be regarded as a special case of a diffraction front.

A diffraction front may be found by consideration of a unit vector \hat{T} tangential to its surface. It follows from the definition that

$$\int_0^{n\tau} (\underline{q} \cdot \hat{T}) P dt = 0 \quad (7.1)$$

where $n\tau$ is any number of complete cycles or periods of the wave. When P and \underline{q} are expressed as complex numbers, then the above equation is equivalent to

$$P(\underline{q} \cdot \hat{T}) = 0 + jA$$

i.e. a purely imaginary number. Alternatively, the component of \underline{q} in a diffraction front, and P , are 90° out of phase. This is analogous to the zero net energy dissipation in an ideal capacitor or inductance, in circuit theory, in which the current and voltage are 90° out of phase.

Let the results of the integrations of the functions give:

$$\begin{aligned} \underline{q}_z &= \hat{z}(RQZ + j IQZ) \\ \underline{q}_r &= \hat{r}(RQR + j IQR) \\ \phi &= (RPHI + j IPHI) \\ P &= (RP + j IP) \end{aligned} \quad (7.2)$$

Now, for a particular point in the field, one may assume that the resultant of \underline{q}_z and \underline{q}_r will give a travelling wave carrying energy normal to the diffraction front, at an angle θ , say, to the z-axis. Thus, in a direction denoted by the vector \hat{T} normal to \hat{n} , any wave which exists must be described as a standing wave, in which energy storage may occur, but no energy propagation. \hat{r} and \hat{z} are the unit vectors of the coordinate system, as shown below in Fig. 7.1.

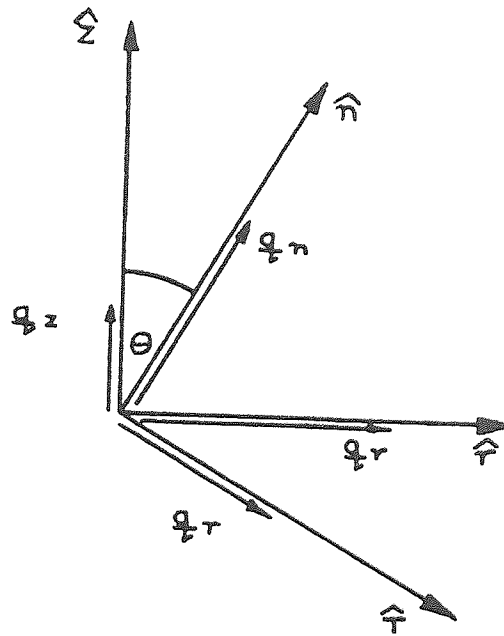


Fig. 7.1 Particle Velocity Vectors

$$\text{From Fig. 7.1, } \hat{n} = \hat{z} \cos\theta + \hat{r} \sin\theta$$

$$\hat{T} = -\hat{z} \sin\theta + \hat{r} \cos\theta$$

These equations are consistent with the formulae for rotation of axes. Resolving \underline{q}_z and \underline{q}_r onto \hat{T} , we have:

$$\begin{aligned} \underline{q}_T &= \hat{T} \left[-(RQZ + jIQZ)\sin\theta + (RQR + jIQR)\cos\theta \right] \\ &= \hat{T} \left[(RQR\cos\theta - RQZ\sin\theta) + j(IQR\cos\theta - IQZ\sin\theta) \right] \end{aligned} \quad (7.3)$$

Now, the vector $P\underline{q}_T$ must be purely imaginary, as no energy is travelling in this direction. Thus the real parts of $P\underline{q}_T$ equate to zero.

From equations (7.2) and (7.3)

$$P_{qT} = \hat{T}(RP + jIP) \left[(RQRCos\theta - RQZSin\theta) + j(IQRCos\theta - IQZSin\theta) \right] \quad (7.4)$$

Equating the real parts of (7.4) to zero:

$$RP(RQRCos\theta - RQZSin\theta) - IP(IQRCos\theta - IQZSin\theta) = 0$$

$$\therefore \frac{RQR \cos \theta - RQZ \sin \theta}{IQR \cos \theta - IQZ \sin \theta} = \frac{IP}{RP}$$

Dividing by $\cos \theta$

$$\frac{RQR - RQZ \tan \theta}{IQR - IQZ \tan \theta} = \frac{IP}{RP} \quad (7.5)$$

Hence,

$$\tan \theta = \frac{RP \cdot RQR - IP \cdot IQR}{RP \cdot RQZ - IP \cdot IQZ} \quad (7.6)$$

Now, for purposes of simpler computing, the ratio of the real and imaginary parts of the pressure in equation (7.5) may be substituted with those already calculated for the acoustic potential ϕ in the following manner:

$P = -j\omega\rho\phi$ for a particular frequency, and hence a particular ratio of a/λ .

$$\therefore P = -j\omega\rho(RPHI + IPHI) = RP + jIP$$

from equations (7.2). Equating real and imaginary parts:

$$\left. \begin{aligned} -\omega\rho \cdot RPHI &= IP \\ \omega\rho \cdot IPHI &= RP \end{aligned} \right\} \quad (7.7)$$

Dividing, $\frac{-RPHI}{IPHI} = \frac{IP}{RP}$

Substituting into equation (7.5) yields:

$$\frac{RQR - RQZ \tan \theta}{IQR - IQZ \tan \theta} = \frac{-RPHI}{IPHI}$$

Hence,

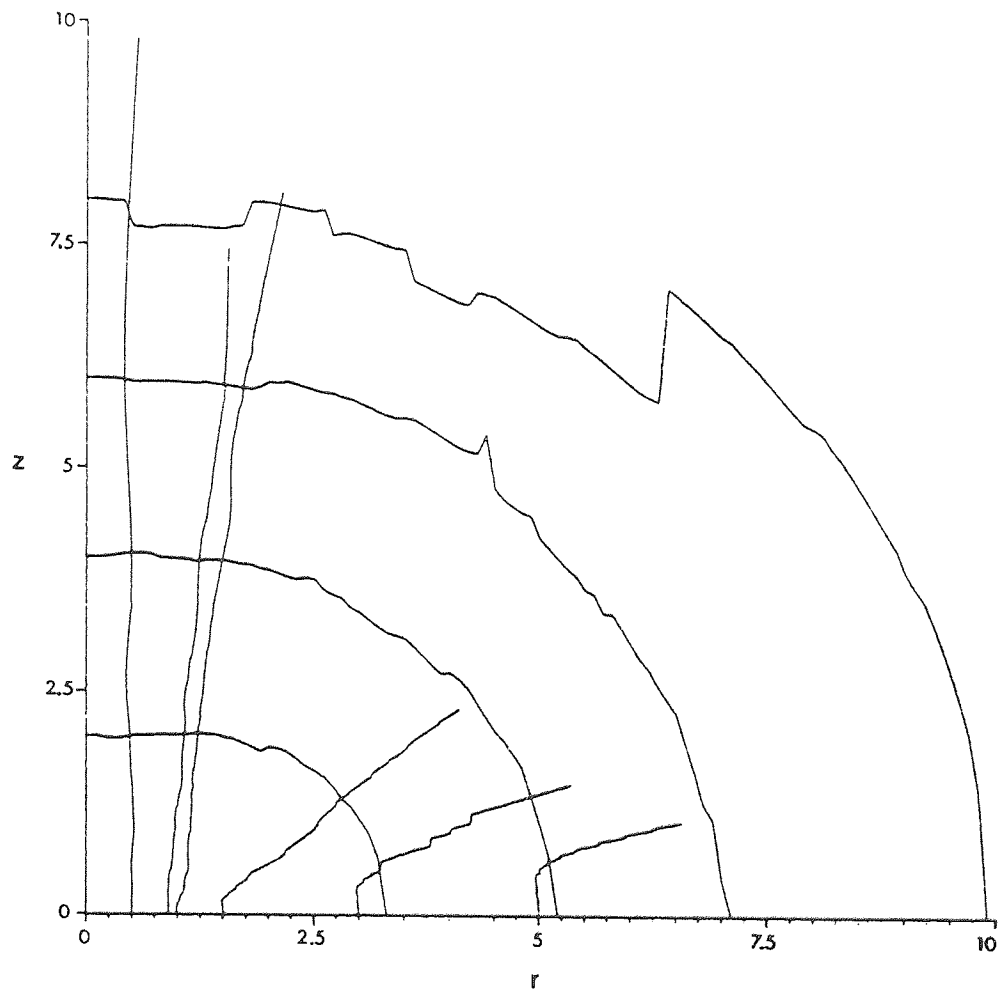
$$\tan \theta = \frac{RPHI \cdot IQR + IPHI \cdot RQR}{RPHI \cdot IQZ + IPHI \cdot RQZ} \quad (7.8)$$

Thus, θ can be evaluated from the function for ϕ without having to make a further calculation to find P , and may be illustrated graphically by using a field plotting technique similar to those used for electrostatic and magnetic fields.

7.1.2 Results

Directions of energy flow are found by starting at a point in the $z = 0$ plane, and stepping small distances in r , changing z in accordance with the magnitude of $\tan \theta$. Similarly, "diffraction surfaces", in which there is no energy flow, are found by starting from a point in the $r = 0$ plane, and stepping increments in z . If the two sets of lines are plotted on the same graph, taking care to keep the scaling of the axes equal, each intersection of energy flow and diffraction front lines should be orthogonal.

A large graph (Fig. 7.2) of these lines has been made for the radiating Dipole, measuring ten units square, where one unit is the radius of the transducer. A closer inspection of the nearfield diffraction fronts (Fig. 7.3) shows the orthogonality, and also that most of the energy emitted from the transducer is initially radiated in an almost straight line. A field, the size of the three dimensional plots of ϕ already shown, was chosen and used to compare all three functions (Fig. 7.4). In all of these graphs, the energy flow lines and diffraction fronts should have both smooth lines and orthogonal intersections. This is not so because the large number of function procedures needed to be integrated by the computer (as many as sixteen in the case of the Kirchhoff function) leads to a not unreasonable error in the result, but one which is cumulative due to the field plotting technique used. A statistical field-plotting computer sub-



$$a = 5\lambda$$

FIG.7.2 Radiating Dipole Diffraction
Fronts

$$a = 5\lambda$$

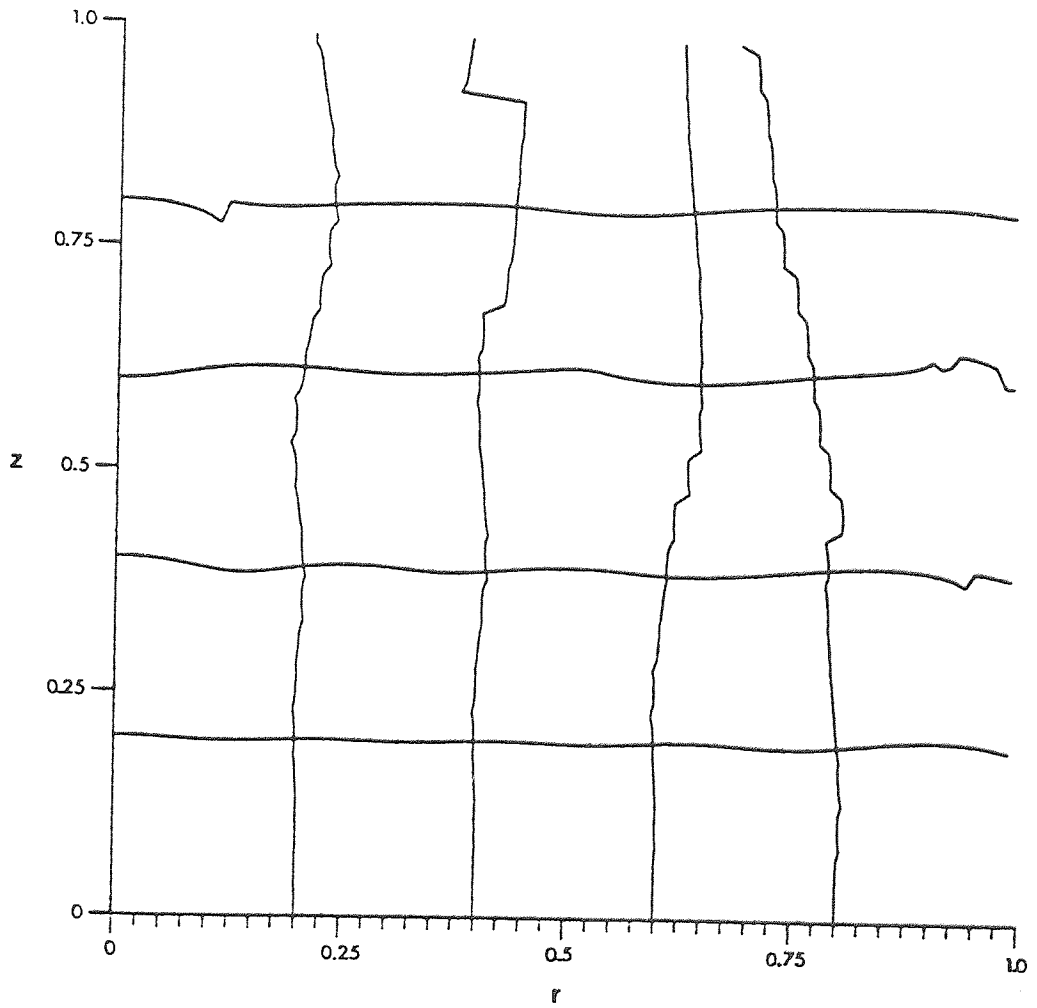


FIG.7.3 Nearfield Diffraction Fronts

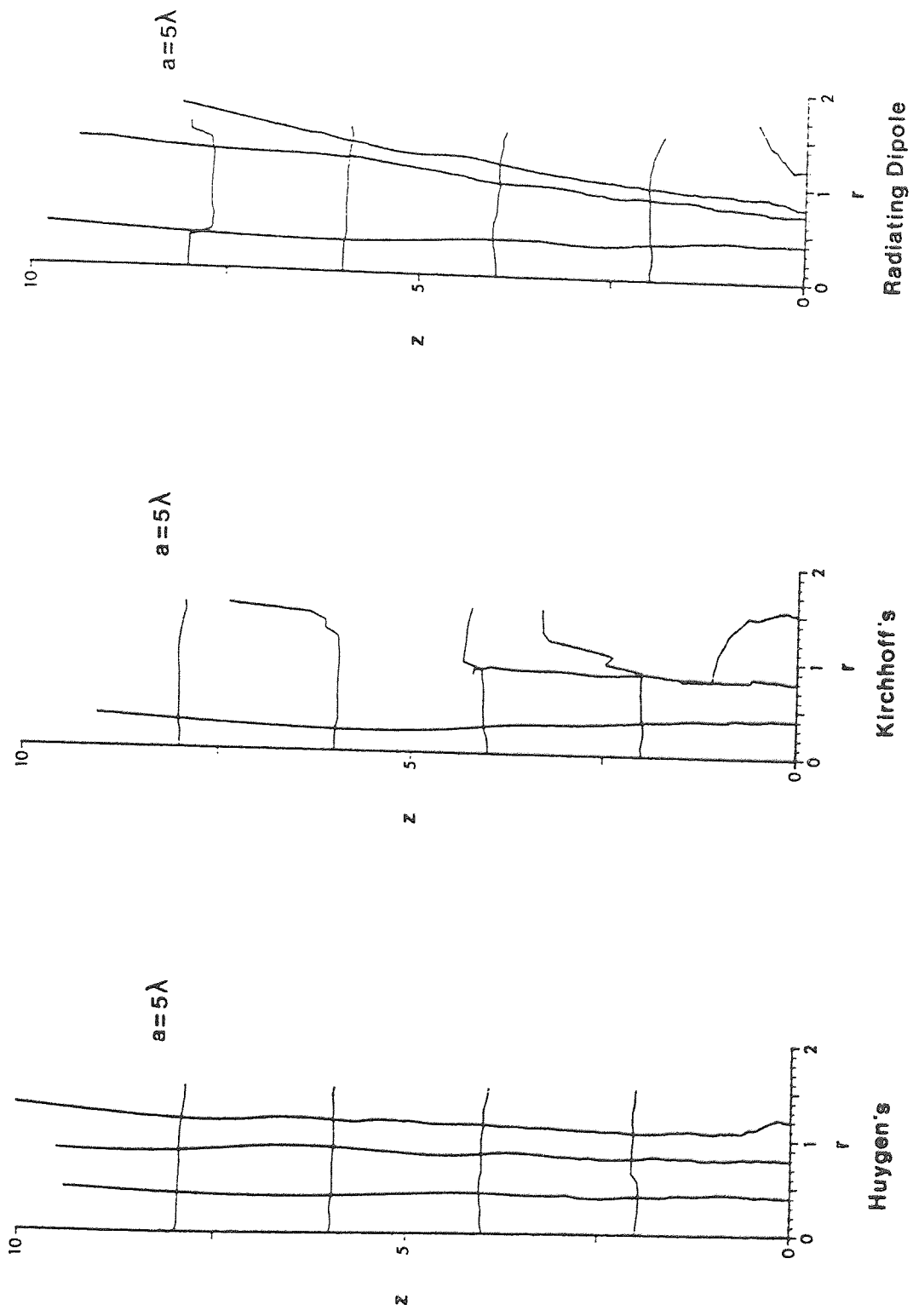


FIG. 7.4 Comparisons of Diffraction Fronts

routine package may provide better results, but this is not yet available at Aston.

7.2 Energy Intensity

7.2.1 Derivation

The graphs of diffraction fronts and energy flow lines only indicate the direction of energy flow, but no information can be given on the same graph about the magnitude of energy in that line without making the illustration too complex. The following method has been developed to give a value of the magnitude of energy anywhere in the diffraction field.

From equation (7.4):

$$\begin{aligned} \therefore P_{\underline{q}_T} &= \hat{T}(RP + jIP) \left[(RQR + jIPR)\cos\theta - (RQZ + jIQZ)\sin\theta \right] \\ &= \hat{T} \left[(RP.RQR - IP.IQR) + j(RP.IQR + IP.RQR) \right] \cos\theta \\ &\quad - \hat{T} \left[(RP.RQZ - IP.IQZ) + j(RP.IQZ + IP.RQZ) \right] \sin\theta \end{aligned}$$

θ is found such that the real part of $P_{\underline{q}_T}$ is zero as in equation (7.4) i.e.:

$$(RP.RQR - IP.IQR)\cos\theta - (RP.RQZ - IP.IQZ)\sin\theta = 0 \quad (7.9)$$

$$\text{Hence, } \tan\theta = \frac{RP.RQR - IP.IQR}{RP.RQZ - IP.IQZ}$$

This agrees with equation (7.6), which is now shown to be an alternative method to find the direction of \underline{Pq} . Now, the energy transfer rate is the real part of $P_{\underline{q}_n}$, which is given by

$$\begin{aligned} P_{\underline{q}_n} &= P(\underline{q}_r \sin\theta + \underline{q}_z \cos\theta) \\ &= \hat{n}(RP + jIP) \left[(RQR + jIQR)\sin\theta + (RQZ + jIQZ)\cos\theta \right] \\ &= \hat{n} \left[(RP.RQR - IP.IQR) + j(RP.IQR + IP.RQR) \right] \sin\theta \\ &\quad - \hat{n} \left[(RP.RQZ - IP.IQZ) + j(RP.IQZ + IP.RQZ) \right] \cos\theta \end{aligned}$$

Let the energy transfer rate = I watts m^{-2}

$$\therefore I = (RP.RQR - IP.IQR)\sin\theta - (RP.RQZ - IP.IQZ)\cos\theta \quad (7.10)$$

and equation (7.9)

$$0 = (RP.RQR - IP.IQR)\cos\theta + (RP.RQZ - IP.IQZ)\sin\theta \quad (7.9)$$

$$\text{Let } (RP.RQR - IP.IQR) = G \quad (7.11)$$

and

$$(RP.RQZ - IP.IQZ) = H \quad (7.12)$$

Therefore, squaring equations (7.9) and (7.10):

$$\left. \begin{aligned} I^2 &= G^2\sin^2\theta + H^2\cos^2\theta - 2GHSin\theta\cos\theta \\ 0 &= G^2\cos^2\theta + H^2\sin^2\theta + 2GHSin\theta\cos\theta \end{aligned} \right\} \quad (7.13)$$

$$\therefore I^2 = G^2 + H^2$$

$$\begin{aligned} \therefore |I| &= \sqrt{G^2 + H^2} \\ &= \left[(RP.RQR - IP.IQR)^2 + (RP.RQZ - IP.IQZ)^2 \right]^{\frac{1}{2}} \end{aligned} \quad (7.14)$$

but, from equations (7.7)

$$RP = \omega_p IPHI$$

$$IP = -\omega_p RPHI$$

and substituting these into equation (7.14) gives

$$|I| = \omega_p \left[(RPHI.IQR + IPHI.RQR)^2 + (RPHI.IQZ + IPHI.RQZ)^2 \right]^{\frac{1}{2}} \quad (7.15)$$

7.2.2 Results

For simpler computing, ω_p has been absorbed into the arbitrary constant A . Thus, the modulus of the energy transfer rate can be found anywhere in the diffraction field. Three dimensional plots of these are shown in Fig. 7.5, 7.6 and 7.7.

From these results, it can be seen that the Huygen function shows a definite cut-off for all points in the field not directly in line with the transducer. As the Kirchhoff function is partly dependent on the Huygen function, it is not surprising that this also displays

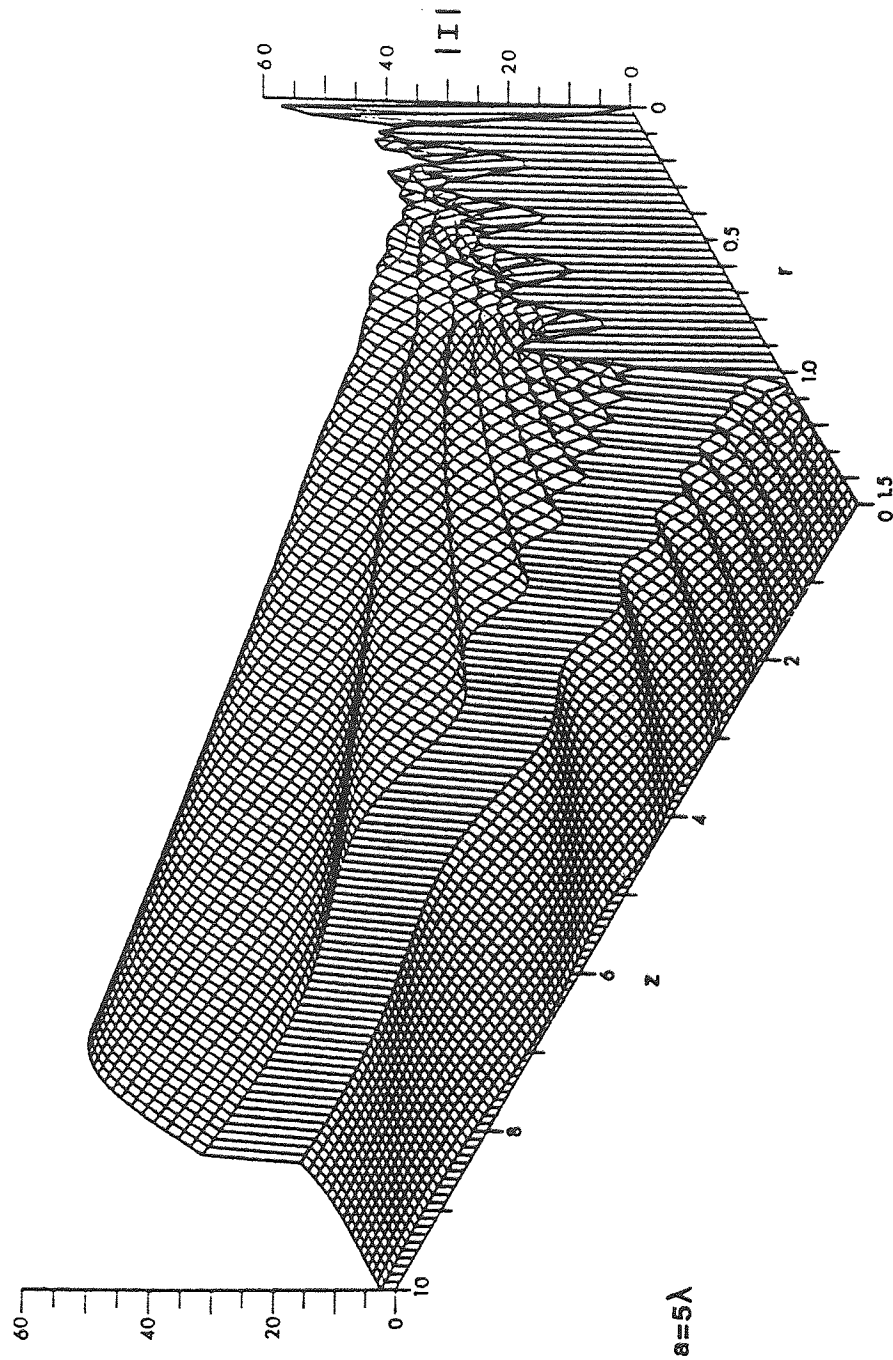


Fig 7.5 Huygen Diffraction Energy Field

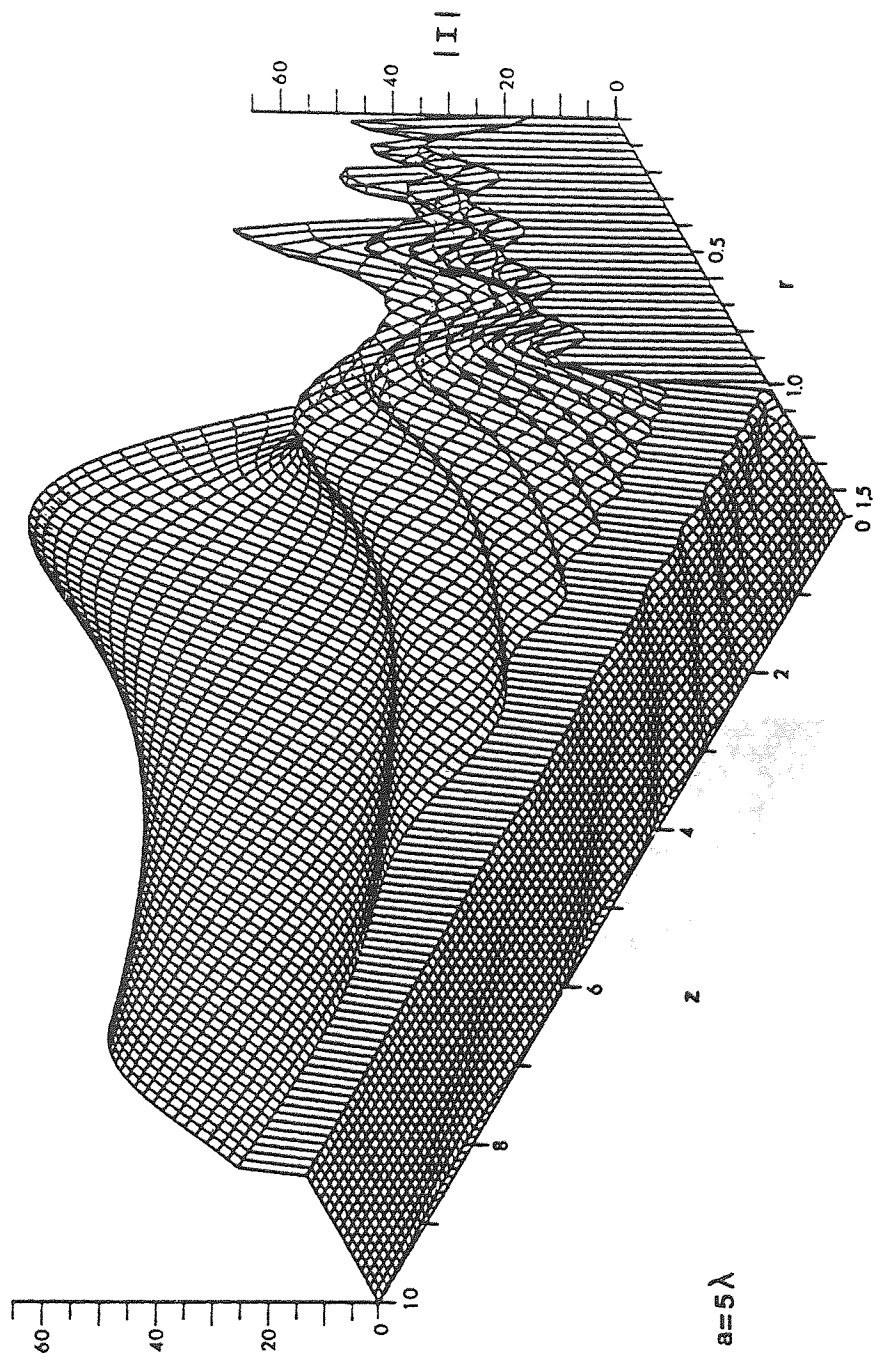


Fig 7.6 Kirchhoff Diffraction Energy Field

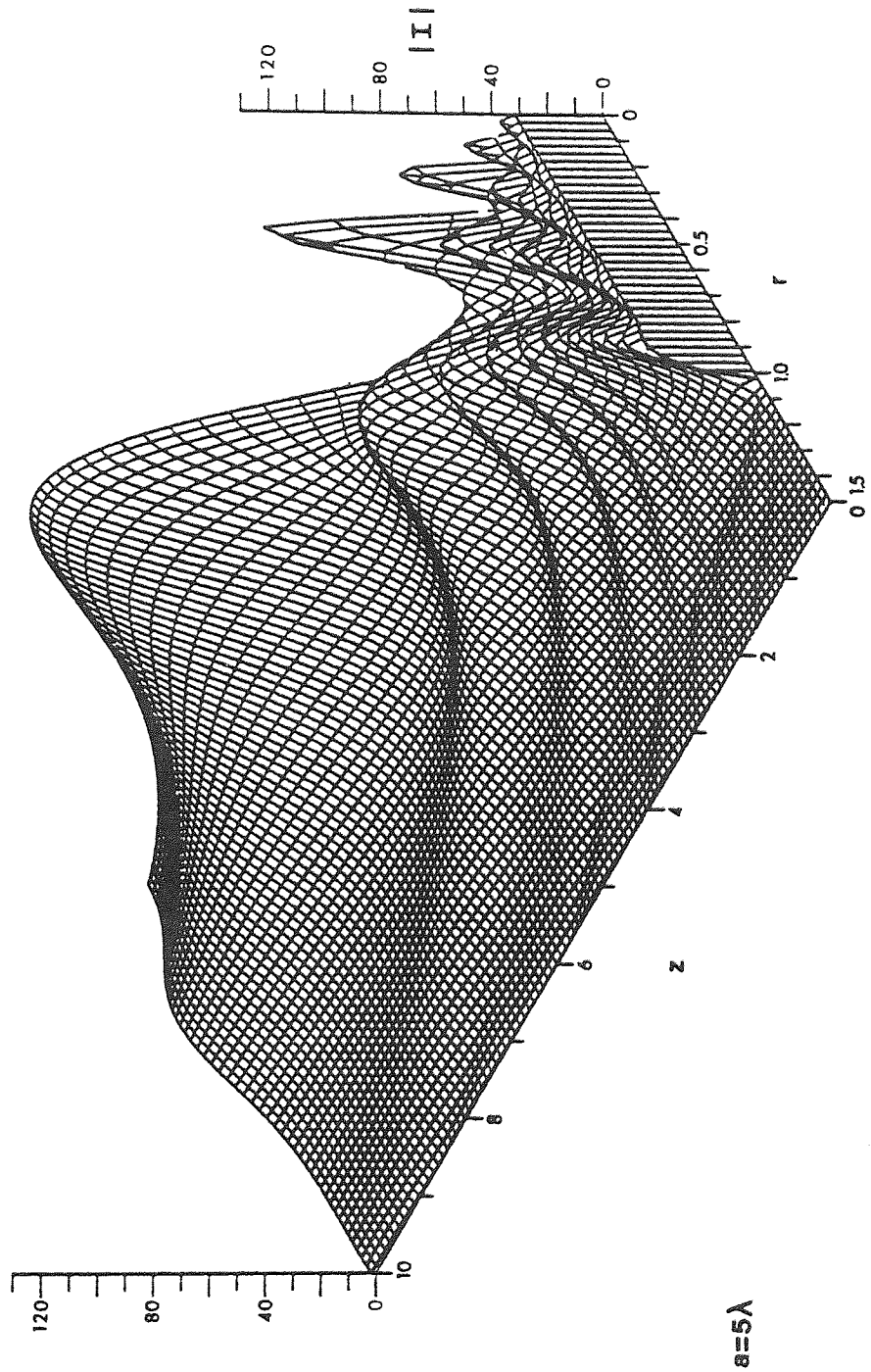


Fig 7.7 Radiating Dipole Diffraction Energy Field

a similar feature. The Radiating Dipole function, however, does not display such a radical cut-off, which seems to be in keeping both with its boundary conditions, and the results of its diffraction front graph. Moreover, it can be shown from the alternative view shown in Fig. 7.8 that the final maximum on the z-axis occurs at 5 units, which corresponds to a^2/λ . The energy then appears to begin to distribute itself in a beam pattern which is indicative of the beginning of the far-field region.

7.3 Corollary of Diffraction Front and Intensity Theory

The general expression for intensity has been written as:

$$\underline{I} = \frac{1}{T} \int_0^T P \underline{q} \, dt \quad (7.16)$$

Now, $P = \nabla \phi$

and $\underline{q} = \rho \frac{\partial \phi}{\partial t}$

Therefore (7.16) may be written as

$$\underline{I} = \frac{\rho}{T} \int_0^T \nabla \phi \frac{\partial \phi}{\partial t} \, dt \quad (7.17)$$

where $\nabla^2 \phi + k^2 \phi = 0$ from the d'Alembertian.

It is accepted that, for a wave equation in which there is no mechanism for attenuation, i.e. the d'Alembertian, then if \underline{I} is the intensity vector, the divergence of \underline{I} is zero. This implies that there are no energy sources in the field. It will now be shown that this is the case for the function that we have used.

Hence, from (7.17)

$$\nabla \cdot \underline{I} = \frac{\rho}{T} \int_0^T \nabla \cdot \left(\nabla \phi \frac{\partial \phi}{\partial t} \right) \, dt$$

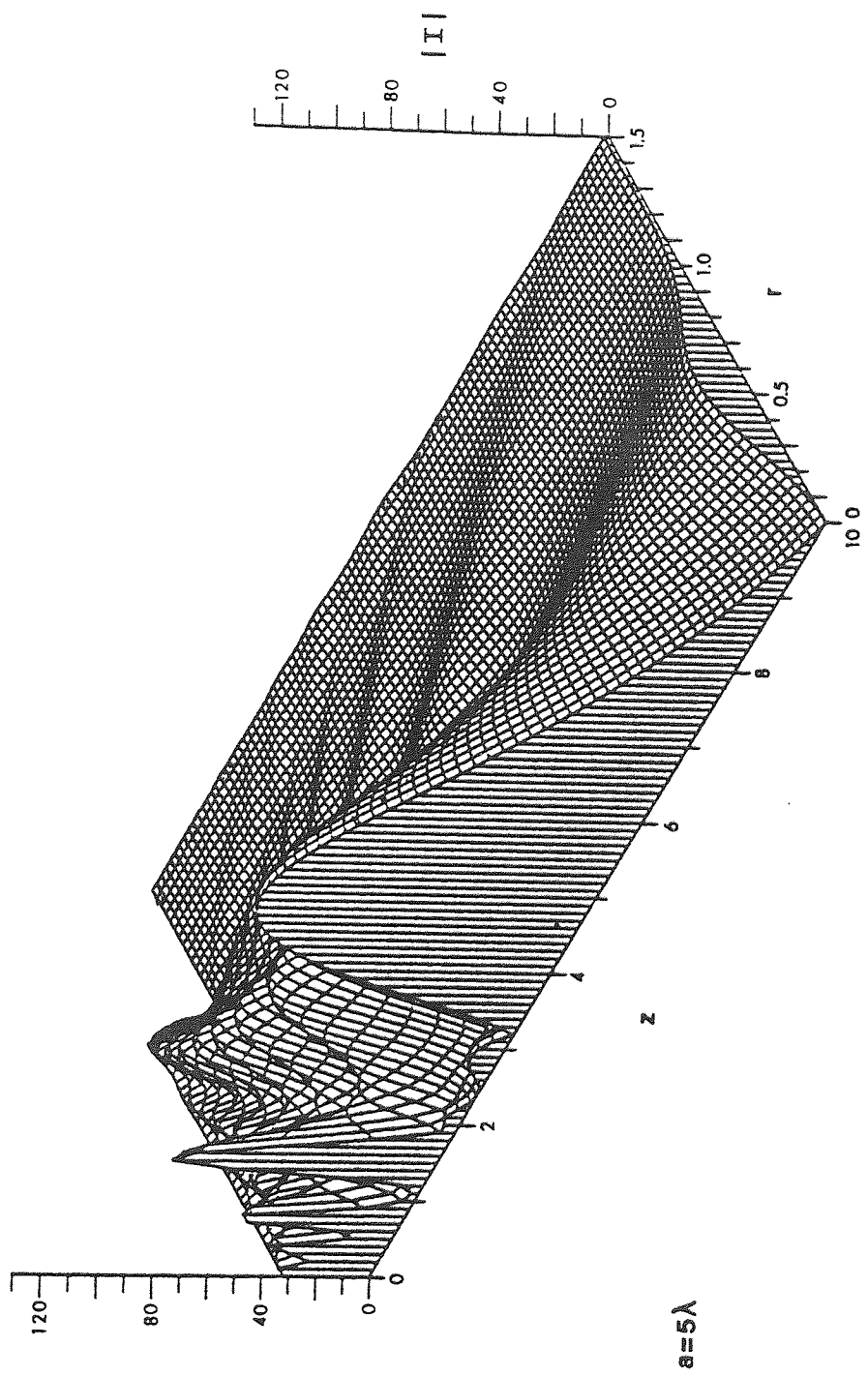


Fig 7.8 Alternative View of Radiating Dipole Energy Field

$$= \frac{\rho}{T} \int_0^T \left(\nabla \cdot \nabla \phi \frac{\partial \phi}{\partial t} \right) + \left(\nabla \phi \cdot \nabla \frac{\partial \phi}{\partial t} \right) dt$$

Separating,

$$\begin{aligned} \nabla \cdot \underline{I} &= \frac{\rho}{T} \int_0^T \nabla \cdot \nabla \phi \frac{\partial \phi}{\partial t} dt + \frac{\rho}{T} \int_0^T \nabla \phi \cdot \nabla \frac{\partial \phi}{\partial t} dt \\ &= \frac{\rho}{T} \int_0^T \nabla^2 \phi \frac{\partial \phi}{\partial t} dt + \frac{\rho}{T} \int_0^T \frac{\partial}{\partial t} \frac{(\nabla \phi)^2}{2} dt \end{aligned}$$

Changing limits and integration variable

$$\nabla \cdot \underline{I} = \frac{\rho}{T} \int_{\phi_0}^{\phi_T} \nabla^2 \phi d\phi + \frac{\rho}{T} \int_{\phi_0}^{\phi_T} \frac{1}{2} d(\nabla \phi)^2$$

$$\nabla \cdot \underline{I} = \frac{\rho}{T} \int_{\phi_0}^{\phi_T} -k^2 \phi d\phi + \frac{\rho}{2T} \int_{\phi_0}^{\phi_T} d(\nabla \phi)^2$$

$$\nabla \cdot \underline{I} = \frac{\rho}{T} \left[-k^2 \frac{\phi^2}{2} \right]_{\phi_0}^{\phi_T} + \frac{\rho}{T} \left[\frac{(\nabla \phi)^2}{2} \right]_{\phi_0}^{\phi_T} \quad (7.18)$$

Now, if $\phi_T = \phi_0$, and $\nabla \phi_T = \nabla \phi_0$,

$$\text{then, } \frac{k^2}{2} (\phi_T^2 - \phi_0^2) = \frac{1}{2} \left[(\nabla \phi_T)^2 - (\nabla \phi_0)^2 \right] = 0$$

Therefore, from equation (7.18),

$$\nabla \cdot \underline{I} = 0, \text{ Q.E.D.}$$

7.4 Conclusions

The difficulty in visualising the spinning particle vector has led to the development of the diffraction front and energy intensity techniques to illustrate both the direction and magnitude of this vector. This has been achieved in a manner which is believed to provide the best practical information about diffraction fields. This technique is

both novel and unique, and hence results obtained cannot be compared with any previously published work, as none exists.

The derivation of an expression to determine the direction of the resultant particle velocity had been performed by two independent methods yielding the same result. The graphical results obtained have provided some confirmation of the original boundary conditions relating to the Green's functions used. These results are not completely satisfactory, and further work is required in either developing an alternative computer program, or adapting an existing graphical subroutine package in order to overcome the problems of plotting the diffraction fronts.

The magnitude of the resultant particle velocity has been illustrated by plotting energy intensity. The results obtained require further examination and experimental confirmation. It may be possible to investigate the conical beam shown in the intensity plots by using a thermocouple probe surrounded by a small encased volume of castor oil. This would measure the heating effect on the oil. However, such a probe may prove to be too large for the size of the field, so an alternative design may be required, or an experiment devised to work at a lower frequency, perhaps in the audio range. One of the main problems is that the experiment would be attempting to measure pressure, particle velocity and phase difference all at the same time. This problem is further compounded by the changing direction of the particle velocity resultant, but it may be possible to measure on-axis intensities, as here the vector is pointing in a constant direction.

Further investigation of the intensity may be possible using a technique developed by Hutchins (1978), and Archer-Hall and Hutchins (1979,1981) using a photoelastic layer to observe continuous-wave ultrasonic fields. The boundary conditions of the transducer used

approximate to those of the Radiating Dipole, and the results obtained show a cone of intensity.

Further work on the corollary to the diffraction theory could also be fruitful, as it is believed that a function W should exist such that: $\underline{I} = \nabla W$ where \underline{I} is the intensity vector already defined.

This function will then obey the Laplacian;

$$\nabla^2 W = 0, \text{ as } \nabla \cdot \underline{I} = 0 \text{ as proved.}$$

If W can be expressed as a complex number:

$$W = U + jV.$$

The component V will be a function to describe the energy flow lines, and U the diffraction fronts. If these functions can be found, the plotting of the energy flow lines and diffraction fronts will be greatly simplified, and the results should be more accurate. However, this could develop into a highly mathematical exercise, and is considered to be beyond the scope of the present project.

7.5 General Conclusions of Diffraction Theory

The geometrical transform presented in this thesis has widened the applications of the surface integral technique for investigation of acoustic diffraction. This is because any Green's function can be used, and the only constraints are that the transducer configuration be axisymmetrical, and the Green's function describes the boundary conditions of the transducer correctly.

A great deal of consideration has gone into various boundary condition requirements, and further work is necessary to describe those of other transducers. The results on the work of the Radiating Dipole transducer are believed to describe the conditions found in medical ultrasonography, and results of this kind have never before been calculated.

The technique has been extended to provide many new areas of discussion by examining the nature of the particle velocity anywhere in the diffraction field. The results of the diffraction front and energy intensity plots have never been obtained before, so no comparison with alternative methods is possible. Further work is obviously required to confirm these results either by experiment or alternative theory. Some of the results obtained are open to a great deal of discussion, and may lead to significant changes in both the use and understanding of acoustic diffraction.

APPENDICES

APPENDIX 1: Transmission Line Model for Attenuation in a Fluid

APPENDIX 2: Initial Bias System

APPENDIX 3: Frequency Response of Transducer Coupling

APPENDIX 4: Investigation of Computing Costs

APPENDIX 5: Publication

Appendix 1: Transmission Line Model for Attenuation in a Fluid

A.1.1 Introduction

Any mathematical model to describe ultrasonic propagation in a dispersive medium must fit available data on tissue absorption and attenuation. Goss et al (1978) show that little information is available in this area. However, some start has been made to set up a mathematical model for tissue by Leeman (1980) (and Gore and Leeman, 1977), which was presented at a conference in May 1978 at Brunel University, entitled "The Transmission and Scattering of Ultrasound in Human Tissue", under the auspices of the Institute of Acoustics.

Leeman's work takes an arbitrary and somewhat questionable choice of wave equation, and solves it after taking a Laplace transform. After taking an inverse Laplace transform, and deconvolution, the results show that a propagating pulse from a reflection in the absorbing medium consists of two components. The first of these is an undistorted replica of the incident pulse, travelling at the velocity of sound in the medium, and damped with an absorption coefficient α_0 . The second component is a time-extended "rumble" of lower frequency components, which travels slower and becomes more significant from reflections further into the medium.

The choice of wave equation is justified by fitting to empirical data for values of absorption and phase velocity (Brady et al, 1976, Carstensen and Schwan, 1959), but the fits are far from exact, especially in the case of phase velocity.

However, as Leeman admits, this model is only a tentative beginning, although it has advantages over an equivalent technique devised by Dines and Kak (1976), in that the Fourier analysis involved in the latter is avoided.

A model to describe attenuation in water is presented here, which uses the concept of a transmission line. The virtual electrical components are arranged to allow for attenuation.

(A1.1)

A.1.2 Theory

Consider the transmission line shown in Fig. A.1.1 below.

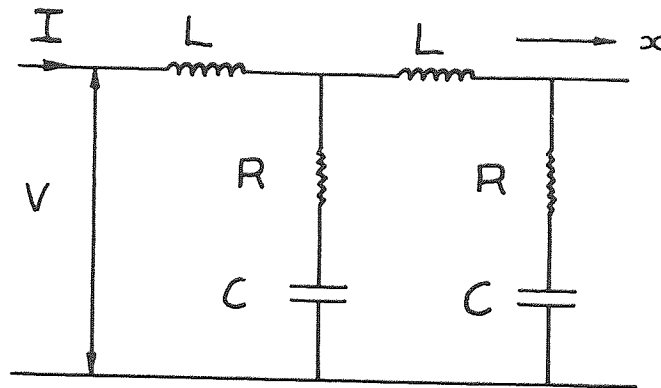


Fig. A.1.1 Transmission Line Model

Now,

$$\frac{\partial V}{\partial x} = -j\omega LI \quad \left(\text{as } j\omega \text{ is equivalent to } \frac{\partial}{\partial t} \right) \quad (\text{A1.1})$$

and,

$$\frac{\partial I}{\partial x} = \frac{-V}{R + \frac{1}{j\omega C}} = \frac{-j\omega CV}{1 + j\omega RC} \quad (\text{A1.2})$$

$$\therefore \frac{\partial I}{\partial x} = \frac{-C}{1 + \omega^2 RC} \frac{\partial V}{\partial t} - \frac{\omega^2 RC^2}{1 + \omega^2 RC} V$$

Now, from (A1.1),

$$\frac{\partial^2 V}{\partial x^2} = -L \frac{\partial}{\partial t} \frac{\partial I}{\partial x}$$

$$\therefore \frac{\partial^2 V}{\partial x^2} = \frac{LC}{1 + \omega^2 RC} \frac{\partial^2 V}{\partial t^2} + \frac{\omega^2 LRC^2}{1 + \omega^2 RC} \frac{\partial V}{\partial t} \quad (\text{A1.3})$$

This is the wave equation for the medium, where the last term allows for attenuation. This equation may also be written as:

$$\frac{\partial^2 V}{\partial x^2} = \frac{-\omega^2 L}{1 + j\omega RC} V \quad (A1.4)$$

If we now assume a solution of the form:

$$V = A e^{-(\alpha + jk')x}$$

where α is the attenuation coefficient, and k' the wave number, then

$$(\alpha + jk')^2 = \frac{-\omega^2 LC}{1 + j\omega CR} \quad \text{from (A1.4)}$$

Rearranging,

$$(\alpha^2 - k'^2 + 2j\alpha k')(1 + j\omega CR) = -\omega^2 LC \quad (A1.5)$$

Equating real and imaginary parts,

$$\alpha^2 - k'^2 - 2\alpha k' \omega CR = -\omega^2 LC \quad (A1.6)$$

$$\text{and } \alpha^2 - k'^2 + \frac{2\alpha k'}{\omega CR} = 0 \quad (A1.7)$$

Subtracting (A1.6) from (A1.7) gives:

$$2\alpha k' \left(\frac{1}{\omega CR} + \omega CR \right) = \omega^2 LC \quad (A1.10)$$

$$\therefore k' = \frac{\omega^2 LC}{2 \left(\frac{1}{\omega CR} + \omega CR \right)} \cdot \frac{1}{\alpha}$$

Let

$$A = \frac{\omega^2 LC}{2 \left(\frac{1}{\omega CR} + \omega CR \right)} \quad (A1.8)$$

$$\therefore k' = \frac{A}{\alpha}$$

Therefore, from equation (A1.7)

$$\alpha^2 - \frac{A^2}{\alpha^2} + \frac{2\alpha}{\omega CR} \cdot \frac{A}{\alpha} = 0$$

$$\therefore \alpha^4 + \frac{2A\alpha^2}{\omega CR} - A^2 = 0$$

$$\therefore \alpha^2 = \frac{-A}{\omega CR} + \sqrt{A^2 \left(\frac{1}{\omega^2 C^2 R^2} + 1 \right)} \quad (\text{A1.9})$$

The negative root of this equation may be ignored since α^2 must be positive as the attenuation coefficient α must be real.

$$\therefore \alpha^2 = \frac{-A}{\omega CR} + \frac{A}{\omega CR} \left(1 + \omega^2 C^2 R^2 \right)^{\frac{1}{2}}$$

Expanding binomially,

$$\begin{aligned} \alpha^2 &= \frac{A}{\omega CR} \left[-1 + 1 + \frac{1}{2} \omega^2 C^2 R^2 - \frac{1}{8} \omega^4 C^4 R^4 \dots \right] \\ &= \frac{A}{2} \omega CR \quad \text{for } \omega CR \ll 1 \end{aligned}$$

Substituting from (A1.8)

$$\alpha^2 = \frac{\omega^4 LC^3 k^2}{4} \cdot \frac{1}{(1 + \omega^2 C^2 R^2)}$$

$$\text{Hence } \alpha \approx \frac{\omega^2 CR}{2} \sqrt{LC} \quad (\text{A1.10})$$

i.e. α is proportional to the square of frequency as $\omega = 2\pi f$

An alternative approach provides more exact expressions for α and k' , without making the approximation that $\omega CR \ll 1$. This is achieved as follows:

$$\text{If } V = A e^{-(\alpha + jk')x}$$

$$\text{and } c_0^2 = \frac{1}{LC} \quad \text{where } c_0 = \text{velocity at } R = 0$$

then

$$(\alpha + jk')^2 = \frac{-\omega^2}{c_0^2} \cdot \frac{1}{1 + j\omega RC}$$

therefore

$$\alpha + jk' = k_0 \frac{1}{(1 + \omega^2 R^2 C^2)^{\frac{1}{4}}} e^{-j \left[\frac{\tan^{-1}(\omega RC)}{2} \right]}$$

and hence

$$\alpha = k_0 \frac{1}{(1 + \omega^2 R^2 C^2)^{\frac{1}{4}}} \sin \frac{1}{2} [\tan^{-1}(\omega RC)] \quad (A1.11)$$

$$k' = k_0 \frac{1}{(1 + \omega^2 R^2 C^2)^{\frac{1}{4}}} \cos \frac{1}{2} [\tan^{-1}(\omega RC)] \quad (A1.12)$$

where k_0 is the wave number at $R = 0$

$$\text{Now, } k' = \frac{\omega}{c'}, \text{ and } k_0 = \frac{\omega}{c_0}$$

\therefore from equation (A1.12)

$$\begin{aligned} \frac{\omega}{c'} &= \frac{\omega}{c_0} \frac{1}{(1 + \omega^2 R^2 C^2)^{\frac{1}{4}}} \cos \frac{1}{2} [\tan^{-1}(\omega RC)] \\ \therefore \frac{c'}{c_0} &= \frac{(1 + \omega^2 R^2 C^2)^{\frac{1}{4}}}{\cos \frac{1}{2} [\tan^{-1}(\omega RC)]} \end{aligned} \quad (A1.13)$$

Hence graphs can be plotted for $\frac{c'}{c_0}$ and α from the expressions (A1.11) and (A1.13), if the range of ω can be ascertained. This is achieved by limiting the value of α to less than 0.1, as the present ultrasonic systems cannot handle any greater degrees of attenuation.

A1.3 Results

The graphs of α and $\frac{c'}{c_0}$ are shown in Figs.A.1.2 and A.1.3 respectively. Both graphs are plotted with the same scale for the frequency, and all scales are linear.

As can be seen from the graphs, both α and c' increase with increasing frequency. The attenuation is almost proportional to the square of the frequency, and the velocity varies almost linearly with frequency. This is believed to be the case in pure liquids.

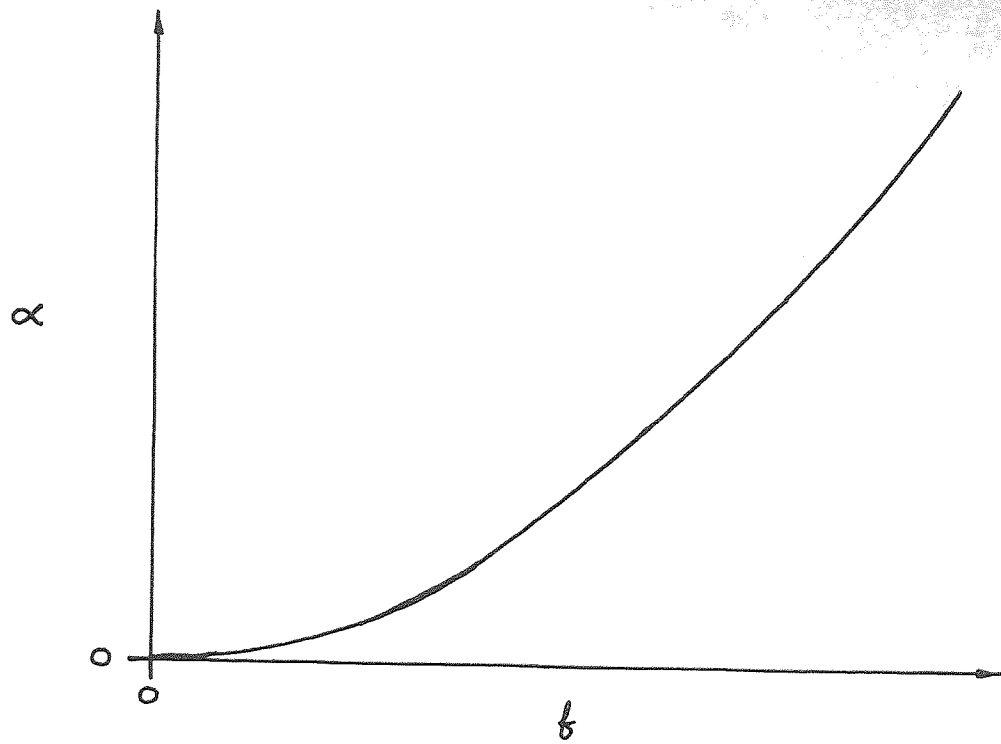


Fig. A.1.2. Graph of α vs f for Transmission Line Model

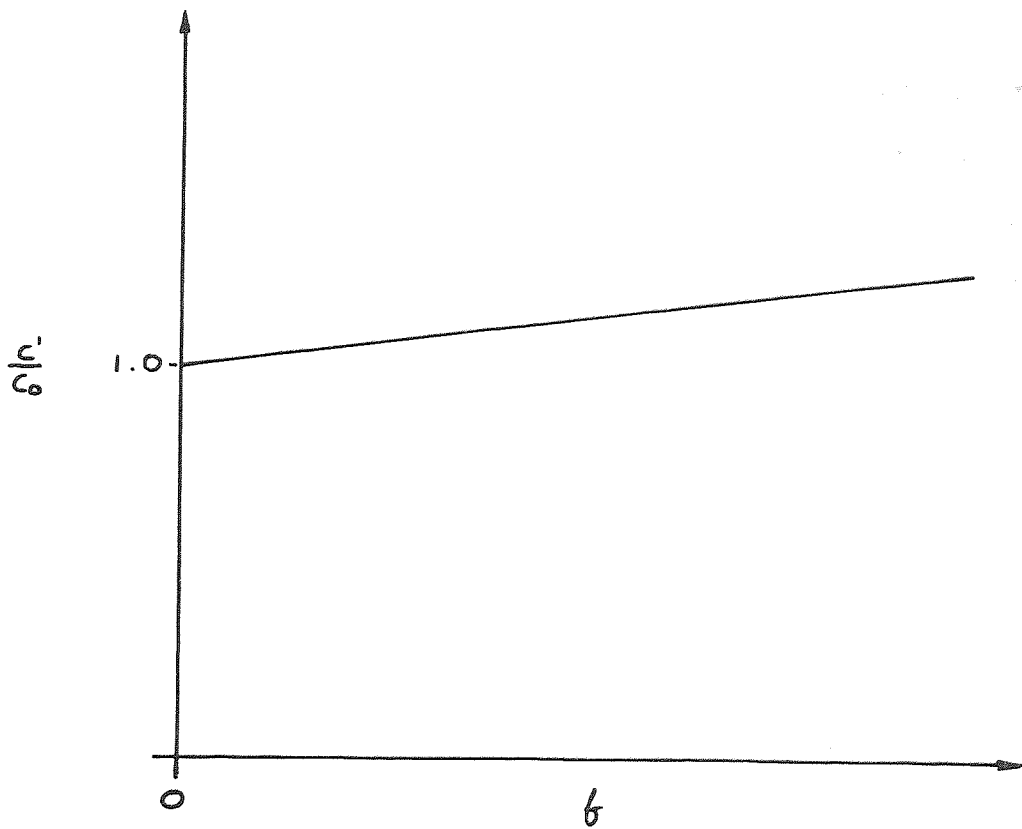


Fig. A.1.3. Graph of c'/c_0 vs f for Transmission Line Model

Appendix 2: Initial Bias System

A.2.1 Description

The initial bias system is shown in Fig. A.2.1. The pulse P11 was derived from a separate multivibrator in the pulse generator, and was altered in the pulse modifier shown to give two complementary pulses operating between 0V and 6V, in opposite senses. These pulses then switched the two sides of the diode pump system on between 0 and 108 μ s.

As can be seen, the reference and bone side signals for the bias system were derived from the respective transformer primaries of the final amplifiers. The 10 pF capacitor and two diodes provided a rectifying and voltage doubling system, which converted the pilot signal into a voltage which was maintained on the 680 pF capacitor.

The charges on each 680 pF capacitor were then compared, and the result fed to the d.c. amplifier shown in the figure. As the leakage of each capacitor had been arranged to cancel, the voltage presented to the high impedance input of the d.c. amplifier would be constant after 108 μ s. The output of this was then fed directly to the A.G.C. amplifier, as no sample and hold mechanism was required.

A.2.2 Initial Bias System Theory

The concept of the initial bias system was to compare received pilot signals from both transducers. This was to be achieved by deriving a d.c. voltage representative of the size of each signal, and subtracting the one from the other. This difference was then to be maintained until the next cycle, when an increment would be added due to any change in the difference. Thus the time constant of the system was arranged to be longer than the repeat time of 2 ms.

Components for Initial Bias System

T1, T2 = BC 477
T3, L1 = Bone side final amplifier output
T4, L2 = Reference side final amplifier output
T5, T7 = BFX 48
T6 = BC 109
F1 = 2N 3821 JFET
F2 = 2N 3819 JFET

The equivalent circuit for the analysis of the operation of the initial bias theory is shown below in Fig. A.2.2.

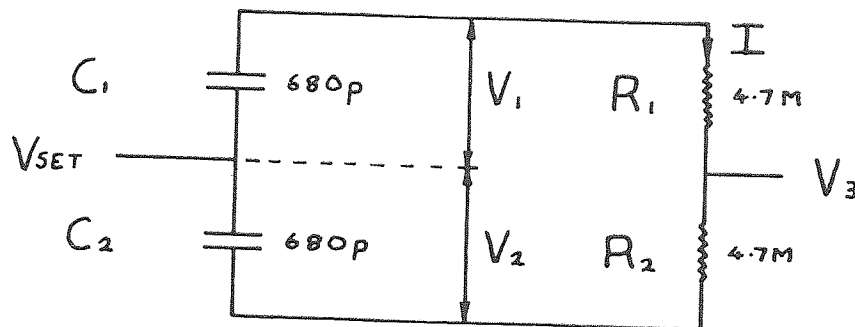


Fig. A.2.2 Equivalent Circuit for Initial Bias System

This circuit assumes that the input impedance of the d.c. amplifier connected to the point V_3 is infinite, and therefore draws no current.

Now,

$$I = \frac{V_1 + V_2}{R_1 + R_2} = \left(\frac{V_{10} + V_{20}}{R_1 + R_2} \right) e^{-\left[\frac{t}{(R_1 + R_2)C^X} \right]}$$

$$\text{where } C^X = \frac{1}{\frac{1}{C_1} + \frac{1}{C_2}} = \frac{C_1}{2} \quad \text{if } C_1 = C_2$$

Now,

$$V_3 = V_{SET} + V_1 - IR_1 \tag{A2.1}$$

$$\text{and } V_3 = V_{SET} - V_2 + IR_2 \tag{A2.2}$$

If $R_1 = R_2$, then, adding (A2.1) and (A2.2)

$$2V_3 = 2V_{SET} + V_1 - V_2$$

$$\text{or } V_3 = V_{SET} + \frac{V_1 - V_2}{2} \tag{A2.3}$$

Now,

$$I = C_1 \frac{dV_1}{dt} = C_2 \frac{dV_2}{dt}$$

$$\text{If } C_1 = C_2, \text{ then } \frac{dV_1}{dt} = \frac{dV_2}{dt}$$

$$\therefore \frac{d}{dt}(V_1 - V_2) = 0$$

Hence from (A2.3)

$$V_3 = V_{\text{SET}} + \frac{V_1 - V_2}{2} = V_{\text{SET}} + \frac{V_{10} - V_{20}}{2} \quad (\text{A2.4})$$

Thus V_3 represents the difference between V_1 and V_2 , and this is maintained even though the charges on each capacitor may leak.

If one considers the time constant of the system, τ , approximately to be given by:

$$\tau = 20 \times 10^6 \times 1400 \times 10^{-12} = 28 \text{ ms}$$

where the input impedance of the d.c. amplifier is about $20 \text{ M}\Omega$, and the two 680 pF capacitors in parallel amount to approximately 1400 pF . This long time constant was considered to be the principle cause of instability in the initial bias system.

Appendix 3: Frequency Response of Transducer Coupling

A.3.1 Coupling Between Driver Amplifier and Transducer

When the transducer is transmitting the signal, the 10 nF capacitor in Figs. 2.7 and 2.8 is effectively in parallel with the L-R circuit. The diode D3 is conducting, but its resistance and the impedance of the transducer will be ignored for the moment. Therefore we have the equivalent circuit shown below in Fig. A.1.

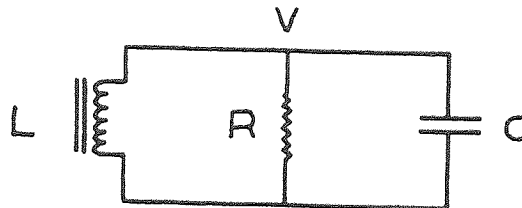


Fig. A.3.1 Equivalent Circuit with Transducer Transmitting

From Fig. A.1

$$\frac{V}{j\omega L} + \frac{V}{R} + j\omega C = 0$$

$$\therefore C \frac{dV}{dt} + \frac{1}{R} V + \int \frac{1}{L} V dt = 0 \quad (\text{A3.1})$$

differentiating equation (A.1), and dividing by C,

$$\frac{d^2V}{dt^2} + \frac{1}{RC} \frac{dV}{dt} + \frac{1}{LC} V = 0$$

Thus, for critical damping,

$$\left(\frac{1}{2RC} \right)^2 = \frac{1}{LC}$$

$$\therefore 2R = \sqrt{\frac{C}{L}} \quad (\text{A3.2})$$

Now, $C = 10\text{nF} = 10^{-8}\text{F}$

$L = 3\mu\text{H} = 3 \times 10^{-6}\text{H}$

$\therefore 2R = \sqrt{30,000}$

$\therefore R = 86\Omega$

Thus it can be shown that the circuit is overdamped, as the value of R is actually 20Ω . However, no account in this analysis can be taken of the effect of the diode D_3 , which will be dissipative, or the effect of the transducer impedance. No one as yet has been able to write a wave equation for a wave in the piezo-electric material, which involves both electrical and mechanical parameters, so an expression for the transducer impedance cannot be cited. It has been found experimentally that this impedance is of a value of a few Ohms. Experiment has also revealed that the system has a good response over a broad range of high frequencies.

In practice, the coupling does not appear to cause any resonant oscillation, so one may assume that it is operating in a nearly critically damped state.

A.3.2 Coupling Between Transducer and Preamplifier

When the transducer is receiving, the equivalent circuit is approximately that shown in Fig. A.2 below.

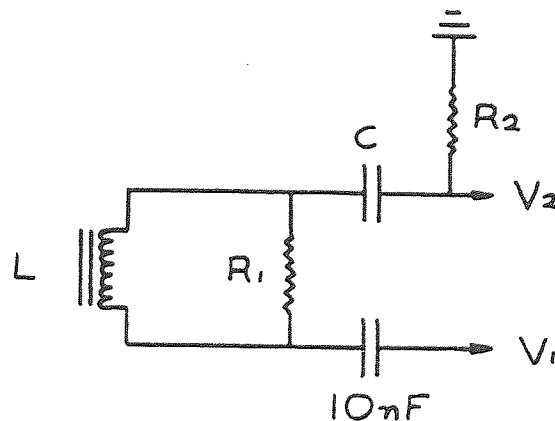


Fig. A.3.2 Equivalent Circuit with Transducer Receiving

The value of the 10nF capacitor can be ignored, as it is effectively in series with C, which is 100pF.

Therefore,

$$V_2 = V_1 \left(\frac{R_2}{R_2 + \frac{1}{j\omega C} + \frac{1}{\frac{1}{j\omega L} + \frac{1}{R_1}}} \right)$$

$$\therefore \frac{V_2}{V_1} = \frac{R_2 + \left(\frac{R_2}{R_1} \right) j\omega L}{R_2 + \left(\frac{R_2}{R_1} \right) j\omega L + j\omega L + \frac{1}{j\omega C} + \frac{L}{R_1 C}} \quad (\text{A3.3})$$

The accuracy of this equation will be affected mainly by L, as the value of the inductance quoted has an error of about $\pm 10\%$. Thus, for an approximate solution, let:

$$R_1 = 20\Omega$$

$$R_2 = 400\Omega$$

$$C = 100\text{pF} = 10^{-10} \text{ F}$$

$$L = 3\mu\text{H} = 3 \times 10^{-6} \text{ H}$$

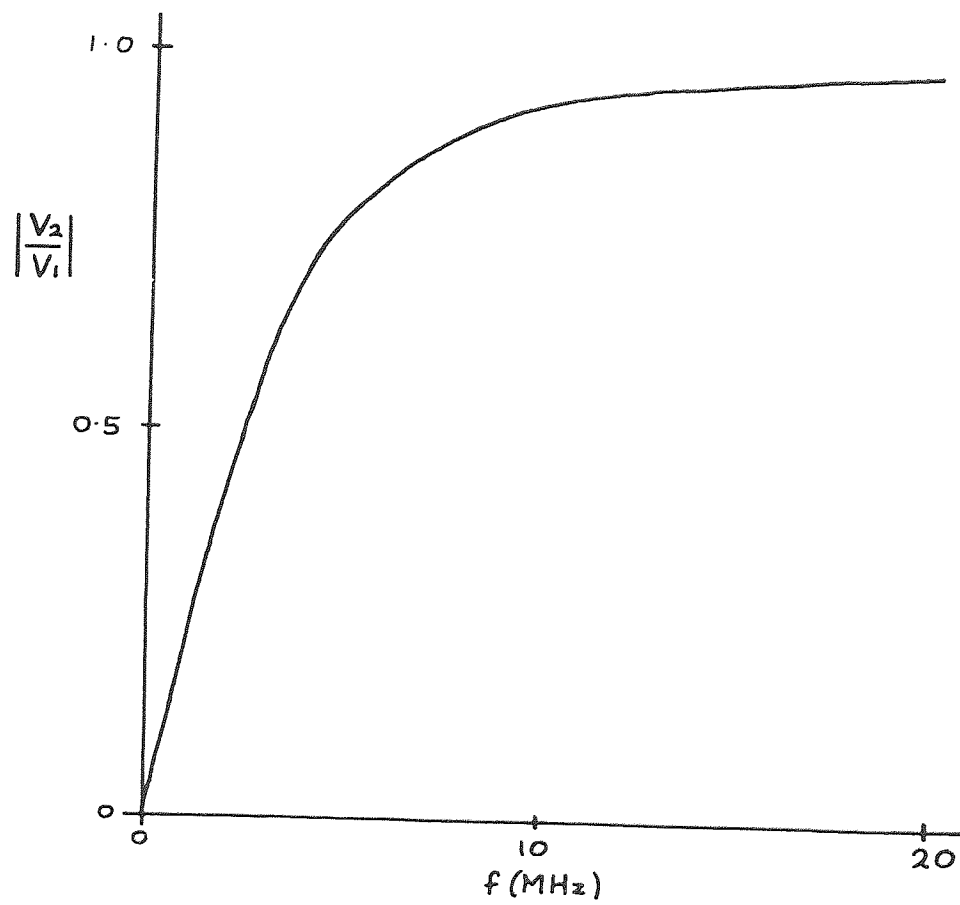
$$\omega = 2\pi f \times 10^6, \text{ where } f \text{ is in MHz.}$$

$$\therefore \frac{V_2}{V_1} \approx \frac{400 + 400 jf^2}{200 + j \left(400 \frac{1600}{f} \right)}$$

$$\therefore \left| \frac{V_2}{V_1} \right| = \left(\frac{1 + f^2}{25 + \left(f - \frac{4}{f} \right)^2} \right)^{\frac{1}{2}} \quad (\text{A3.4})$$

This equation (A3.4) gives the graph shown in Fig. A.3.3.

The circuit previously existing gave a response having a maximum at about 8.5 MHz, and this tended to promote oscillation via a feedback loop including the high gain amplifier. The inclusion of R_2 has made



A.3.3 Frequency Response of Transducer Coupling

a radical change in the behaviour of the system in that its response now exhibits no peak or maximum.

Appendix 4: Investigation of Computing Costs

A.4.1 Estimation of Computing Costs for Zemanek Algorithm

From Zemanek (1971),

$$P(z, x) = \left| \sum_{p=1}^m \sum_{q=1}^n \frac{\Delta S_q}{R_{p,q}} e^{[j(a/\lambda)^2 R_{p,q}]} \right|$$

$$\text{where } n = \frac{4a}{\lambda} = 4k$$

$$m = n\pi^{10} = 4k\pi^{10}$$

$$\Delta\psi = \frac{\pi}{m} = \frac{1}{4k\pi^9}$$

$$\Delta\sigma = \frac{\lambda}{na} = \frac{1}{nk} = \frac{1}{4k^2}$$

$$\sigma_q = \Delta\sigma(q - \frac{1}{2}) = \frac{(q - \frac{1}{2})}{4k^2}$$

$$\therefore \Delta S_q = \sigma_q \Delta\sigma \Delta\psi = \frac{(q - \frac{1}{2})}{4k^2} \cdot \frac{1}{4k^2} \cdot \frac{1}{4k\pi^9}$$

$$\text{and } R_{p,q} = \left[x^2 + z^2 + \sigma_q(\sigma_q - 2x \cos\psi_p) \right]^{\frac{1}{2}}$$

Now,

$$P(z, x) = \left| \sum_{q=1}^n \Delta S_q \sum_{p=1}^m \frac{1}{R_{p,q}} e^{[jk^2 R_{p,q}]} \right|$$

$$= \left| \sum_{q=1}^n \Delta S_q \sum_{p=1}^m \frac{1}{R_{p,q}} \left[\cos(k^2 R_{p,q}) + j\sin(k^2 R_{p,q}) \right] \right|$$

Although Zemanek gives no computer program to evaluate this algorithm, it would probably be implemented as follows:-

```

1 int n = 4*k
2 int m = n*pi* 10;
3 real dsigma = 1/(n*k), dpsi = pi/m;
4 real consta = dsigma*dpsi,constb = x↑2 + z↑2,
   conste = 2*x, constd = k↑2;
5 [1 : m] real costerm;
6 for i to m do costerm[i]:=constc*cos(dpsi*(p-.5))od;
7 compl result:=0;
   for q to n
8 do compl sum:=0;real sigmaq=dsigma*(q-.5);
   for p to m
9 do real rpq=sqrt(constb+sigmaq*(sigmaq-costerm[p]));
10 real angle = constd*rpq;
11 sum plusab cos(angle)i sin(angle)/rpq
   od;
12 result plusab (sigmaq*consta)*sum
   od;
13 print (abs result);

```

Although there may be a more efficient method of evaluating $P(z,x)$ by reorganising the series, this simple program will do to find to an order of magnitude the costs of computing the Zemanek algorithm.

The University's computer is an ICL 1904S, and the following table is a rough estimate of the costs involved in various operations involved in the preceding algorithm:

+	-	5 μ s
-	-	5 μ s
*	-	10 μ s
/	-	20 μ s
2	-	70 μ s
<u>abs</u>	-	20 μ s
<u>sqrt</u>	-	165 μ s
<u>sin</u>	-	215 μ s
<u>cos</u>	-	215 μ s

Therefore, for each line of the program, the costs are:

$$\begin{aligned}
 \underline{6} \quad & 5+10+215+10 & = & 240(\times m)\mu\text{s} \\
 \underline{7} \quad & 10+5 & = & 15(\times n)\mu\text{s}
 \end{aligned}$$

<u>9</u>	165+5+10+5	= 185($\times n \times m$) μ s
<u>10</u>	10	= 10($\times n \times m$) μ s
<u>11</u>	215+215+20+20+5+5	= 480($\times n \times m$) μ s
<u>12</u>	10+10+10+5+5	= 40($\times n$) μ s
<u>13</u>	165+4+70+70+	= 309 μ s

Adding these, and using $m = 4k\pi^{10}$, $n = 4k$, gives:

$$\text{Costs} = [309 + (960\pi^{10} + 220)k + 10,800\pi^{10} k^2] \mu\text{s}.$$

This gives a value of about 2.5×10^{10} for $k = 5$, i.e. $a = 5\lambda$.

A.4.2 Estimation of Computing Costs for New Algorithm using Huygen Green's Function

$$I = \frac{1}{\pi} \int_0^{\pi} e^{-jks} \left(\frac{ab\cos\psi - a^2}{a^2 + b^2 - 2ab\cos\psi} \right) d\psi$$

where $s = (z^2 + a^2 + b^2 - 2ab\cos\psi)^{\frac{1}{2}}$

$$\therefore I = \frac{1}{\pi} (I_1 - jI_2), \text{ where}$$

$$I_1 = \int_0^{\pi} \cos ks \left(\frac{ab\cos\psi - a^2}{a^2 + b^2 - 2ab\cos\psi} \right) d\psi = \int_0^{\pi} f_1(\psi) d\psi$$

$$I_2 = \int_0^{\pi} \sin ks \left(\frac{ab\cos\psi - a^2}{a^2 + b^2 - 2ab\cos\psi} \right) d\psi = \int_0^{\pi} f_2(\psi) d\psi$$

This can be evaluated using the following core program:

```

1 real consta = a 2, constb=b 2, constf = z 2;
2 real constc = consta+constb, constd=a*b;
3 real conste = 2*constd;
4 proc f1 = (real psi)real;
   real costerm = constd*cos(psi);
   real s* = constc - 2*costerm;
   real s = sqrt(s2+constf);
   cos(k*s)*(costerm-consta)/s2;

```

```

5 proc f2 = (real psi)real;
   real costerm = constd*cos(psi);
   real s2 = constc - 2*costerm;
   real s = sqrt(s2+constf);
   sin(k*s)*(costerm-consta)/s2;

```

This is then a first approximation to evaluate the new algorithm and, as with the Zemanek algorithm, is not the most efficient method for the problem. A call to the NAG library to perform the Patterson's quadrature method for the functions f_1 and f_2 would be:

```

6 real I1 := D01ACA(.... f1 .....);
7 real I2 := D01ACA(.... f2 .....);
8 print (sqrt((I1+2+I2+2)/pi));

```

Now, if the Patterson algorithms use n_1, n_2 evaluations of $f_1(\psi)$ and $f_2(\psi)$ respectively (these values will vary depending upon the "difficulty" of evaluating I1 and I2), then the costs will be approximately given by:

$$\begin{aligned} \text{Costs} &= (n_1+n_2)[(215+10+10+5+5+165+215+10+10+10 \\ &\quad +5+20+10+5+20+\text{internal operations})]\mu\text{s} \\ &= (n_1+n_2)(705+x)\mu\text{s} \end{aligned}$$

A generous value for x could be, say, 295,

$$\therefore \text{Costs} = 1000(n_1+n_2)\mu\text{s}$$

The maximum allowed value of n_1 or n_2 is 381, as this is the largest number of points that the quadrature method could possibly take into account. This will give a value of about $7.6 \times 10^5 \mu\text{s}$, and is independent of k .

Thus it can be shown that this new algorithm is approximately 3×10^4 times more efficient than Zemanek's. However, it should be noted that these estimations have been made for the results presented, at $a = 5\lambda$, i.e. $k = 5$, which is slightly biased against the Zemanek algorithm. At $a = \lambda$, i.e. $k = 1$, the factor will be about 1000, as the rise in the factor is roughly proportional to k^2 .

Moreover, it may have been impossible for Zemanek to compute the diffraction pattern of a ring transducer such as that mentioned in Chapter 4, as for $k = 25\lambda$, the factor would be about 6.25×10^5 and this may have been beyond the capabilities of the CDC 6400 computer used by Zemanek.

A.4.3 Estimation of Computing Costs for Lockwood and Willette Algorithm

Lockwood and Willette (1973) have produced a single integral technique to evaluate the same diffraction field as Zemanek, i.e. that corresponding to Huygen boundary conditions. In evaluating the effectiveness of this technique, Lockwood and Willette have shown that, as the computing factor is proportional to k^2 for the Zemanek algorithm, theirs is only proportional to k . Hence this single integral technique involves less computing costs than Zemanek's for values of k greater than unity.

Thus the Lockwood and Willette algorithm can be compared against that presented in Chapter 5. At $k=1$, the present technique is about 1,000 times more efficient, as is so with the Zemanek algorithm. For $a = 5\lambda$, i.e. $k = 5$, the factor will be about 5,000, and for the ring transducer calculations, about 25,000. Thus it may have been possible for Lockwood and Willette to compute the diffraction pattern of a ring transducer obeying the Huygen boundary conditions if they had the same size computer as Zemanek, as this factor is almost the same as Zemanek's for his disc transducer.

Appendix 5: Publication

A single integral computer method for axisymmetric transducers with various boundary conditions

J.A. Archer-Hall and D. Gee

A computer method is presented which can be applied to any Green's function for an axisymmetric system, ie disc and ring transducers. The acoustic field is given by a general integral which, by suitable geometry, can be transformed, without approximation to a single integral with fixed limits, provided that the integral is analytically evaluable at an axis point for the Green's function chosen. The single integral is then capable of evaluation by computer using Patterson's quadrature method. Three types of boundary condition have already been applied to this method. The function corresponding to 'pressure release' boundary conditions is of particular significance in medical ultrasonography, as it corresponds most closely to a transducer applied to the skin. Diffraction fields have been computed for ring and disc transducers using this function, and these show marked differences from the values obtained by using the usual Huygen function.

Introduction

The usual method of analysing diffraction fields involves surface integrals of the form:

$$\phi_D = A \iint_S G dS \quad (1)$$

where A = arbitrary constant, S = surface and G = any Green's function, as shown in Fig. 1.

The Green's function may be defined as one that obeys the d'Alembertian equation:

$$(\nabla^2 + k^2)G = 0$$

where $k = 2\pi/\lambda$ and λ = wavelength.

Fig. 2 shows three examples of Green's functions. These have been called the Huygen, Kirchoff and Radiating Dipole functions. The choice of Green's function to be used in a particular case is dictated by the boundary conditions, and here the conditions to which each applies are illustrated diagrammatically.

The conditions for the use of the Huygen function imply an ideally rigid infinite baffle surrounding the transducer, which imposes the boundary condition that the normal component of fluid particle velocity shall be zero in the $z = 0$ plane, except over the transducer face. A close approximation to these conditions, in practice, would be a sonar device set in the side of a large ship.

The Kirchoff function is appropriate for a transducer in a thin case, totally immersed in the acoustic medium. The rear wall of the case must be insulated from the transducer, and be ideally rigid, thus imposing zero normal component of particle velocity, on its surface.

The radiating dipole function fits the boundary condition for zero acoustic pressure in the $z = 0$ plane outside the transducer, as illustrated in Fig. 3.

This condition is appropriate for an air to liquid or air to solid interface on which a transducer is applied.

The theories of the Kirchoff and Huygen integrals have been fully described by Baker and Copson,¹ and Morse and Ingard.² The third of these functions, the Radiating Dipole, has only recently been used in a suitable form for ultrasonic diffraction studies. Fig. 3 illustrates the boundary conditions for this function, which are such that the acoustic pressure is zero in the $z = 0$ plane, outside the disc. These conditions are much closer to those found in medical ultrasonography than for either of the other two functions.

The Radiating Dipole Green's function is derived by considering an array of acoustic dipoles as a model. This is mathematically identifiable with the case of a freely suspended, un baffled disc in an infinite medium.

Theory

Consider the single dipole shown in Fig. 4. It consists of two point sources, S_1 and S_2 , 180° out of phase, a distance 2δ apart. Each source is represented by the function for a spherical wave:

$$\phi_1 = \frac{e^{-jkx_1}}{s_1} \quad \text{for source } S_1$$

$$\phi_2 = \frac{e^{-jkx_2}}{s_2} \quad \text{for source } S_2$$

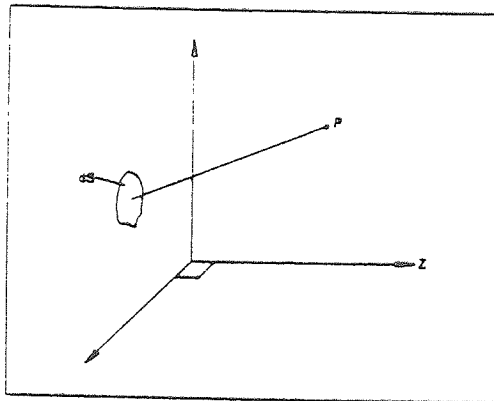


Fig. 1 Geometry of general surface integral

Name	Green's function	Boundary conditions
Huygen's	$\frac{e^{-jks}}{s}$	Idea rigid barrier ($q_n = 0$) Transducer
Kirchoff's	$\frac{e^{-jks}}{s} \left[jk \left(1 + \frac{z}{s} \right) + \frac{z}{s^2} \right]$	Vibrating surface of transducer Rigid surface ($q_n = 0$) No barrier
Radiating dipole	$\frac{e^{-jks}}{s} \left(jk + \frac{1}{s} \right)$	Transducer

Fig. 2 Examples of Green's functions

The radiating Dipole Green's function is a combination of these two sources.

$$G = \phi_1 + \phi_2 = \frac{e^{-jkx_1}}{s_1} - \frac{e^{-jkx_2}}{s_2} \quad (2)$$

as $\delta \rightarrow 0$, the function becomes:

$$G = \frac{\partial}{\partial z} \frac{e^{-jkz}}{s} = \left(-jk - \frac{1}{s} \right) \frac{e^{-jkz}}{s} \frac{\partial s}{\partial z}$$

Since $\frac{\partial s}{\partial z} = -\cos \theta$ as $\delta \rightarrow 0$,

and $\cos \theta = \frac{z}{s}$ from the geometry of Fig. 4;

$$G = \left(jk + \frac{1}{s} \right) \frac{e^{-jkz}}{s} \frac{z}{s} \quad (3)$$

Thus the integral describing the acoustic field for the free surface boundary conditions is:

$$\phi_p = A \iint_S \frac{e^{-jkz}}{s} \frac{z}{s} \left(jk + \frac{1}{s} \right) dS \quad (4)$$

from Equation 1, where A is an arbitrary normalizing constant.

For all three Green's functions illustrated in Fig. 2, it is possible to evaluate the surface integral for a disc analytic-

ally at an axis point. This is necessary for the present technique.

These three double integrals can be turned into single integrals by applying the geometry shown in Fig. 5, which has to be considered separately for two cases. Fig. 5a applies to points whose normals to the $z = 0$ plane fall within the disc, and Fig. 5b where they fall outside. The reason for selecting this geometry is that for areas dS on the circular arcs ΔS shown, the length s and the ratio z/s are constant.

Omitting the arbitrary constant from Equation 4, the integral required is:

$$I = \iint_S \frac{e^{-jkz}}{s} \frac{z}{s} \left(jk + \frac{1}{s} \right) dS$$

$$= \int_{\beta_1}^{\beta_2} \int_{-\alpha}^{+\alpha} \frac{e^{-jkz}}{s} \frac{z}{s} \left(jk + \frac{1}{s} \right) \rho d\rho d\beta \quad (5)$$

The first stage of integration can now be performed with respect to the only remaining variable, β

$$I = \int_{\beta_1}^{\beta_2} \frac{e^{-jkz}}{s} \frac{z}{s} \left(jk + \frac{1}{s} \right) 2\alpha \rho d\rho \quad (6)$$

Now, from the geometry of Fig. 5,

$\rho d\rho = s ds$ as $s^2 = z^2 + \rho^2$ and z is constant

$$I = 2 \int_{s_1}^{s_2} e^{-jkz} \frac{z}{s} \left(jk + \frac{1}{s} \right) \alpha ds \quad (7)$$

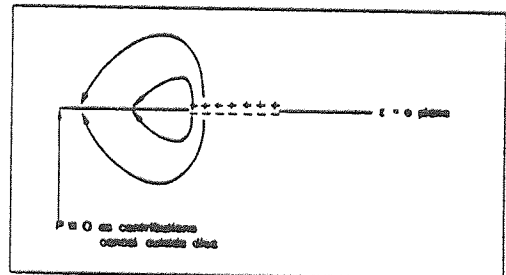


Fig. 3 Boundary conditions of radiating dipole

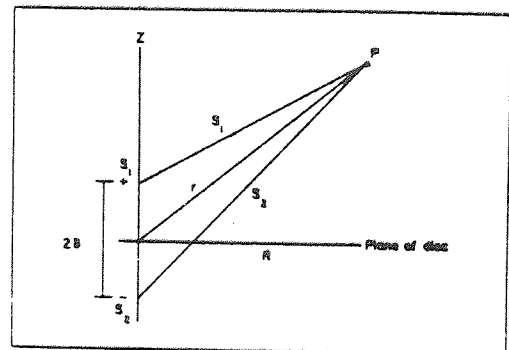


Fig. 4 Single radiating dipole

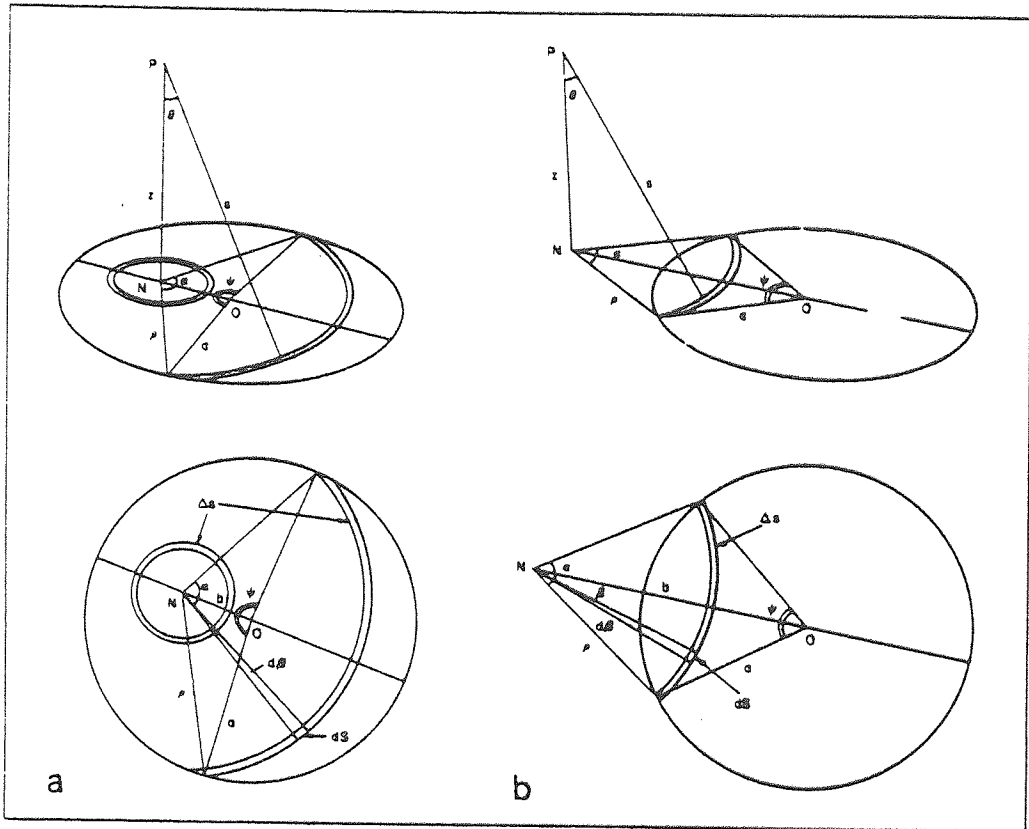


Fig. 5(a) and 5(b) Geometry used for transformations

Let the factor 2 become part of the arbitrary constant A. Equation 7 can now be integrated by parts giving:

$$I = \left[-e^{-kz} \frac{z}{s} \alpha \right]_{z_1}^{z_2} \quad (8a)$$

$$+ \int_{z_1}^{z_2} -e^{-kz} \frac{z}{s} d\alpha \quad (8b)$$

The term in Equation 8a becomes e^{-kz} for points where $b < a$, and zero for $b > a$, i.e. points outside the disc. The enumeration of the remaining integral in Equation 8b by computer is facilitated by substituting for $d\alpha$ in terms of the angle ψ subtended by the ends of the arc elements ΔS at 0, as follows:

$$\cos \alpha = (b^2 - a^2 + \rho^2) / 2b\rho \quad (9)$$

$$\cos \psi = (b^2 + a^2 - \rho^2) / 2ab \quad (10)$$

$$\frac{\sin \alpha}{a} = \frac{\sin \psi}{\rho} \quad (11)$$

By differentiating Equation 9 with respect to ρ and substituting from Equation 11 into the result:

$$\sin \psi \frac{d\alpha}{d\rho} = \frac{b^2 - a^2 - \rho^2}{2ab\rho} \quad (12)$$

Differentiating Equation 10 with respect to ρ and dividing Equation 12 by the result gives:

$$\frac{d\alpha}{d\psi} = \frac{b^2 - a^2 - \rho^2}{2\rho^2}$$

and from Equation 10:

$$d\alpha = \left(\frac{ab \cos \psi - a^2}{a^2 + b^2 - 2ab \cos \psi} \right) d\psi \quad (13)$$

Now $s^2 = z^2 + \rho^2 = z^2 + a^2 + b^2 - 2ab \cos \psi$

$$I = e^{-kz} + \int_0^\pi e^{-kz} \frac{z}{s} \left(\frac{ab \cos \psi - a^2}{a^2 + b^2 - 2ab \cos \psi} \right) d\psi$$

Thus the evaluation of I in the general case involves the computation of a single integral with fixed limits, and the addition of a term such as e^{-kz} for $b < a$, but not for $b > a$, as this term is zero outside the disc.

For the actual process of computation, the two terms, e^{-kz} and the integral of Equation 10, are both split into real and imaginary parts. The integration is performed using Patterson's quadrature method^{3,4} called from a NAG library subroutines. The modulus of the acoustic

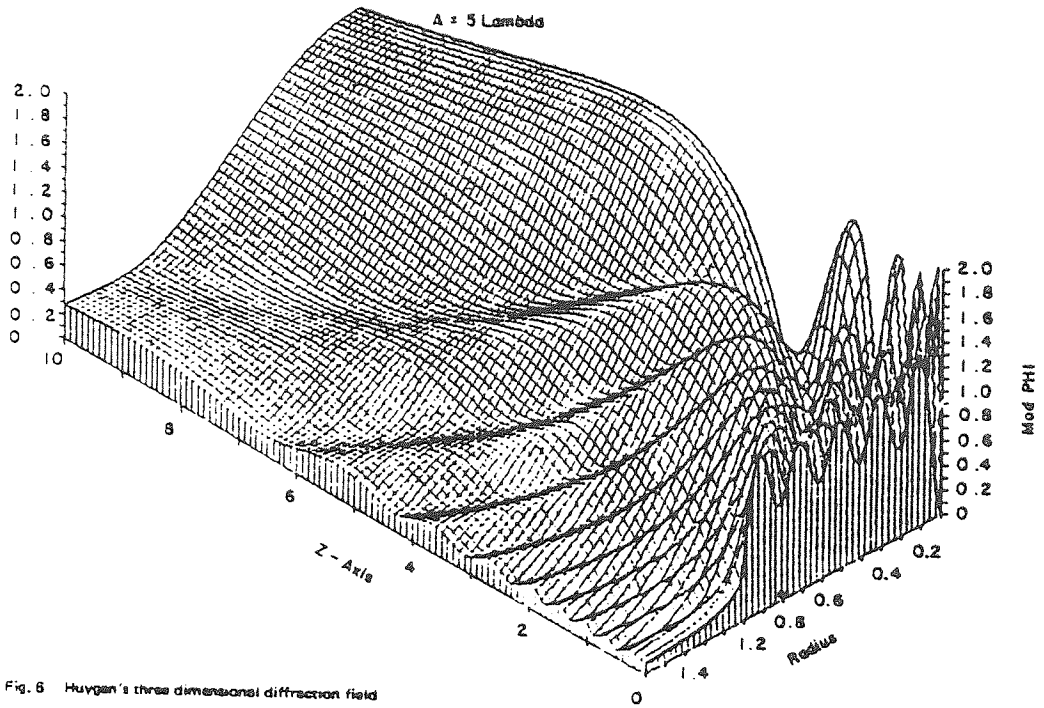


Fig. 6 Huygen's three dimensional diffraction field

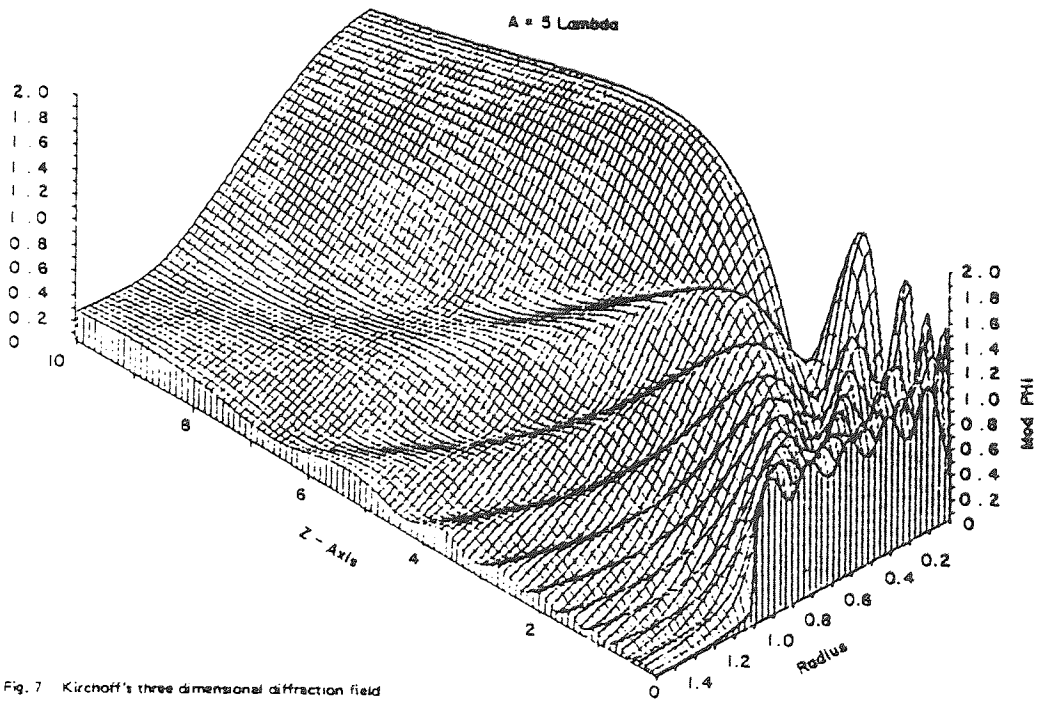


Fig. 7 Kirchoff's three dimensional diffraction field

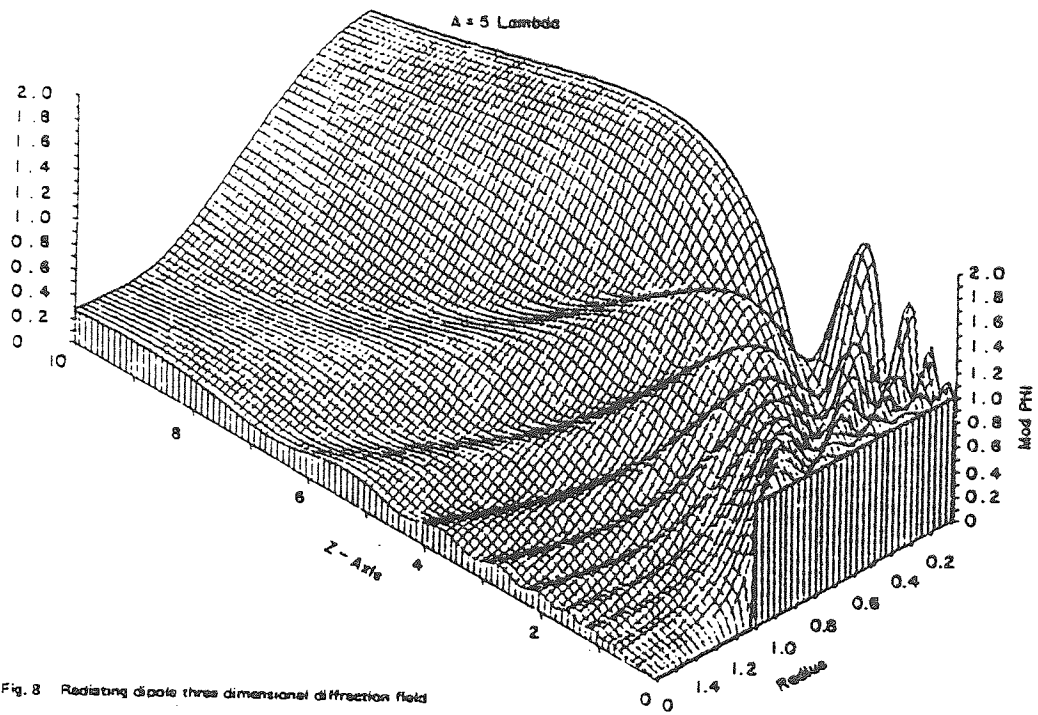


Fig. 8 Radiating dipole three dimensional diffraction field

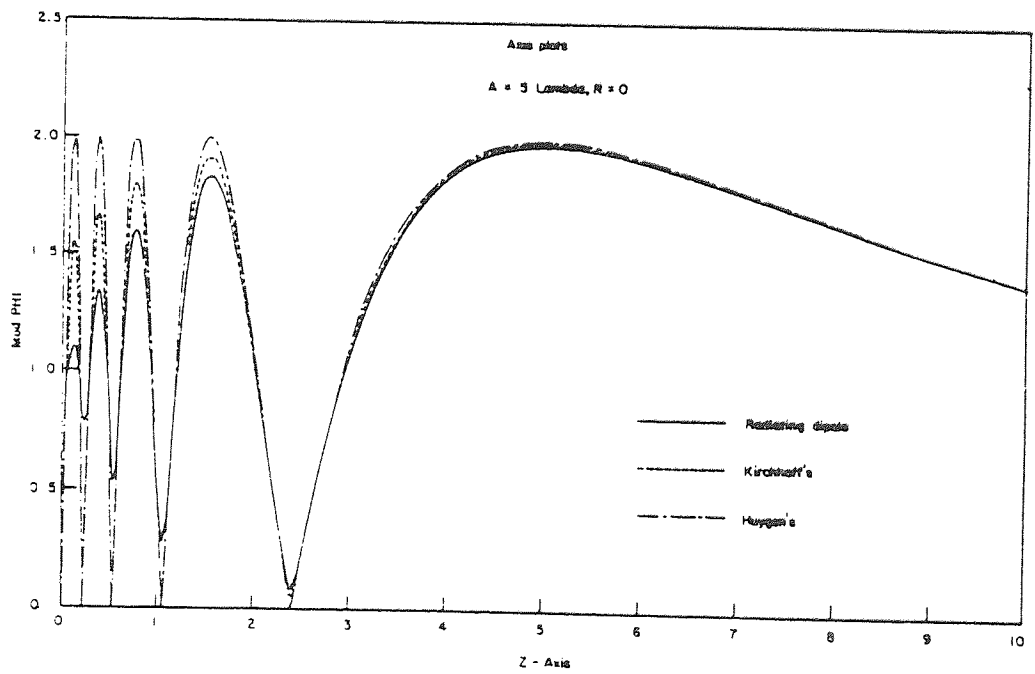


Fig. 9 Axis plots for disc

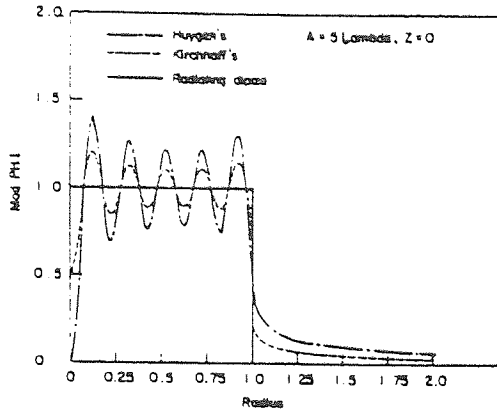


Fig. 10 Cross plots for disc

potential ϕ is then found by taking the square root of the sum of the squares of these real and imaginary results. Values obtained may be plotted graphically to give 'axis plots' ($r = \text{constant}$), 'cross plots' ($z = \text{constant}$), or three dimensional isometric plots by varying r and z .

Results

For comparison against previous work described in other papers^{1,4,7} most of the graphs were plotted with $a = 5\lambda$, where a is the disc radius.

Figs 6,7 and 8 show the three dimensional plots of the Huygen, Kirchoff and Radiating Dipole diffraction fields. Fig. 6 agrees with the three dimensional plot produced by Zemanek⁶ using a far greater amount of computing time in evaluating a complete double integral.

Figs 9 and 10 show the axis plots ($r = 0$), and the cross plots ($z = 0$), of the Radiating Dipole function, compared with those of the Kirchoff and Huygen functions. In the axis plots, the salient features are that the Huygen integral gives a set of zero minima and equal maxima, the Kirchoff varies less, and the Radiating Dipole less still. All three converge to the same result in the Fraunhofer far-field region.

The cross plot illustrates a boundary condition for the Radiating Dipole, that the acoustic potential, and thus the pressure, is zero outside the disc face in the $z = 0$ plane. The Radiating Dipole has a constant pressure across the disc face, and again the Kirchoff varies about this value and the Huygen varies even more. In fact, the Huygen results even predict a zero in the centre of the transducer disc.

This technique has been extended to deal with ring transducers, using the Radiating Dipole function. By subtracting the real and imaginary results for two discs of slightly different radii before the modulus is taken, the system described fits the boundary conditions of a ring transducer.

A ring has been arranged to have a width of 4λ , operating at $a = 25\lambda$. For a real ring of 40 mm diameter, this gives a ring width of 3.2 mm with an ultrasonic frequency in water of about 2 MHz.

Figs 11 and 12 show a series of cross plots and an axis plot, which clearly illustrate a workable 'tube' of focus

from about $5a$ to $15a$, is 10 cm to 30 cm from the disc face. A three dimensional plot of this diffraction field, (Fig. 13), shows the focus 'tube' quite distinctly.

Two other values for the ring width, is 2λ and 8λ , have been investigated, but 4λ appears to be an optimum.

The practical application of such a transducer is open to some discussion, for it seems that a thin ring of a particular width may be able to give as good a resolution as methods involving zone-delay focussing with elaborate electronics used at present in medical ultrasonography. However, further work needs to be carried out to prove or disprove this suggestion.

Conclusion

There are two major advantages to this technique. The first is that the double surface integral can be computed as a single integral. Secondly, the technique can be applied to different boundary conditions. The form of the integrals gives the conclusion that the Kirchoff is the average of the Huygen and Radiating Dipole integrals. This is easily shown after transformation of all three functions into single integrals:

$$\phi_H = e^{-ikz} + \frac{1}{\pi} \int_0^\pi e^{-ikz} \left(\frac{ab \cos \psi - a^2}{a^2 + b^2 - 2ab \cos \psi} \right) d\psi$$

$$\phi_{RD} = e^{-ikz} + \frac{1}{\pi} \int_0^\pi e^{-ikz} \frac{z}{z} \left(\frac{ab \cos \psi - a^2}{a^2 + b^2 - 2ab \cos \psi} \right) d\psi$$

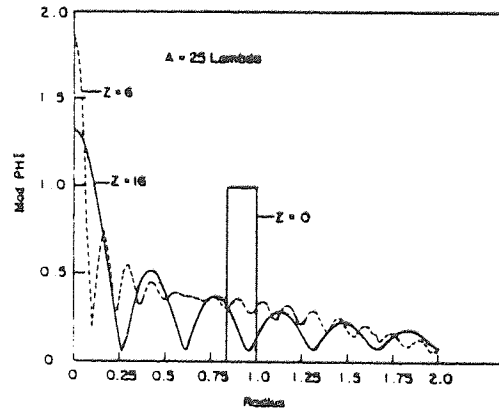


Fig. 11 Ring transducer cross plot

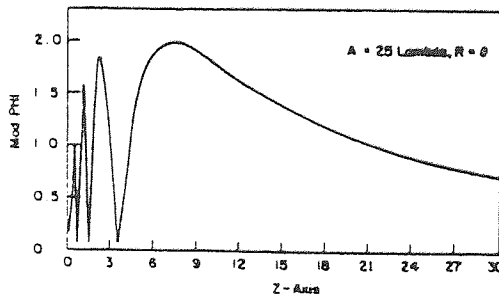


Fig. 12 Ring transducer axis plot

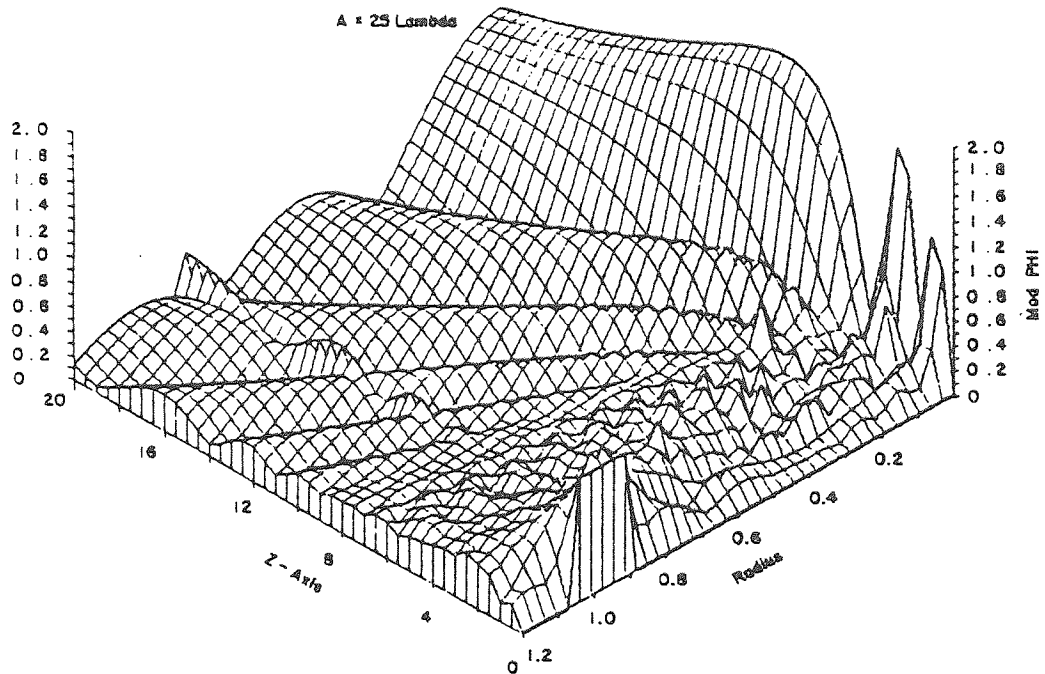


Fig. 13 Ring transducer three dimensional diffraction field

$$\phi_K = e^{-jkz}$$

$$+ \frac{1}{2\pi} \int_0^\pi e^{-jkz} \left(1 + \frac{z}{r}\right) \left(\frac{ab \cos \psi - a^2}{a^2 + b^2 - 2ab \cos \psi}\right) d\psi$$

Therefore $\phi_K = (\phi_H + \phi_{RD})/2$

This result is clearly illustrated in Figs 9 and 10.

It has been conclusively shown from the values obtained by the technique described, that the three Green's functions

comply with the boundary conditions as shown in Fig. 2. Of these, the Radiating Dipole function fits most accurately the conditions which exist in medical diagnostic ultrasonography and for the compressional wave in most cases of non-destructive testing.

Authors

The authors are with the University of Aston in Birmingham, England. Enquiries about the work should be directed to Dr. J.A. Archer-Hall, The University of Aston in Birmingham, Gosta Green, Birmingham B4 7ET, England.

REFERENCES

- Al-Jarallah, M. I., Evaluation and Development of an In Vivo Bone Densitometer, PhD thesis, University of Aston in Birmingham 1976.
- Al-Jarallah, M. I., Archer-Hall, J. A., Francois, P. E., Correlations in Bone Mineral Measurement Using Polychromatic X-rays, Brit. Jour. Radiol., 51, 393-394, 1978.
- Al-Jarallah, M. I., Archer-Hall, J. A., Francois, P. E., Positioning Errors in Bone Mineral Measurement, Brit. Jour. Radiol. 51, 821-822, 1978.
- Allipi, A., Palmieri, L., Nearfield Visualization of a Piston Like Rectangular Source, Acustica, 24, 233-234, 1971.
- Ambrose, J., Computerised Transverse Axial Scanning (Tomography): Part 2, Clinical Application, Brit. Jour. Radiol., 46, 1023-1047, 1973.
- Archer-Hall, J. A., Bashter, A. I. A., The Diffraction Pattern of Large Aperture Bowl Transducers, N.D.T. International, 13, 51-55, 1980.
- Archer-Hall, J. A., Bashter, A. I. A., Hazelwood, A. J., A Means for Computing the Kirchhoff Surface Integral for a Disc Radiator as a Single Integral with Fixed Limits, Jour. Acoust. Soc. Amer., 65, 1568-1570, 1979.
- Archer-Hall, J. A., Carpenter, P. B., Edwards, J. P. N., Francois, P. E., A New Method of Bone Mineral Estimation Using a Conventional X-ray Set, Brit. Jour. Radiol., 46, 375-380, 1973.
- Archer-Hall, J. A., Gee, D., A Single Integral Computer Method for Axisymmetric Transducers with Various Boundary Conditions, N.D.T. International, 13, 95-101, 1980.
- Archer-Hall, J. A., Hutchins, D. A., The Photoelastic Visualisation of Ultrasonic Waves in Liquids, Ultrasonics, 17, 209-212, 1979.
- Archer-Hall, J. A., Hutchins, D. A., A Series Approach for the Determination of Nearfield Radiation Patterns of Axisymmetric Transducers under Various Conditions of Baffle., N.D.T. International, 13, 151-158, 1980.
- Archer-Hall, J. A., Hutchins, D. A., The Effectiveness of Thin Layers as Ultrasonic Visualisation Media, Ultrasonics, 19, 77-80, 1981.
- Baker, B. B., Copson, E. T., The Mathematical Theory of Huygen's Principle, Clarendon Press, 1939.
- Bashter, A. I. A., Ultrasonic Bone Tomography, PhD Thesis, University of Aston in Birmingham, 1976.
- Bow, C. R., McDicken, W. N., Anderson, T., Scorgie, R. E., Muir, A. C., A Rotating Transducer Real-Time Scanner for Ultrasonic Examination of the Heart and Abdomen, Brit. Jour. Radiol., 52, 29-33, 1979.

- Brady, J. K., Goss, S. A., Johnston, R. L., O'Brien, W. D., Dunn, F., Ultrasonic Propagation Properties of Mammalian Testes, Jour. Acoust. Soc. Amer., 60, 1407-1409
- Cameron, J. R., Jurist, J. M., Sorenson, J. A., Mazess, R. B., New Methods of Skeletal Status Evaluation in Space Flight, Aerospace Medicine, 40, 1119-1122, 1969.
- Carson, P. L., Oughton, T. V., Hendee, W. R., Ultrasonic Trans-Axial Tomography by Reconstruction, Ultrasound in Medicine, 2, 341-350, 1976.
- Carstensen, E. I., Schwan, H. P., Acoustic Properties of Haemoglobin Solutions, Jour. Acoust. Soc. Amer., 31, 305-311, 1959.
- Carter, A. H., Williams, A. O., A New Expansion of the Velocity Potential of a Piston Source, Jour. Acoust. Soc. Amer., 23, 179-184, 1951.
- Coulson, C. A., Jeffrey, A., Waves, Oliver and Boyd, 2nd edition, 1977.
- Dehn, J. T., Interference Pattern in the Nearfield of a Circular Piston, Jour. Acoust. Soc. Amer., 32, 1692-1696, 1960.
- Dekker, D. L., Piziali, R. L., Dong, E., Effect of Boundary Conditions on the Ultrasonic-Beam Characteristics of Circular Discs, Jour. Acoust. Soc. Amer., 56, 87-93, 1974.
- Dines, K. A., Kak, A. C., Measurement and Reconstruction of Ultrasonic Parameters for Diagnostic Imaging, Purdue University Report, Tr-EE, 77-84, 1976.
- Donald, I., Brown, T. G., Demonstration of Tissue Interfaces within the Body by Ultrasonic Echo Sounding, Brit. Jour. Radiol., 34, 539-546, 1961.
- Edwards, J. P. N., An In Vivo Bone Densitometer for Use with a Diagnostic X-Ray Set, PhD thesis, University of Aston in Birmingham, 1973.
- Elssasser, U., Reeve, J., Bone Density Measurement with Computed Tomography, Brit. Med. Bull., 36, 243-248, 1980.
- Emiscan CT 1010 Specifications.
- Emiscan 7020 Specifications.
- Emiscan 7020 HR Specifications.
- Emiscan 7070 Specifications.
- Fourman, P., Calcium Metabolism and the Bone, Blackwell Scientific Press, 1960.
- Frederick, J. R., Ultrasonic Engineering, Wiley, 1965.
- Freedman, A., Sound Field of a Rectangular Piston, Jour. Acoust. Soc. Amer., 32, 197-209, 1960.
- Freedman, A., A Mechanism of Acoustic Echo Formation, Acustica, 12, 10-21, 1962.

- Freedman, A., The High Frequency Echo Structure of some Simple Body Shapes, *Acustica*, 12, 61-69, 1962.
- Freedman, A., Transient Fields of Acoustic Radiators, *Jour. Acoust. Soc. Amer.*, 48, 135-138, 1970.
- Freedman, A., Sound Field of Plane or Gently Curved Pulsed Radiators, *Jour. Acoust. Soc. Amer.*, 48, 221-227, 1970.
- Freedman, A., Farfield of Pulsed Rectangular Acoustic Radiator, *Jour. Acoust. Soc. Amer.*, 49, 738-748, 1971.
- Freedman, A., Sound Field of a Pulsed Planar Straight-Edged Radiator, *Acoust. Soc. Amer.*, 51, 1624-1639, 1972.
- Freedman, A., Reply to "Comments on Farfield of a Pulsed Rectangular Radiator", *Jour. Acoust. Soc. Amer.*, 52, 437-438, 1972.
- Freedman, A., The Use of Linear System Theory in Acoustic Radiation and Scattering, *Jour. Sound. Vib.*, 52, 265-276, 1977.
- Fry, F. J., Biological Effects of Ultrasound - A Review. *Proc. I.E.E.E.*, 67, 604-619, 1979.
- Fry, W. J., Leichner, G. H., Okuyama, D., Fry, F. J., Fry, E. K., Ultrasonic Visualisation System Employing New Scanning and Presentation Methods, *Jour. Acoust. Soc. Amer.*, 44, 1324-1338, 1968.
- Glover, G. H., Sharp, J. L., Reconstruction of Ultrasound Propagation Speed Distribution in Soft Tissue: Time-of-flight Tomography, *I.E.E.E. Trans. Son. Ultrason.*, SU-24, 229-234, 1977.
- Gore, J. C., Leeman, S., Ultrasonic Backscattering from Human Tissue: A Realistic Model, *Phys. Med. Biol.*, 22, 317-326, 1977.
- Gore, J. C., Leeman, S., Echo Structure in Medical Ultrasonic Pulse-Echo Scanning, *Phys. Med. Biol.*, 22, 431-443.
- Goss, S. A., Frizzell, L. A., Dunn, F., Frequency Dependence of Ultrasonic Absorption in Mammalian Testis, *Jour. Acoust. Soc. Amer.*, 63, 1226-1229, 1978.
- Goss, S. A., Johnston, R. L., Dunn, F., Comprehensive Compilation of Empirical Ultrasonic Properties of Mammalian Tissues, *Jour. Acoust. Soc. Amer.*, 64, 423-457, 1978.
- Grant, I. S., Philips, W. R., *Electromagnetism*, Wiley, 1975.
- Gray, H., *Anatomy, Descriptive and Surgical*, Bounty Books, 15th edition, 1977.
- Greenleaf, J. F., Johnson, S. A., Lee, S. L., Herman, G. T., Wood, E. H., Algebraic Reconstruction of Spatial Distributions of Acoustic Absorption within Tissue from the Two-Dimensional Acoustic Projections, *Acoustical Holography*, 5, 591-603, 1974.

Greenleaf, J. F., Johnson, S. A., Samoya, W. F., Duck, F. A., Algebraic Reconstructions of Spatial Distributions of Acoustic Velocities in Tissue from their Time-of-Flight Profiles, *Acoustical Holography*, 6, 71-90, 1975.

Greenspan, M., Piston Radiator: Some Extensions of the Theory, *Jour. Acoust. Soc. Amer.*, 65, 608-621, 1979.

Hall, A. J., New Developments in Ultrasonic Equipment, *Brit. Med. Bull.*, 36, 267-272, 1980.

Helela, T., Telkka, A., Virtama, P., Bone Pattern of the Femoral Neck as a Measure of Bone Density and Susceptibility to Hip Fractures, *Ann. Clin. Res.*, 1, 85-87, 1961.

Helela, T., Virtama, P., Bradykinin in Renal Angiography of Normotensive and Hypertensive Patients, *Invest. Radiol.*, 5, 149-152, 1970.

Hounsfield, G. N., Computerised Transverse Axial Scanning (Tomography): Part 1 Description of System, *Brit. Jour. Radiol.*, 46, 1016-1022, 1973.

Howry, D. H., Techniques Used in Ultrasonic Visualisation of Soft Tissues, *Amer. Inst. Biol. Sci.*, 3, 49-65, 1957.

Howry, D. H., Posakony, G., Cushman, C. R., Holmes, J. H., Three Dimensional and Stereoscopic Observation of Body Structures by Ultrasound, *Jour. Appl. Physiol.*, 9, 304-306, 1956.

Hutchins, D. A., The Optical Display of Ultrasonic Waves in Liquids, PhD thesis, University of Aston in Birmingham, 1978.

Johns, H. E., The Physics of Radiology, Charles Thomas, 2nd edition, 1961.

Jurist, J. M., In Vivo Determination of Elastic Response of Bone: 1. Method of Ulnar Resonant Frequency Determination, *Phys. Med. Biol.*, 15, 417-426, 1970.

Kikuchi, Y., Ultrasonic Transducer, Corona Ltd., 1969.

King, L. V., On the Acoustic Radiation of the Piezo-electric Oscillator and the Effect of Viscosity on Transmission, *Can. Jour. Res. Phys. Sci.*, 11, 135-155, 1934.

Kossoff, G., Design of Narrow-Beamwidth Transducers, *Jour. Acoust. Soc. Amer.*, 35, 905-912, 1963.

Kossoff, G., The Effects of Backing and Matching on the Performance of Piezoelectric Ceramic Transducers, *I.E.E.E. Trans. Son. Ultrason.*, SU-13, 20-30, 1966.

Kossoff, G., A Transducer with Uniform Intensity Distribution, *Ultrasonics*, 9, 196-200, 1971.

Kossoff, G., Robinson, D. E., Garrett, W. J., Ultrasonic Two-Dimensional Visualisation Techniques, *I.E.E.E. Trans. Son. Ultrason.*, SU-12, 31-37, 1965.

- Kossoff, G., Robinson, D. E., Garrett, W. J., Two Dimensional Ultrasonography in Obstetrics, Proc. 1st Int. Conf. Diagnostic Ultrasonics, 333-347, 1966.
- Kossoff, G., Robinson, D. E., Garrett, W. J., Ultrasonic Two Dimensional Visualisation for Medical Diagnosis, Jour. Acoust. Soc. Amer., 44, 1310-1318, 1968.
- Kossoff, G., Robinson, D. E., Liu, C. W., Design Criteria for Ultrasonic Visualisation Systems, Ultrasonics, 2, 29-38, 1964.
- Leeman, S., Ultrasound Pulse Propagation in Dispersive Media, Phys. Med. Biol., 25, 481-488, 1980.
- Lobdell, D. D., An Analysis of the Piezoelectric Element for Ultrasonic Pulse Generation and Detection, Proc. 5th U.S. National Congress of Applied Mechanics, 79-87, 1966.
- Lockwood, J. C., Willette, J. G., High-Speed Method for Computing the Exact Solution for the Pressure Variations in the Nearfield of a Baffled Piston, Jour. Acoust. Soc. Amer., 53, 735-741, 1973.
- Lockwood, J. C., Willette, J. G., 1. Finite-Amplitude Sound Propagation in the Farfield of Non-Uniform Sources; 2. The Diffraction of N Waves by a Circular Aperture in a Plane Baffle, Jour. Acoust. Soc. Amer., 54, 1761-1762, 1973.
- Lord Rayleigh, Theory of Sound, MacMillan and Company, 1926.
- Macovski, A., Ultrasonic Imaging Using Arrays, Proc. I.E.E.E., 67, 484-495, 1979.
- Maginess, M. G., Methods and Terminology for Diagnostic Ultrasound Imaging Systems, Proc. I.E.E.E., 67, 641-653, 1979.
- McLachlan, N. W., On the Acoustic and Inertia Pressure on a Vibrating Circular Disc, Phil. Mag., 14, 1012-1025, 1932.
- Millman, J., Halkias, C. C., Integrated Electronics, McGraw-Hill, 1972.
- Morse, P. M., Feshbach, H., Methods of Theoretical Acoustics, McGraw-Hill, 1953.
- Morse, P. M., Ingard, K. U., Theoretical Acoustics, McGraw-Hill, 1968.
- Mueller, R. K., Kaveh, M., Wade, G., Reconstructive Tomography and Application to Ultrasonics, Proc. I.E.E.E., 67, 567-587, 1979.
- Newman, D. R., Ultrasonic Schlieren System Using a Pulsed Gas Laser, I.E.E.E. Trans. Son. Ultrason., SU-20, 282-285, 1973.
- Nordin, B. E. C., Osteoporosis, Advan. Metab. Disorders, 1, 125-151, 1964.

- Oberhettinger, F., On Transient Solutions of the Baffled Piston Problem, Jour. Res. Natl. Bur. Stand. (U.S.), 65 (B), 1-6, 1961.
- Patterson, T. N. L., The Optimum Addition of Points to Quadrature Formulae, Math. Comp., 22, 847-856, 1968.
- Patterson, T. N. L., On Some Gauss and Lobatto Based Quadrature Formulae, Math. Comp., 22, 877-881, 1968.
- Patterson, T. N. L., Algorithm for Automatic Integration Over a Finite Interval, Comm. Assoc. Comp. Machinery, 16, 694-699, 1973.
- Penttinen, A., Luukkala, M., The Impulse Response and Pressure Nearfield of a Curved Ultrasonic Radiator, Jour. Phys. D: Appl. Phys., 9, 1547-1577, 1976.
- Perry, B. J., Bridges, C., Computerised Transverse Axial Scanning (Tomography): Part 3 Radiation Dose Considerations, Brit. Jour. Radiol., 46, 1048-1051, 1973.
- Rayleigh - see Lord Rayleigh.
- Rich, C., Klink, E., Smith, R., Graham, B., Ivanovich, P., Sonic Measurements in Bone Mass, Progress in Development in Methods of Bone Densitometry, N.A.S.A. Report SP-64, 137-146, 1965.
- Robinson, D. E., Kossoff, G., Garrett, W. J., Artefacts in Ultrasonic Echoscopic Visualisation, Ultrasonics, 4, 186-194, 1966.
- Robinson, D. E., Lees, S., Bess, L., Nearfield Transient Radiation Patterns for Circular Pistons, I.E.E.E. Trans. Acoust. Speech Sig. Proc., ASSP-22, 395-403, 1974.
- Rusch, O., Virtama, P., Clavicular Cortical Thickness as Risk Index of Vertebral Compression Factors, Radiology, 105, 551-553, 1972.
- Schoch, A., Betrachtungen über das Schallfeld einer Kolbenmembran, Akust.z., 6, 318-326, 1941.
- Seki, H., Granato, A., Truell, R., Diffraction Effects in the Ultrasonic Field of a Piston Source and their Importance in the Accurate Measurement of Attenuation, Jour. Acoust. Soc. Amer., 28, 230-238, 1956.
- Shaw, E. A. G., On the Resonant Vibrations of Thick Barium Titanate Discs, Jour. Acoust. Soc. Amer., 28, 38-50, 1956.
- Shaw, E. A. G., Sijur, R. J., Vibration Patterns of Loaded Barium Titanate and Quartz Discs, Jour. Acoust. Soc. Amer., 32, 1463-1467, 1960.
- Spence, R. D., A Note on the Kirchhoff Approximation in Diffraction Theory, 21, 98-100, 1949.
- Stenzel, H., Leitfaden zur Berechnung von Schallvorgängen, Springer, 1939.

- Stenzel, H., Die Akustische Strahlung der Reckteckigen Kolbenmembran, *Acustica*, 2, 263-281, 1952.
- Stepanishen, P. R., An Approach to Computing Time Dependent Interaction Forces and Mutual Radiation Impedances between Pistons in a Rigid Planar Baffle, *Jour. Acoust. Soc. Amer.*, 49, 283-292, 1971.
- Stepanishen, P. R., The Time Dependent Force and Radiation Impedance on a Piston in a Rigid Infinite Planar Baffle, *Jour. Acoust. Soc. Amer.*, 49, 841-849, 1971.
- Stepanishen, P. R., Transient Radiations from Pistons in an Infinite Planar Baffle, *Jour. Acoust. Soc. Amer.*, 49, 1629-1638, 1971.
- Stepanishen, P. R., Comments on "Farfield of Pulsed Rectangular Acoustic Radiator", *Jour. Acoust. Soc. Amer.*, 52, 437-438, 1972.
- Stepanishen, P. R., Impulse Response and Radiation Impedance of an Annular Piston, *Jour. Acoust. Soc. Amer.*, 56, 305-312, 1974.
- Stepanishen, P. R., Acoustic Transients in the Farfield of a Baffled Circular Piston Using the Impulse Response Approach, *Jour. Sound Vib.*, 32, 295-310, 1974.
- Stepanishen, P. R., Asymptotic Behaviour of the Acoustic Nearfield of a Circular Piston, *Jour. Acoust. Soc. Amer.*, 59, 749-754, 1976.
- Stepanishen, P. R., Radiated Power and Radiation Loading of Cylindrical Surfaces with Non-uniform Velocity, *Jour. Acoust. Soc. Amer.*, 63, 328-338, 1978.
- Virtama, P., Telkka, A., Helela, T., Relative Density of the Vertebral End-Plates as an Estimate of Osteoporosis, *Brit. Jour. Radiol.*, 38, 360-364, 1965.
- Watson, G. N., A Treatise on the Theory of Bessel Functions, Cambridge University Press, 1966.
- Weight, J. P., Hayman, A. J., Observations of the Propagation of Very Short Ultrasonic Pulses and their Reflection by Small Targets, *Jour. Acoust. Soc. Amer.*, 63, 396-404, 1978.
- Wells, P. N. T., Physical Principles of Ultrasonic Diagnosis, Academic Press, 1969.
- Wells, P. N. T., A Range-Gated Ultrasonic Doppler System, *Med. Biol. Engng.*, 7, 641-652, 1969.
- Wells, P. N. T., Ultrasonics in Clinical Diagnosis, Churchill Livingstone, 1972.
- Wells, P. N. T., Tumour Detection of Ultrasonic Doppler Blood-Flow Signals, *Ultrasonics*, 15, 231-232, 1977.

Wells, P. N. T., Ultrasonics in Medicine and Biology, Phys. Med. Biol., 22, 629-669, 1977.

Wells, P. N. T., Biomedical Ultrasonics, Academic Press, 1977.

Wells, P. N. T., Ultrasonics in Medical Physics, Philos. Trans. R. Soc. London Ser. A, 292 (1390), 187-200, 1979.

Wells, P. N. T., Abdominal Ultrasound Diagnosis, Brit. Med. Bull, 36, 256-260, 1980.

Wells, P. N. T., Bullen, M. A., Follett, D. M., Freundlich, H. F., James, J. A., The Dosimetry of Small Ultrasonic Beams, Ultrasonics, 1, 106-110, 1963.

Wells, P. N. T., McCarthy, C. F., Ross, F. G. M., Read, A. E. A., Comparison of A-Scan and Compound B-Scan Ultrasonography in the Diagnosis of Liver Disease, Brit. Jour. Radiol., 42, 818-823, 1969.

Westwater, F. L., Waddell, W. A., An Introduction to Servomechanisms, English Universities Press, 1961.

Weyns, A., Radiation Field Calculations of Pulsed Ultrasonic Transducers: Part 1 - Planar Circular, Square and Annular Transducers, Ultrasonics, 18, 183-188, 1980.

Weyns, A., Radiation Field Calculations of Pulsed Ultrasonic Transducers: Part 2 - Spherical Disc- and Ring-Shaped Transducers, Ultrasonics, 18, 219-223, 1980.

Wild, J. J., French, L. A., Neal, D., The Experimental Application of Ultrasonics to the Localisation of Brain Tumours, Jour. Neurosurg., 8, 198-203, 1951.

Williams, A. O., Acoustic Field of a Circular Piston, Jour. Acoust. Soc. Amer., 36, 2408-2410, 1964.

Woodcock, J. P., Doppler Ultrasound in Clinical Diagnosis, Brit. Med. Bull., 36, 243-248, 1980.

Zemanek, J., Beam Behaviour Within the Nearfield of a Vibrating Piston, Jour. Acoust. Soc. Amer., 49, 181-191, 1971.